Novel Synthesis of Metal Oxide Nanoparticles via the Aminolytic Method and the Investigation of Their Magnetic Properties

A Thesis
Presented to
The Academic Faculty

by

Daniel E. Sabo

In Partial Fulfillment
of the Requirements for the
Doctor of Philosophy in the
School of Chemistry and Biochemistry

Georgia Institute of Technology
December 2012

Novel Synthesis of Metal Oxide Nanoparticles via the Aminolytic Method and the Investigation of Their Magnetic Properties

Approved by:

Dr. Z. John Zhang, Advisor
School of Chemistry and Biochemistry
Georgia Institute of Technology

Dr. Jiří Janata
School of Chemistry and Biochemistry
Georgia Institute of Technology

Dr. Mostafa El-Sayed
School of Chemistry and Biochemistry
Georgia Institute of Technology

Dr. Dong Qin
College of Materials Science and Engineering
Georgia Institute of Technology

Dr. Angus Wilkinson
School of Chemistry and Biochemistry
Georgia Institute of Technology

Date Approved: November 1, 2012

ACKNOWLEDGEMENTS

I would like to convey my gratitude to all those who supported and helped me throughout my graduate program here at Georgia Tech. The first person I would like to thank is Dr. John Zhang, who was always there for me whenever I had a question or concern about a project I was working on. I would go to his office all worried and, within just a few minutes, he had me calm and laughing again. I am not sure I would have made it through the program without his helpful suggestions and great stories. I would also like to thank my committee members; Dr. Mostafa El-Sayed, Dr. Art Janata, Dr. Angus Wilkinson, and Dr. Dong Qin, for their feedback and suggestions which have no doubt improved the quality of this thesis. I would also like to take this opportunity to express my gratitude towards Dr. Ding and Dr. Ye Cai for their help in performing TEM on my zirconia and manganese oxide samples, respectively, and Dr. Wen Zhang for helping me to acquire ICP-MS data for my yttrium iron garnet and yttrium iron perovskite samples.

Next, I would like to thank past and present group members for their help and suggestions. The first group member I would like to express my gratitude for is Dr. Man Han, who showed me the ropes around the lab and answered every question I posed to him. I would also like to thank Dr. Lisa Vaughan for our conversations which led to some interesting projects, as well as helping me to keep my cool while teaching undergraduate labs. Also I would like to thank Gabriel Hernandez for his humor and his helpful suggestions while reviewing my thesis.

Finally, I would like to thank my family and friends for their support and patience. The first person I am grateful to is my wife, Mary, for her unwavering support and patience throughout my entire graduate program. While Dr. Zhang was able to help

calm me at work, it was Mary who had my back at home. Second, I would like to thank my parents, who always believed in me from the moment in grade school when I came home and told them I wanted to become a “mad scientist”. I would also like to express my gratitude for my in-laws, the Bonn family, for eagerly admitting me as an honorary member of the “Dr. Bonn Club”. Finally, I would like to thank my best friends, Marcelo Molina and Terry Kennedy, who have always been there for me whenever I needed to vent or just relax.

Thank you, everyone! I truly appreciate all of your support in helping me become Dr. Daniel Sabo!

TABLE OF CONTENTS

LIST OF TABLES

LIST OF FIGURES

SUMMARY

Metal oxide nanoparticles, both magnetic and nonmagnetic, have a multitude of applications in gas sensors, catalysts and catalyst supports, airborne trapping agents, biomedicines and drug delivery systems, fuel cells, laser diodes, and magnetic microwaves. Over the past decade, an inexpensive, simple, recyclable, and environmentally friendly large, scale synthesis method for the synthesis of these metal oxide nanoparticles has been sought. Many of the current techniques in use today, while good on the small, laboratory bench scale, suffer from drawbacks that make them unsuitable for the industrial scale. The aminolytic method, developed by Dr. Man Han while working for Dr. Zhang, fits industrial scale-up requirements. The aminolytic method involves a reaction between metal carboxylate(s) and oleylamine in a non-coordinating solvent. This system was shown to produce a range of spinel ferrites. Dr. Lisa Vaughan showed that this method can be recycled multiple times without degrading the quality of the produced nanoparticles. The purpose of this thesis is to test the versatility of the aminolytic method in the production of a wide range of metal oxides as well as various core/shell systems. **Chapter 2** explores the effect of precursor carboxylates chain length on the aminolytic synthesis of cobalt ferrite, and manganese ferrite nanoparticles. In **Chapter 3**, a series of $Cu_xMn_{1-x}Fe_2O_4$, (*x* ranges from 0.0 to 0.2), nanoparticles were synthesized via the aminolytic method. This series allows for the investigation of the effects of orbital Jahn-Teller distortion as well as orbital angular momentum on the magnetic properties of this ferrite. The quantum couplings of magnetic ions in spinel ferrites govern their magnetic properties and responses. An understanding

of the couplings between these metal ions allows for tailoring magnetic properties to obtain the desired response needed for various applications. **Chapter 4** investigates the synthesis of MnO and Mn_3O_4 nanoparticles in pure single phase with high monodispersity. To the best of our knowledge, the range of sizes produced for MnO and Mn_3O_4 is the most extensive, and therefore a magnetic study of these systems shows some intriguing size dependent properties. The final part of this chapter investigates the applicability of the aminolytic method for building a MnO shell on a $CoFe_2O_4$ core. **Chapter 5** explores the synthesis of another metal oxide, ZrO_2 in both the cubic and monoclinic phases with no impurities. The use of the aminolytic method here removes the need for dangerous/expensive precursors or equipment and eliminates the need for extensive high temperature heat treatments that destroy monodispersity which is required for most techniques. The creation of a core/shell system between $CoFe_2O_4$ and ZrO_2 using the aminolytic method was also tested. This core/shell system adds magnetic manipulation which is especially useful for the recovery of zirconia based photocatalyst. **Chapter 6** studies the application of the aminolytic method in the synthesis of yttrium iron garnet (YIG) and yttrium iron perovskite (YIP) nanoparticles. Current synthesis techniques used to produce YIG and YIP nanoparticles often requires high temperatures, sensitive to contamination, which could be eliminated through the use of our method.

CHAPTER 1

INTRODUCTION

1.1 Background of Magnetism

1.1.1 Fundamental Theory of Magnetism

1.1.1.1 Origins of Magnetism[1-5]

Magnetism arises from two electron motions, the spin of an electron, up or down, and the motion of the electron around the nucleus, known as orbital angular momentum. With this in mind, any atom with at least one electron should show magnetism, however it is observed only in materials containing unpaired electrons. This is due to the Pauli's Exclusion Principle, which states that only two electrons of opposite spins can occupy the same orbital resulting in the cancellation of each of their magnetic moments' contribution. Good examples of these types of atoms are the 3-d transition metal ions, such as Mn^{2+}, Cu^{2+}, and Fe^{3+}, which contain unpaired electrons. In these ions, the main contributor of the magnetic moment is the unpaired electron spins. Rare earth metals, such as Gd^{3+}, Pr^{3+}, and Nd^{3+}, show magnetic behavior due to the unpaired electron spin as well as orbital angular momentum, which is larger for these ions than in the 3-d transition metals and therefore cannot be ignored. Metal oxides, alloys, and other compounds that contain these types of ions will exhibit magnetic properties.

The magnetic induction (B) of a material when placed in an applied magnetic field (H) can be described by

$$\mathbf{B} = \mathbf{H}+4\pi M \qquad (1.1.1.1.1)$$

M represents the magnetic moment of a sample per volume. The susceptibility (κ) of a substance is

$$\kappa = M/\mathbf{H} \qquad (1.1.1.1.2)$$

The ratio of magnetic induction to an applied magnetic field is a material's permeability (P) and can be described as

$$P = 1+4\pi\chi \qquad (1.1.1.1.3)$$

where χ_{mol} is a material's molar susceptibility and can be represented with

$$\chi_{mol} = \kappa F/d \qquad (1.1.1.1.4)$$

F is the formula weight of the material and *d* is its density. A magnetic material can be easily classified using its magnetic susceptibility. Each class has a unique magnetic moment alignment and ordering. These different classes each have characteristic susceptibilities, as well as field and temperature dependencies, which contain important magnetic moment alignment and magnitude information.

1.1.1.2 Magnetic Classification[3-18]

When classifying a material, there are two possible groups that it can fall into based on its magnetic behavior. The first, which involves no interactions between magnetic moments, are diamagnetism. With diamagnetism, the material contains no

unpaired electrons and, therefore, no net magnetic moment. When the material is exposed to an external magnetic field, it will magnetize in an opposite direction of the applied field and the number of field lines passing through the material is less than if they were passing through a vacuum of the same size and volume. Figure 1.1.1.2.1 is a good illustration of this phenomenon.

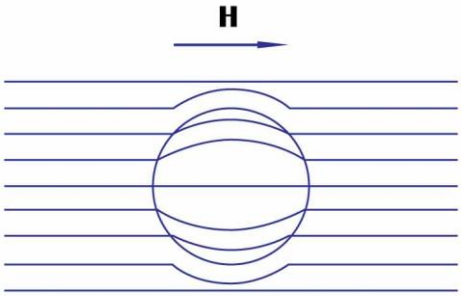

Figure 1.1.1.2.1: Diamagnetic material in an applied magnetic filed.

These types of materials usually have negative susceptibilities and a permeability value less than one. Any material that contains paired core electrons will exhibit small diamagnetic behavior, though its magnitude is much less when compared to magnetic materials.

The second classification group is paramagnetism, which involves materials that contain unpaired electrons; however, the overall magnetic moments still do not interact with one another. When the material is placed in an external magnetic field, the number of force lines passing through it is slightly more than a vacuum of the same shape and size. This can be seen in Figure 1.1.1.2.2.

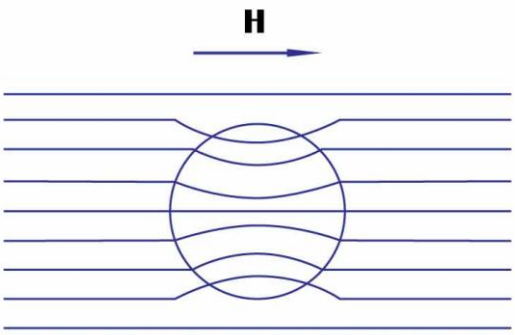

Figure 1.1.1.2.2: Paramagnetic material in an external magnetic field.

For materials that contain non-interacting localized electrons, the Langevin model says that, because of thermal agitation, the magnetic moment is randomly oriented. When the material interacts with an external magnetic field, the moments align with the field. With an increase in temperature, the thermal agitation also increases, resulting in an increased difficulty in aligning the magnetic moments. The relationship between a material's susceptibility and temperature is described by Curie's Law

$$\chi = \frac{C}{T} \qquad (1.1.1.2.1)$$

χ is a material's susceptibility, C is its Curie constant, and T is temperature. This law is only applicable to systems that contain non-interacting magnetic moments. Paramagnetic material will have a positive susceptibility and a permeability greater than one.

Ferromagnetism, antiferromagnetism, and ferrimagnetism all fall into the category of paramagnetic systems that have either a positive or negative exchange interactions between neighboring magnetic moments. In ferromagnetic materials, the magnetic

moments, due to lattice arrangements, will align parallel to each other and will have a positive exchange interaction. It was proposed by Weiss that within these materials there are domains where the magnetic moments will align with respect to one another. When placed in an external magnetic field, the domain walls will move and result in an induced magnetic moment. Due to this relationship of external field and induced magnetic moment, magnetic susceptibility is much less important than saturation magnetization when comparing ferromagnetic materials. When ferromagnetic materials are heated, their saturation magnetization decreases until a critical temperature, T_C (Curie temperature, see Figure 1.1.1.2.3 b). Above this temperature, the material will behave like a paramagnetic material due to the large thermal fluctuations overriding the exchange interactions of the magnetic moments. At temperatures above T_C, the material's susceptibility will vary according to Curie-Weiss Law

$$\chi = \frac{C}{T - \theta} \qquad (1.1.1.2.2)$$

θ is a temperature constant. Below a material's T_C, θ will be positive, while its susceptibility is quite large, and contains a permeability much larger than one.

Antiferromagnetism involves materials that contain magnetic moments that are of the same magnitude and have a negative exchange interaction. These materials will exhibit diamagnetic behavior unless heated, where they will show paramagnetic properties because of the statistical alignment of magnetic moments. The critical temperature where antiferromagnetic materials will switch from diamagnetic properties

to paramagnetic properties is known as T_N (Néel temperature, see Figure 1.1.1.2.3 c). These materials have a positive susceptibility and a permeability greater than one.

Ferrimagnetic materials possess a negative exchange interaction between magnetic moments that results in an antiparallel alignment, but because of the difference in magnitude of the moments, they still contain a net positive moment. This results in magnetic behavior similar to ferromagnetic materials but with a lower saturation magnetization.

The reason behind the various temperature dependence of susceptibility of magnetic materials can be explained simply. In paramagnetic materials, when an external field is applied, the unpaired electrons will align with the field. But since there is no exchange interaction, the overall susceptibility is rather small. In ferromagnetic and ferrimagnetic materials, when in the presence of a field, their magnetic moments will align parallel with the field, and thanks to the strong exchange interactions, the net magnetic moment is amplified and thus increases the susceptibility. In antiferromagnetic materials, the antiparallel alignment of moments causes a complete cancellation, and so only a small susceptibility is observed. As the temperature of these different systems increases, there is an accompanied increase in structural disorder. This structural disorder will have an effect on magnetic properties. In paramagnetic materials, as the temperature increases, there is a partial cancellation of the ordering of the moments and results in a reduced susceptibility. In the cases of ferromagnetism, antiferromagnetism, and ferrimagnetism, the structural disorder will cause disorder in the parallel and antiparallel alignments. For ferromagnetic and ferrimagnetic materials, this results in a decrease in

susceptibility, while in antiferromagnetic materials, the susceptibility will increase due to an imperfect cancellation of the magnetic moments.

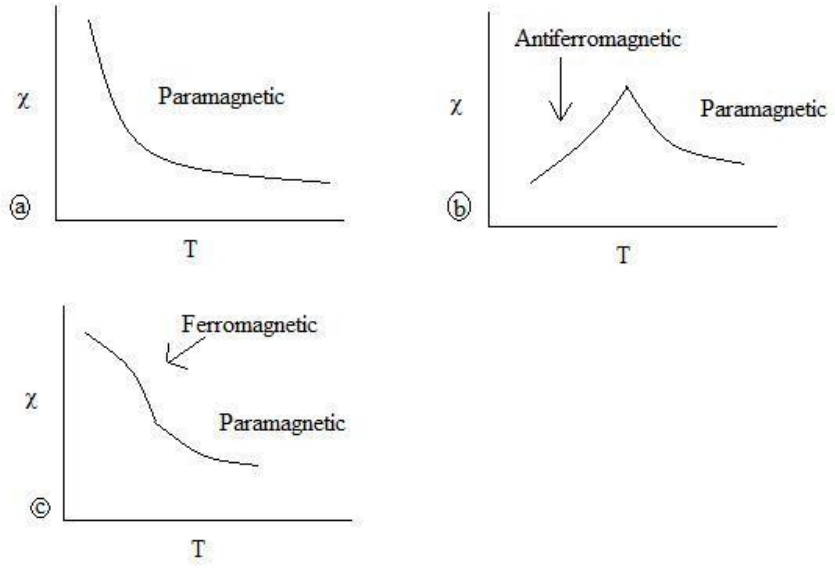

Figure 1.1.1.2.3 Magnetic Susceptibility as a function of temperature for (a) paramagnetic (b) ferromagnetic and (c) antiferromagnetic materials.

1.1.1.3 Magnetic Moment Calculation[19-23]

The motion of an electron's angular momentum and spin results in the magnetic property of unpaired electrons. In 3-d metal cations, the electron's spin contribution is more important than the angular momentum. In the simplest terms, one can view an electron as a spinning negative charge. This results in a spin moment (μ_s) of 1.73 Bohr Magnetons (BM) where *BM* can be defined as

$$1BM = \frac{eh}{4\pi mc} \qquad (1.1.1.3.1)$$

e is the charge of the electron ($1.602 \bullet 10^{-19}$C), *h* is Plank's constant ($6.626 \bullet 10^{-34}$Js), *m* is the electron's mass ($9.109 \bullet 10^{-31}$kg) and *c* is the speed of light ($2.99 \bullet 10^{8}$m/s). μ_s for a single electron can be calculated using

$$\mu_s = g_e[s(s+1)]^{1/2} \qquad (1.1.1.3.2)$$

g_e is the electron g-factor (~2.00), *s* is the spin quantum number of a single electron (1/2). For atoms containing more than one unpaired electron, the equation changes to

$$\mu_s = g[S(S+1)]^{1/2} \qquad (1.1.1.3.3)$$

where *S* is the sum of the spin quantum number of each unpaired electron. When working with atoms where orbital angular momentum (L) cannot be ignored, the equation is expanded to

$$\mu_s = g_J([S(S+1)]^{1/2} + [L(L+1)]^{1/2}) \qquad (1.1.1.3.4)$$

1.1.1.4 Hysteresis[24-26]

Permanent magnets are magnetic materials whose magnetic moments do not relax to zero when an applied magnetic field is removed. In order for the moments to relax, an opposite applied magnetic field is required. A hysteresis loop is the result of field

dependent measurements of magnetic moments. In this measurement, the magnetic moment of a system is measured as a function of changing magnetic field strengths. Figure 1.1.1.4.1 shows an illustration of a representative hysteresis loop.

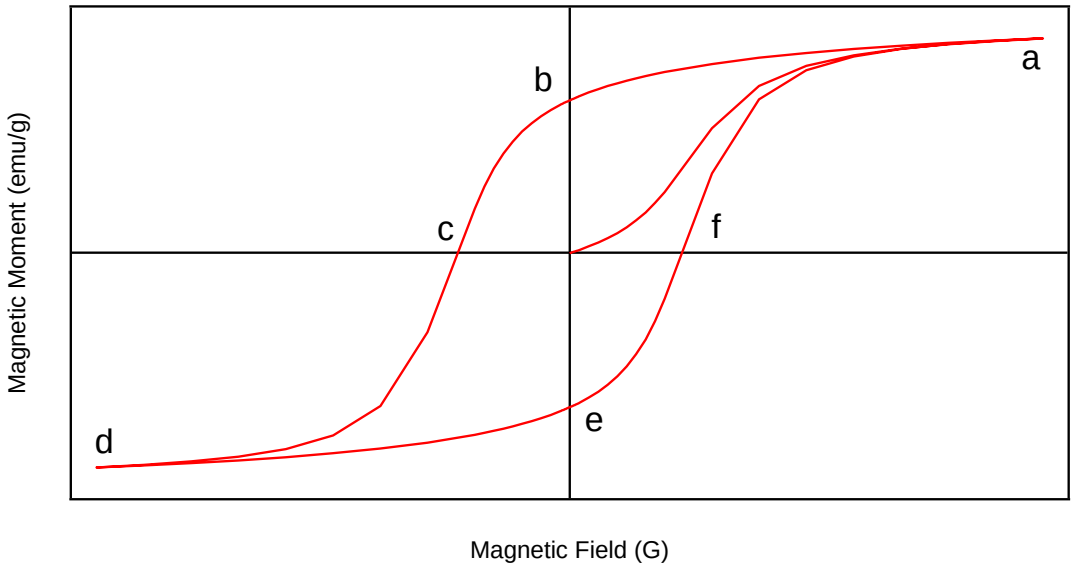

Figure 1.1.4.1: A typical hysteresis loop.

Points (b) and (e) mark the remnant magnetization (M_R). This is the magnetization a system will retain once the applied field is removed. The points labeled (c) and (f) mark the coercivity (H_C) which is the magnetic field strength needed to reverse the direction of the magnetic moments and to remove this retained magnetization. Points (a) and (d) mark the saturation magnetization (M_S) which is the maximum amount of magnetization that a particular system can achieve when placed in an applied magnetic field.

1.1.2 Domain Theory[27-32]

The internal magnetic moments of ferromagnetic and ferrimagnetic materials can be induced by a small external field, even on the order of the earth's magnetic field strength (300-600mG). This is due to the existence of small regions in the material called magnetic domains. These domains range in size from 1-100μm and are separated by domain walls. Within these domains, the magnetic moments will align in a certain direction, but may not be the same direction as the moments in a neighboring domain. The moments may align, however, with a crystallographic axis, which is referred to as the easy axis. When the grain size of ferromagnetic and ferrimagnetic materials are reduced, it can show multi-domains, single domains, or superparamagnetism.

Ferrimagnetic and ferromagnetic materials exhibit temperature dependent saturation magnetization that results from spontaneous magnetization as well as a net magnetic moment that is slightly dependent on the strength of an applied external magnetic field. It has been shown that despite the nonuniform direction of magnetization from one area to another, a material will have a uniform magnitude of saturation magnetization in materials that are homogeneous. Uniform saturation magnetization is possible when one of two things happens: the presence of a strong applied magnetic field or the absence of domain walls. Domains form in order to reduce the magnetostatic energy of a system that arises from surface charge distribution. Consider, for a moment, a bulk material that is magnetized as one large domain. When magnetized, the material develops surface charges at the end of each pole, which creates a local magnetic field. If the magnetization were to split into two opposite poles, the magnetostatic energy would drop by half. With this is mind, it makes sense that the magnetic domains will divide into

smaller and smaller regions until there are an equal number of domains. This process does not go on forever, as there is an energy requirement for the formation and maintenance of domain walls. The existence of these walls is gleaned by the variation of coercivity and remnant magnetization with a change in grain size.

1.1.2.1 Multi-Domain Theory[33-36]

A bulk material is a multi-domain structure due to the fact it contains a collection of magnetic domains. In the absence of a magnetic field, the magnetic moments in each domain will align with respect to one another but will not necessarily align with moments in neighboring domains. This can change if a magnetic field is applied. Even in a weak field, the magnetic moments in neighboring domains will align with respect with one another and in the same direction as the applied field. An illustration of this can be seen in Figure 1.1.2.1.1

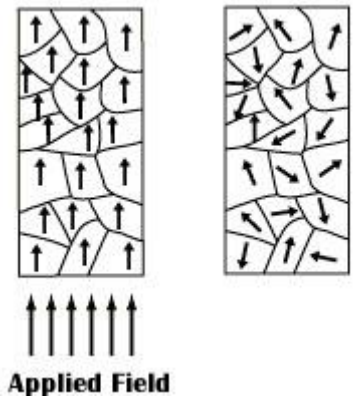

Figure 1.1.2.1.1: Magnetic alignment of a multi-domain structure without and with an applied field.

There have been studies into the process of how the magnetic moments align in multi-domain materials. They reveal that it is not just a simple alignment of the moments, but rather, the movement of domain walls. When a multi-domain material is in the presence of an applied field, the domain walls move in favor of domains that are already in the direction of the applied field. The domains that are not in the direction of the applied field shrink in size while the domains that have magnetic moments in the correct orientation become larger. Figure 1.1.2.1.2 is an illustration of this process.

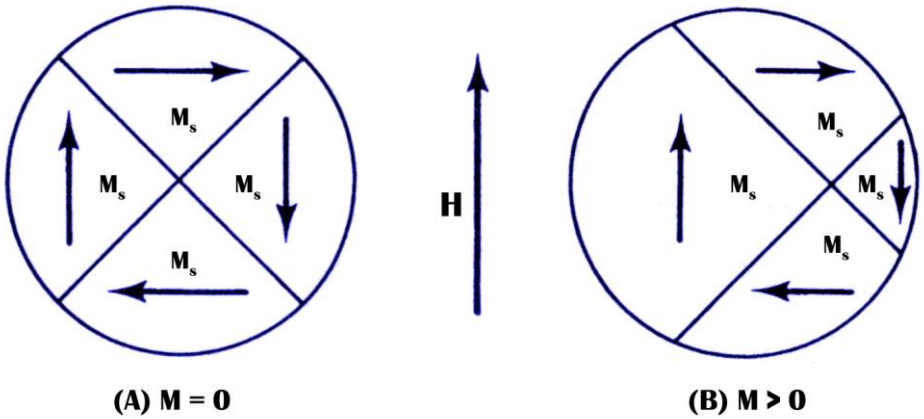

Figure 1.1.2.1.2 Magnetic domain movement without an applied field (a) and with an applied field (b).

1.1.2.2 Single Domain Theory[37-39]

A material will become a single domain state when the grain size is reduced past a certain critical point. When this occurs, there is no longer a domain wall, and all the domains are separated from one another. This results in uniform saturation magnetization, as well as uniform magnetization. In multi-domain systems, changing

magnetization is an energetically energy easy process as domain walls can be moved under a weak field. Magnetization of the single domain system involves the physical rotation of the particle which requires more energy. The end result is that multi-domain systems are magnetically soft with low coercivity and remnant magnetization values, and single domain systems are magnetically hard with much higher values of coercivity and remnant magnetization.

1.1.3 Superparamagnetism[35,40-49]

As the grain size of a material is reduced past a certain point, it will exhibit a remnant magnetization and coercivity of zero. At this point, the magnetization of this single domain material is collinear with its easy axis of magnetization. As temperature increases, there is enough thermal energy, which results in random fluctuations of the magnetization, and a single domain material acts like a paramagnetic material. These materials show paramagnetism even at temperatures below their Curie Temperature, the temperature needed to overcome coupling force between neighboring atoms in ferromagnetic materials. The difference in single domain nanoparticles is that the magnetic susceptibility is much higher than a normal paramagnetic material, and the magnetic moment is due to one particle containing ~10^5-10^6 atoms. Superparamagnetism is the formation of a superspin with a large magnetic moment per particle.

Coherent rotation of a particle's magnetization can be used to describe the particle's reversal of magnetization, as discovered by Stoner and Wohlfarth. They used the following equation to describe the magnetic anisotropy of a non-interacting single domain particle with a uniaxial anisotropy

$$E_A = KV\sin^2\theta \qquad (1.1.3.1)$$

E_A is the energy barrier of the nanoparticle, K is the magnetocrystalline anisotropy constant, V is the particle's volume, and θ is the angle between the particle's magnetic moment and its easy axis. When the magnetic moment is parallel/antiparallel to the easy axis, the anisotropy of the particles is at its minimum. Figure 1.1.3.1 is a simple illustration of a potential well model that best describes the anisotropy energy barrier:

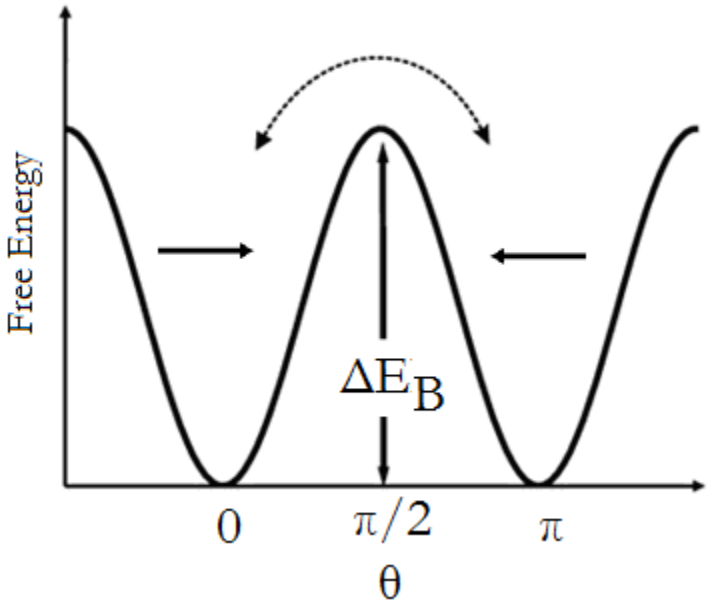

Figure 1.1.3.1 Stoner-Wohlfarth magnetization reversal illustration.

The energy barrier of a particle, when a magnetic field (H) is applied in the easy axis direction, can be best described as

$$E_A = KV\sin^2\theta - \mu H\cos\theta \qquad (1.1.3.2)$$

μ is the total magnetic moment of the particle. This equation shows that when the volume or the magnetocrystalline anisotropy is decreased to a single domain nanoparticle, the E_A will become comparable to thermal energy, which results in random fluctuations in the magnetic moment at temperatures lower than the material's Curie temperature. When there is a change in temperature or field strength, there is a characteristic relaxation time for the magnetization of a particle to reach equilibrium. Néel described this relaxation time, τ, as

$$\tau = \tau_0 e^{(-KV/kBT)} \qquad (1.1.3.3)$$

τ_0 is an attempt frequency factor, $\sim 10^{-9}$s, which is usually treated as a constant, but depends on temperature, magnetic field, magnetization, particle size, gyromagnetic ratio, and dampening constant.

A particle's blocking temperature (T_B) is the temperature above which the particle shows superparamagnetism, and below which shows ferrimagnetism or ferromagnetism. The blocking temperature is related to the anisotropy energy barrier, and is dependent on the particle's composition, volume, and shape. If the measuring time is shorter than the relaxation time, the material appears to be blocked and will show ferrimagnetism/ferromagnetism. If, on the other hand, the measuring time is longer than the relaxation time, the magnetic moment will fluctuate rapidly, and the particle will exhibit superparamagnetism.

1.2 Applications of Magnetic Nanoparticles and Metal Oxide Nanoparticles

1.2.1 Catalyst Supports/Catalysts[50-52]

Due to their ability to participate in both acid-base and redox reactions, metal oxides are quite useful as catalysts for industrial chemical synthesis. Transition metal oxides, such as MnO and Mn_3O_4, are used extensively in industry today for the selective oxidation of hydrocarbons. Industrial preparation of many of the monomers useful for synthetic plastics is created using hydrocarbon oxidation via transition metal catalysts. As the supply of low cost hydrocarbons drops and energy costs increase, metal oxide catalysts need to become more efficient and cheaper to produce. Since the site of the oxidation reactions occurs at surface oxygens, metal oxide nanoparticles, with an increased ratio of surface area to volume, becomes more efficient. If the metal oxide were immobilized on a magnetic core, collection and separation of the catalyst from the reaction mixture, become more energy efficient, as only a magnetic field would be required.

Recycling catalysts is of particular interest, especially if the catalyst is expensive. Immobilization of catalysts on micrometer material has been used for many years now and allows for the separation of the catalyst from product via a filtration process. A way to improve this separation efficiency is by the use of magnetic nanoparticles. Again, due to their high surface area, the loading of catalysts is much higher and allows for easier access to the catalysts' active sites. Another advantage of the use of magnetic nanoparticle catalyst supports is the ability to "turn off" a reaction by moving the catalysts out of the reaction with an applied magnetic field. This also allows for the easy recovery of the catalyst at the end of the reaction.

1.2.2 Magnetic Microwave Technologies[50,53-61]

Over the last century, there has been an increase in the demand for signal processing devices for communication, radar, and other similar instrumentations. Along with this increase for processing devices, microwave technology is moving to higher frequencies requiring the use of nonconducting materials to ensure full electromagnetic penetration. Another required property for these materials to be able to be integrated into these devices is microwave permeability. This property describes the response of induction to an oscillating magnetic field. One of the best materials for microwave processing materials is nanometer ferrites and garnets due to their magnetic property tailorability, low eddy current losses, high permeability, and simple and cheap preparations.

The application of planar microwave magnetic devices range from isolators, phase shifters, patch antennas, and circulators. The most important class of applications from that list is the circulators which are commonly used in phone and radar equipment where the same device is used to transmit and receive a signal. Figure 1.2.2.1 shows an illustration of a circulator. The permanent magnets provide the field needed to bias the soft magnetic material. When a high power signal is transmitted, the circular bias causes it to travel from port I-port II (such as sending a signal). When a low power is utilized, the material bias causes it to travel from port III-port I (such as receiving a signal).

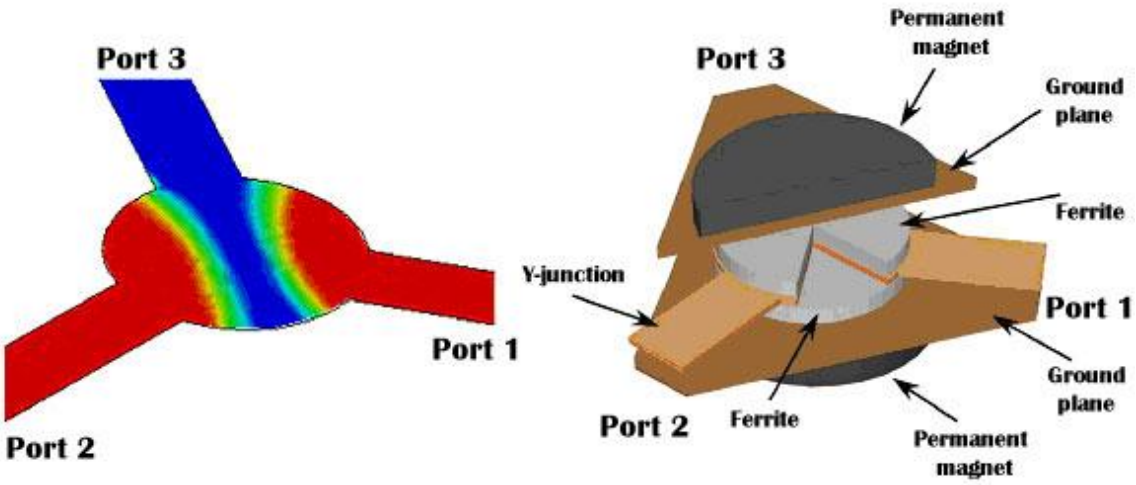

Figure 1.2.2.1 Illustration of a circulator.

Over the past decade, there has been an increase in applications utilizing wireless technologies that use their own frequency standards. In order to reduce production costs, there has been a strive to develop devices with frequency tunable systems. A solution lies in magnetostriction, which is a property inherent in magnetic materials and easily exploited in ferrites and garnets.

1.2.3 Sensors[62-69]

There are several properties of magnetic metal oxide nanoparticles that make them suitable for sensor applications. Coercive field dependence on surface chemistry is the first. The coercivity of the nanoparticles can change drastically depending on the surface environment. Magnetostriction, a property where stress on the nanoparticle produces a change in magnetization and inversely a change in the magnetic field induces

a dimensional change, is another useful property for the incorporation of these oxide materials in sensors.

Magnetic response, i.e. coercivity changes, utilizes fundamental properties of magnetic metal oxide nanoparticles. When a material's grain size is reduced to the nanometer scale, the surface area to volume ratio increases, which results in a high responsiveness to surface changes. More sensitive sensors can be developed by investigation into surface anisotropy effects on coercivity experienced in magnetic nanoparticle systems.

One general magnetostriction sensor is known as a liquid level sensor. Changes in position, caused by strain due to a magnetic field, are monitored. Floating in a solution is a moveable magnet that interacts with magnetic nanoparticles and causes a dimension change that is monitored as movement in the magnet. An advantage of this system is the absence of physical contact of any of the parts, and thus wear and tear is quite minimal.

Current sensor technologies used by industry today utilize high cost rare earth metals. Magnetic metal oxide nanoparticles, such as spinel ferrites and manganese oxides contain the necessary properties, such as chemical and thermal stability, that will allow them to become useful for sensing applications.

1.2.4 Biomedicine[70-74]

Metal oxide nanoparticles, namely magnetic nanoparticles, are of great interest in biomedicine due to the ability to manipulate the particles with an external magnetic field. The ability to direct the delivery of drugs using a magnetic field has generated much

interest. Other applications of these magnetic nanoparticles include cell separation/extractions as well as cell/drug manipulation via magnetic fields.

MRI (nuclear magnetic resonance imaging) is another area in biomedicine that has benefited from the application of magnetic metal oxide nanoparticles. MRI is a powerful noninvasive tool used in medicine but suffers from low signal sensitivity. The use of contrast agents aids in this, however, suffers from their own drawbacks. The most common contrast agent used is paramagnetic materials that utilize T_1 relaxations (the time constant of the return movement of protons to applied field direction). Superparamagnetic metal oxides, such as $CoFe_2O_4$, effects T_2 relaxation times (the time constant of relaxation of protons interfering with each other) by altering local magnetic fields surrounding protons.

A third interesting application of metal oxide nanoparticles is hyperthermia treatment, using a magnetic field to heat up magnetic nanoparticles. Localized heating in specific locations can be achieved through the use of an alternating magnetic field and magnetic nanoparticles. The nanoparticles heat up due to one of two things: reversal of magnetic spins within the nanoparticles or physical rotation of the nanoparticle in a viscous solution. Magnetic hyperthermia is being investigated for its application into the treatment of cancer treatment.

1.3 Spinel Ferrites, Garnets and Perovskites

1.3.1 Spinel Ferrites[4,5,35,75-77]

Spinel, named for the mineral $MgAl_2O_4$, is a class of minerals with the generalized formula AB_2O_4 where *A* represents tetrahedral sites, and *B*, octahedral sites,

formed by the cubic close packed lattice of oxygen. A general representation of the spinel formula cell structure can be seen in Figure 1.3.1.1. There are 64 *A* sites, of which only 8 are occupied, and 32 *B* sites, of which 16 are filled. In spinel ferrites, the *B* sites are usually occupied by Fe(III) ion, while the *A* sites are occupied by divalent cations such as Zn^{2+}.

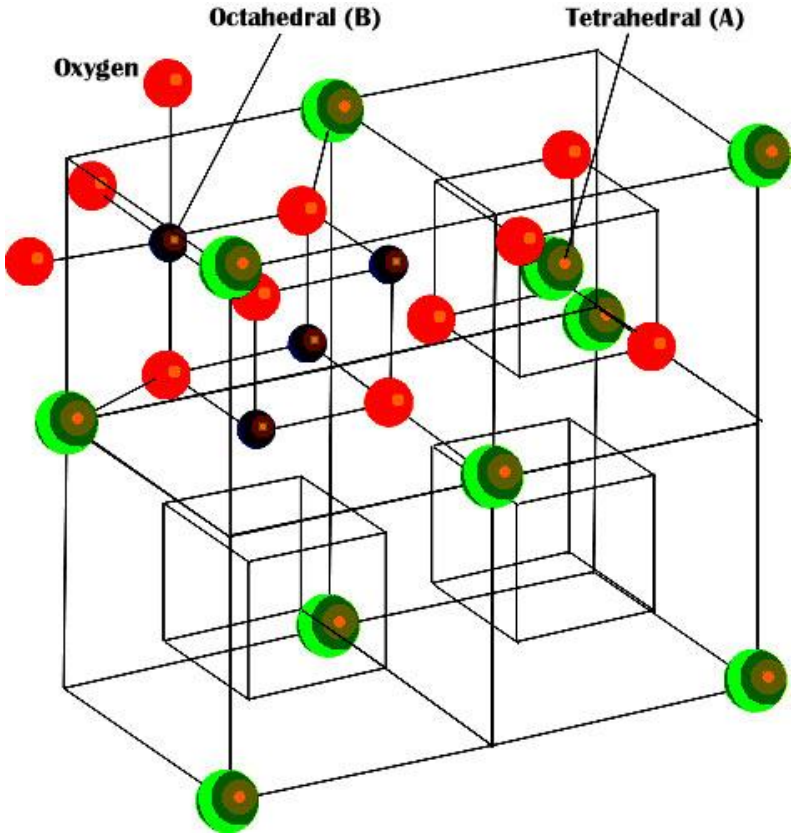

Figure 1.3.1.1 Spinel (AB_2O_4) unit cell with A tetrahedrally coordinated and B octahedrally coordinated.

There are two extreme types of spinel ferrites, inverse and normal. A cation ratio of 1:2 (A:B) results in a normal spinel. A general formula for normal spinels is

$$[A]^{tet}[B_2]^{oct}O_4$$

For inverse spinel ferrites, half of the Fe(III), from the normally occupying *B* sites occupy *A* sites instead and the remaining divalent cations from the *A* sites occupy the *B* sites. A generalized formula develops and is best viewed as

$$[B]^{tet}[A,B]^{oct}O_4$$

A third spinel ferrite type is possible when there is a random cation distribution of both *A* and *B* sites and can be thought of as

$$[B_xA_y]^{tet}[A_{1-x}B_{2-y}]^{oct}O_4$$

Most magnetic ferrites are inverse spinels, due to the Fe^{3+} being a d^5 ion with no crystal field stabilization energy in the *B* sites. The large M^{2+} ions will prefer to occupy *B* sites over *A* sites, while the Fe^{3+} will occupy both *A* and *B* sites.

1.3.1.1 Magnetic Properties of Spinel Ferrites[4,5,35,75-77]

Antiferromagnetism arises in spinel ferrites that are a result of the cation site alignment. The *B* site cations align magnetic moments parallel with respect to each other, while the *A* site cations align parallel with other *A* site cations. The *A* site cations align antiparallel to *B* site cations resulting in antiferromagnetism. However, since there are more *B* site cations than *A* site cations, there is not a full cancellation of magnetic

moments, and ferrimagnetism arises from this system. A representation of this behavior can be best viewed in Figure 1.3.1.2

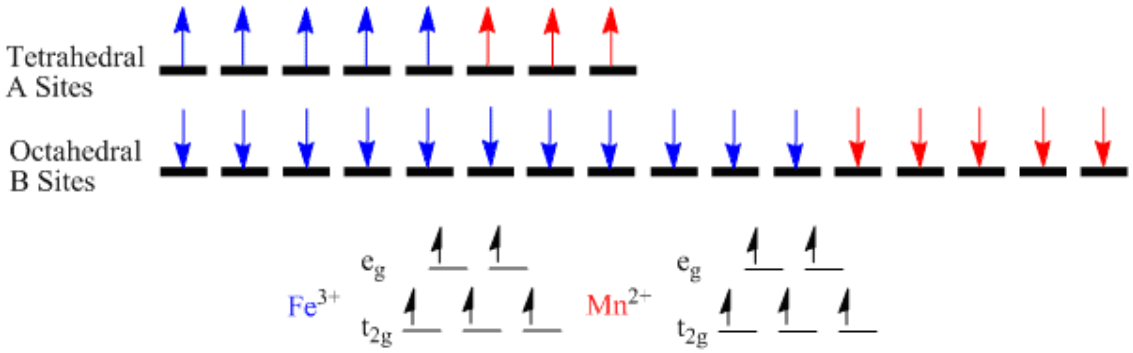

Figure 1.3.1.2 Unequal antiparallel alignment of magnetic moments in manganese ferrite.

As shown, the *A* sites only partially cancel out the *B* site cations, and there is a net magnetic moment in the downward direction in this example. This results in an overall magnetic response.

1.3.2 Garnets[36,77-81]

Garnets are a group of minerals that have a complex cubic structure. One of the most common garnets that has been studied is $Ca_3Al_2(SiO_4)_3$. A general formula for iron garnets can be written as

$$Me_3Fe_5O_{12} \qquad \text{(Me = Er, Dy, Sm, Y, etc)}$$

Similar to spinel structures, there are eight formula units contained in the unit cell. There are two different cations that occupy three different sites within the garnet structure. Figure 1.3.2.1 best illustrates this structure

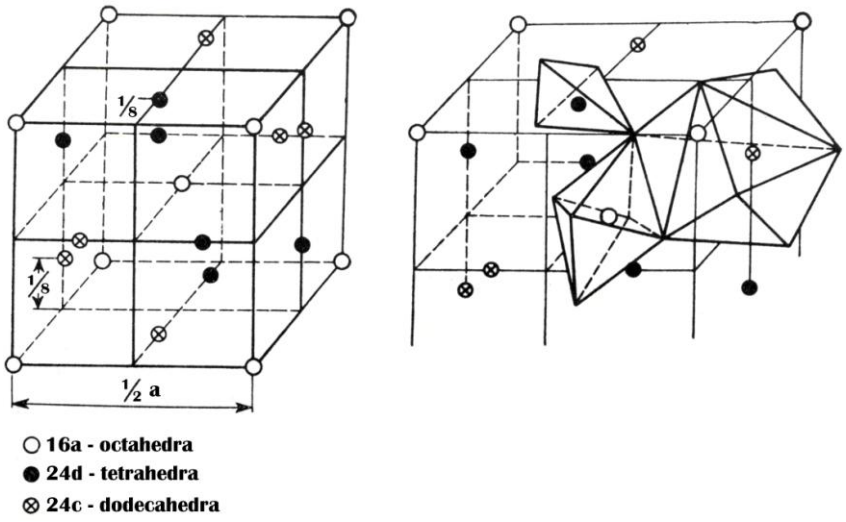

Figure 1.3.2.1: Formula structure of garnet.

Within the garnet structure, the Me^{3+} cation will occupy the *c* sites, while Fe^{3+} will occupy the *a* and *d* sites. The unit cell consists of 24 Me^{3+} within the *c* sites, 16 Fe^{3+} in the *a* sites, and 24 Fe^{3+} in the *d* sites. The oxygen atoms form different polyhedra around the various metal cations. The polyhedra around the *c* sites are dodecahedra, while the ones formed for the *a* and *d* sites are octahedra and tetrahedra respectively. Figure 1.3.2.2 shows this coordination environment for the various sites.

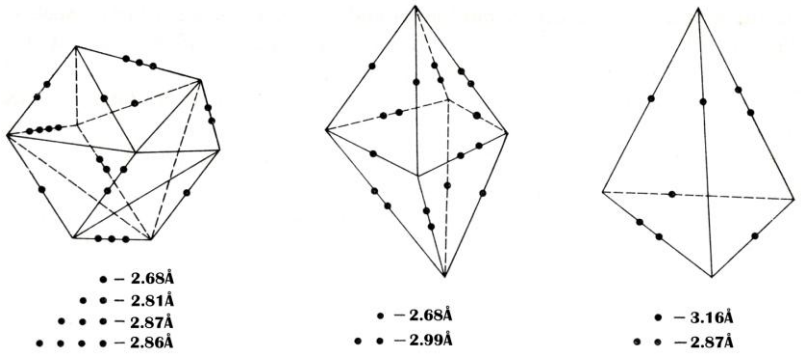

Figure 1.3.2.2: Polyhedra of the different sites within garnet.

1.3.2.1 Magnetic Properties of Garnets[72-76,36]

The garnet unit cell is rather large, containing 160 atoms, with three different sites: *A*, *B*, and *C*. Standard occupancy of the sites are

$$16Fe^{3+}(A),\ 24Fe^{3+}(B),\ 24Me^{3+}(C)$$

There is an antiparallel alignment between the iron of the *A* and *B* sites. The Me^{3+} cations' magnetic moments align antiparallel to the resulting magnetic moment of the *A* and *B* irons. In Yttrium Iron Garnets (YIG), the Y^{3+} provides no magnetic moment to the *C* sites and the resulting magnetic moment of the system is due solely to the imbalance of the iron distribution between the *A* and *B* sites.

1.3.3 Perovskites[77-80,82]

Perovskites belong to a class of oxides whose general formula is ABO_3, and have a structure based on ReO_3. A general way to view this structure is a close packed array host lattice ($[BO_3]_\infty$ that have corner sharing octahedral BO_6 that form cages using twelve oxygen atoms where the *A* cation is located. Figure 1.3.3.1 shows this structure.

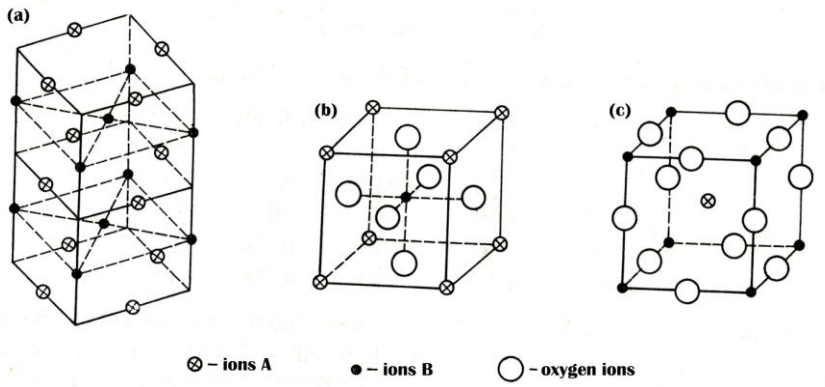

Figure 1.3.3.1: Perovskite structure. a) metallic ion arrangement b) and c) *A* and *B* site relation to oxygen ions.

This structure can result in a distorted cubic cell. Perovskites have three classifications

$A^{I}B^{V}O_3$ (A: Na, Ag; B: Nb Ta)

$A^{II}B^{IV}O_3$ (A: Ba, Sr; B: Ti, Sn)

$A^{III}B^{III}O_3$ (A: Ln, Y; B: Fe, Cr)

The perovskites that are covered in this thesis all belong to the third class and will involve yttrium and iron in the *A* and *B* sites, respectively. The stability of perovskites depends on the electronic structure of the *B* cations as well as the relative sizes of the *A* and *B* cations. The stability of these structures can be characterized using a coefficient that Goldschmidt determined

$$t = \frac{r_A + r_B}{\sqrt{2(r_B + r_O)}} \qquad (1.3.3.1)$$

$r_{A,B,O}$ are the atomic radii of the ions in the *A* and *B* sites as well as oxygen. If *t* is between 0.8-1, the perovskite will be regular. When *t* is less than 0.8 or larger than 1.0, then there will be a distortion of the structure. $YFeO_3$ structure is in fact distorted and will be orthorhombic, with a space group classification of $D_{2h}^{16} - Pb|n|m$.

1.3.3.1 Magnetic Properties of Perovskites[77-80,82]

Perovskite is a useful material for probing the interactions of cations with uncompensated electrons. Looking at the site occupancy of the $YFeO_3$ perovskite structure, it is easy to think of the iron occupying only one site (4b) and the Y occupying only another site (4c). If the exchange interaction between those sites is antiferromagnetic, then the overall structure should be antiferromagnetic with the magnetic moments compensated; however, this is not the case. Magnetic investigations show the material as weakly magnetic, in that the magnetic moments are not completely compensated. The above antiparallel arrangement of the iron is based on an analogy to a normal spinel structure, where there is an antiparallel exchange interaction between *A* and *B* sites. The difference between the spinel and the perovskites lies in the strength of that exchange interaction. In spinels, it is much larger than in perovskites. The resulting magnetism in perovskites can be due to a few things including a nonperfect antiparallel alignment of the cations and the weak exchange between the iron and yttrium that is either ferromagnetic or antiferromagnetic. When moving through one node of the crystal lattice to another, the spins located there can orient parallel or antiparallel. This is known as a collinear structure. If the spins change their orientation through an angle, these structures are called non-collinear. Perovskites that are weakly ferromagnetic and contain

a nonmagnetic ion in the *A* site, such as $YFeO_3$, belong to the non-collinear classification. This weak magnetism occurs due to the iron that are at the correct nodes and are almost fully antiparallel, which causes an incomplete compensation. The canting angle in $YFeO_3$ is 8.9mrad and is enough to give rise to ferrimagnetic behavior. Also, the weak ferromagnetism is related to lattice symmetry and therefore also related to crystal field symmetry.

1.4 Synthesis Methods for Metal Oxide Nanoparticles

Over the past two decades, new synthesis methods for the production of metal oxide nanoparticles have been routinely reported. These new methods range from novel schemes to slight changes to known procedures that provide for the production of a certain desired trait or product. There are several different ways to compare synthesis techniques to evaluate them, such as product yield, product quality, etc. For the purpose of this thesis, I will be using the industrial viability to appraise various methods. This means I will be looking at various factors deemed important to an industrial scale production of nanoparticles. These factors are cost, recyclability, product quality and yield, uncomplicated scheme, and reaction versatility for a range of different products.

When considering these factors, one can see that they are connected in one fashion or another. Two ways to keep the overall production cost down is to use simple, cheap precursors and add recyclability to the reaction scheme. Another way to help reduce costs is a simple scheme, in that the more complicated a reaction is, more materials and equipment are needed, resulting in a higher cost. A high yield and good quality product production reduces the need for purification or additional reactions which

also helps reduce production cost. Finally, the ability to produce a wide range of products from the same reaction and equipment, by simply changing precursors, will also reduce costs.

The following subchapters explore several of the better known synthesis methods for metal oxide nanoparticles. The last section describes the aminolytic method, which was developed in the Zhang lab by Dr. Man Han, and its versatility, robustness, and recyclability for the synthesis of spinel ferrites was tested by Dr. Lisa Vaughan. Throughout the rest of this thesis, I will be investigating the ability of the aminolytic reaction in the production of a wide range of metal oxide nanoparticles, such as manganese oxide, garnets, and perovskites.

1.4.1 Co-precipitation Utilizing Micelles[46,83-88]

Microemulsion co-precipitation is a common, well-studied, bottom-up synthesis technique for the production of metal oxide nanoparticles. This method utilizes a solution of water, oil, surfactant, and some inorganic phase to form micelles. Most of these techniques utilize the creation of two batches of micelles, each containing a reactant, which, when mixed, results in the micelles combining. Once this happens, a reaction between the precursors occurs, and the desired metal oxide particles form. The micelles here are acting as microreactors, and the size of the particles formed can be controlled by varying the oil-to-water ratio. The micelles also help prevent aggregation and resulting in narrow size distribution. There are two types of micelles possible: normal and reverse. The surfactant in both cases consists of a long chain hydrocarbon with one end containing a hydrophilic end and the other hydrophobic. In the normal micelle reaction, spherical

micelles form in a water solvent, that is, the hydrophilic end of the surfactant extends into the water. In the reverse micelle method, spherical micelles form in an organic solvent. The hydrophobic end of the surfactant is orientated into the organic phase, while a water droplet forms the micelle.

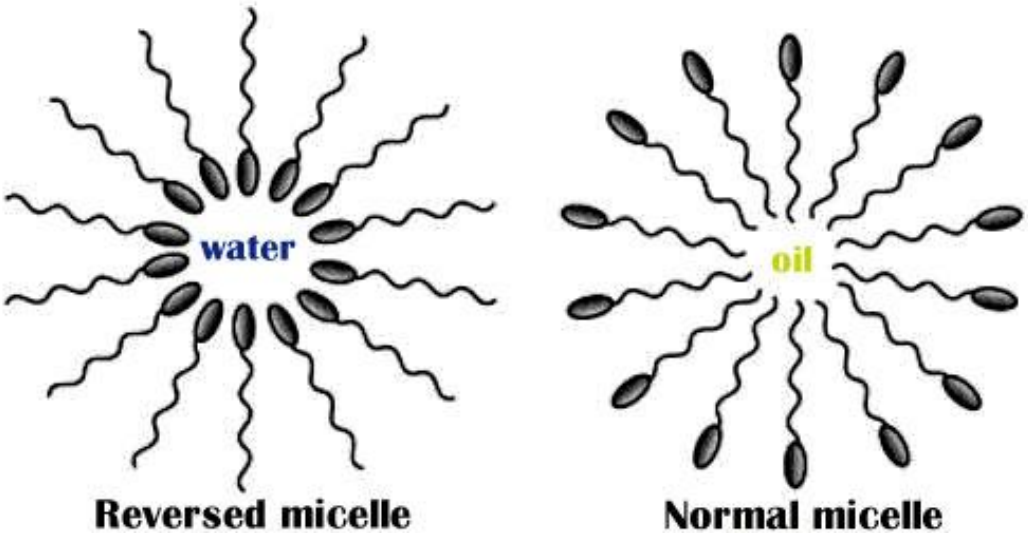

Figure 1.4.1.1 Schematic of a normal (right) and reverse (left) micelle.

One of the advantages of these reactions is reduced crystal lattice defects and cation distributions that are equalized throughout the particles due to the reaction speed being slow. There are several drawbacks, however. The first is low product yield, on the order of 0.8-1.0 g from a single reaction. The second drawback is the high waste production. In a typical normal micelle reaction performed by all first-year graduate students in the Zhang lab, about 2.5 L of waste is produced when making 1 g of sample. In a typical reverse micelle reaction, 1 L of toxic organic waste remains at the end of the reaction. The large amount of solvents and reactants as well as the large amount of waste

by-product results in the cost of this system to be quite high for low production yield. One final drawback is that the product may also require a heat treatment if the desired crystallinity is not achieved in the micelles.

1.4.2 Thermal Decomposition[40,89-93]

In recent years, the thermal decomposition method has been extensively researched for the production of metal oxide nanoparticles, namely due to its ability to produce tunable and highly crystalline products. A generalized reaction scheme for the thermal decomposition method is the decomposition of some precursor in the presence of a surfactant dissolved in a high boiling point, non-reacting solvent. If the desired product is a binary metal oxide, no special attention to precursor decomposition temperature is needed. Though the use of only one precursor limits the reaction to only one product, and if another product composition is desired, a new precursor needs to be developed. However, in a more complicated system such as a ternary system, like spinel ferrites, each precursor's decomposition temperature needs to be considered and matched to one another in order to obtain the desired product. The use of multiple precursors allows for the system to produce a range of particles with various compositions if proper precursors are found and used. More common precursors for the production of metal oxide nanoparticles include metal citrates, metal cuppferrons, and metal acetylacetonates. One of the major drawbacks for this system is the large toxic waste-to-product ratio. The amount of product is quite small, while the amount of waste is rather large.

1.4.3 Hydrothermal[94-96]

The hydrothermal method has been around for well over a hundred years and therefore is a well-established, heavily studied synthesis method especially for the creation of ceramics and metal oxide nanocrystals. The hydrothermal method is a synthesis technique that grows crystals and nanocrystals using reactions (heterogeneous or single phase) in a water medium at elevated temperatures and pressures. Although there are no defined lower limits on temperature and pressure for the hydrothermal method, the majority of procedures found today in the literature use temperatures above 100^{o}C and 1 atm. Upper limits to the hydrothermal reaction conditions include 1000^{o}C and 5000 atm. Most commercial uses of the hydrothermal method utilize temperatures less than 300^{o}C and 500 atm. Figure 1.4.3.1 shows an illustration of hydrothermal oxidation of zirconium powder:

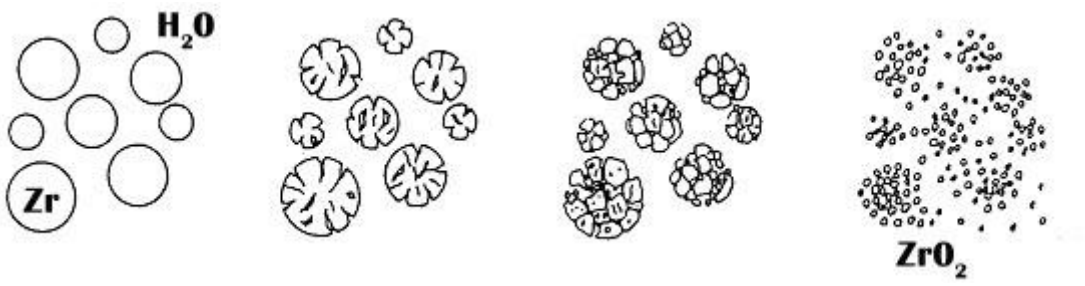

Figure 1.4.3.1 Illustration of a hydrothermal oxidation process used in some hydrothermal methods.

There are several advantages of the hydrothermal method that include aggregate reduction resulting in monodispersity, ability to morphological control of the final products, and crystalline product. Despite these advantages, there are several

disadvantages that render this method inadequate for commercial production of metal oxide nanoparticles. The first is the low amount of product produced. In order to produce the amounts that will be required for applications, the hydrothermal is not efficient enough to meet demands. If larger pressure vessels are used, then there is a danger of possible explosion due to the high pressures needed for the reaction. Another disadvantage is that in most synthesis of metal oxide nanoparticles, there are possible side reactions that will cause impurities in the final product that would need to be removed or purified. Finally, there is the need for capping agents or additional surfactants in order to control morphology of the product that may be dangerous at high temperatures and pressures and can cause the waste generated by the reaction to be toxic.

1.4.4 Sol-gel[77,86,97-101]

Lately, there has been an increase of research into the production of nanoparticles via sol-gel techniques. This reaction scheme produces nanoparticles, usually metal oxides, through the use of a gel matrix to control the mixing of precursors. The reaction usually involves the integration of solution of metal alkoxides (sol) into a polymer matrix (gel). Once the precursors are fully incorporated into the matrix, they undergo a hydrolysis reaction which forms the product. The final step of the reaction is calcination of the sol-gel, which causes the agglomeration of the particles, and usually results in causing polydispersity, depending on heating temperature and duration. One of the advantages of this reaction is the ability to coat nanoparticles to surfaces that allow the matrix to adhere to. Since the reaction is the hydrolysis of metal alkoxides, tailoring of various types of nanoparticles is possible, while the overall reaction is simplistic.

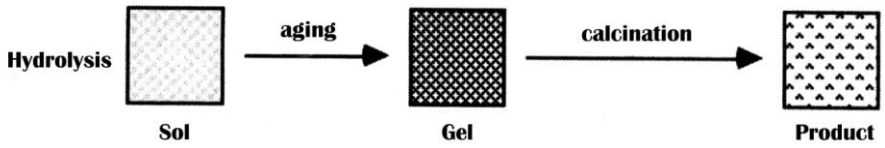

Figure 1.4.4.1 Schematic of Sol-Gel reactions to product various phases of product.

There are, however, several disadvantages to this reaction that prevent it from being used on the industrial scale. The first is the hydrolysis rates of the precursors need to be matched well in order to produce the desired product and crystal phase. The need for the calcination step often results in structure defects as well as polydispersity due to agglomeration. In order to control and eliminate undesired side reactions in the sol-gel, protecting agents are frequently used and complicate the system and oftentimes require additional purification steps to obtain the desired product. Finally, morphology of the particles produced can be problematic to control due to packing densities of the matrices, which result in uneven solvent removal throughout the system. This aspect of the reaction will be magnified if scaled up. This all results in a higher cost for the production of product that may not even be the desired morphology or composition.

1.4.5 Aminolytic Method[102]

Dr. Man Han, while in the Zhang group, developed a version of the thermal decomposition method that he termed the "aminolytic method". This method utilizes the use of metal organic precursors that are suspended with a surfactant (oleylamine) in a high boiling point solvent. This method is an improvement over previous thermal decomposition routes with the application of metal acetate precursors. These acetates are

simple to make and allow for the use of a wide range of metals in various oxidation states, such as Fe, Co, Cr, Mn, etc. Because of the assortment of usable precursors, the application of this synthesis method for the creation of metal oxide nanoparticles is almost never-ending. Dr. Han proposed a possible mechanism for the aminolytic method that is also different from previous thermal decomposition methods. He proposed that the nanoparticles are created in a two-step reaction: an amide bond forms between the acetate and an amine molecule. There is then a proton transfer that causes the formation of a metal hydroxide, which then undergoes a condensation reaction to form the metal oxide. He also proposed that, because the amide bond formation is slow while the condensation reaction is fast, the amide bond limits the amount of metal hydroxide present. This causes a separation of the nucleation and growth stages of metal oxide nanoparticle synthesis and allows for the formation of a monodispersed system. Figure 1.4.5.1 shows Dr. Han's proposed mechanism.

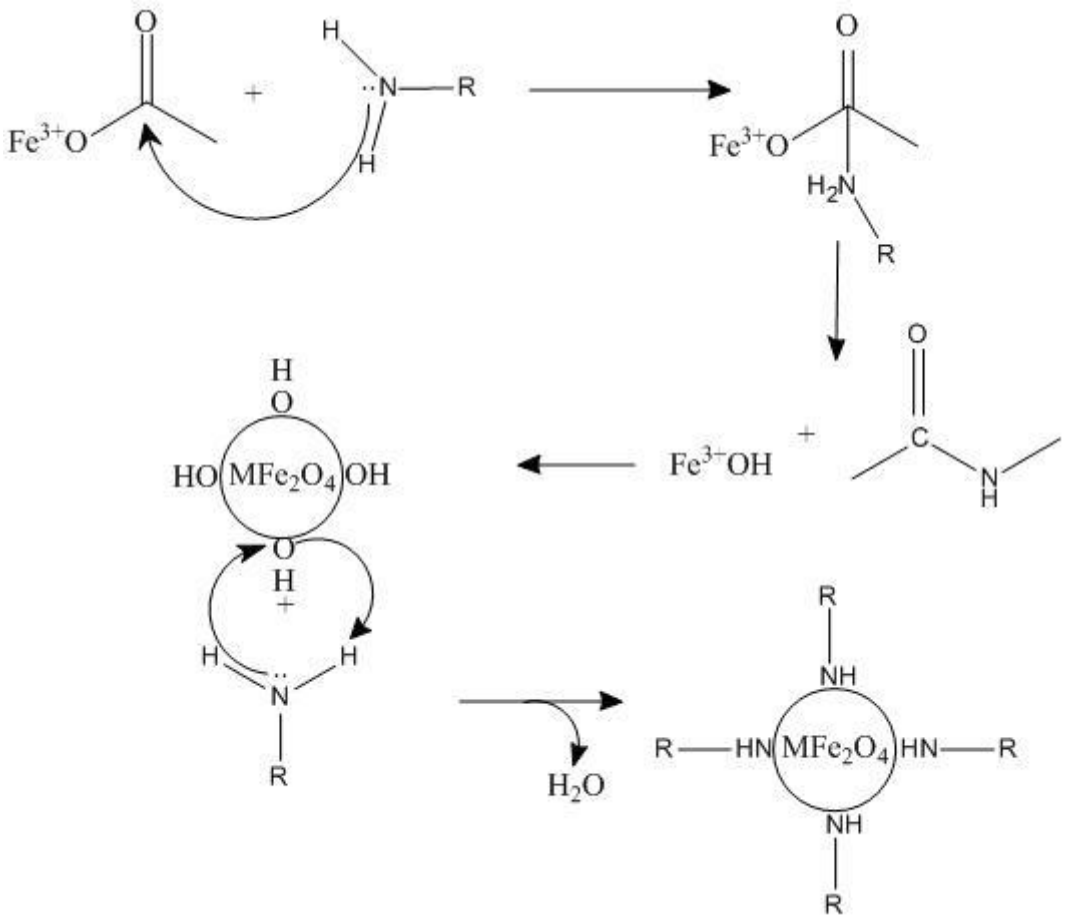

Figure 1.4.5.1: Proposed mechanism for the Aminolytic Method.

The oleylamine in this system serves two functions one as the amine supply and the other as a surfactant. It coats the nanoparticle surface allowing for suspension within the solvent, thus preventing agglomeration, which would cause polydispersity within the product. Since the reaction is controlled by the amide bond formation, there is no longer a need to match the decomposition temperatures of the precursors, which is a major drawback to previous methods. Another advantage of the aminolytic method was proven by Dr. Lisa Vaughan. She tested the recyclability of the this method to investigate if there was any degradation of product yield or crystallinity with repeated use of the high boiling

temperature solvent, dibenzyl ether. Dr. Vaughan showed that the dibenzyl ether could be reused ten times without any lose of product or quality, with an indication of higher repeated use of the solvent. The aminolytic method retains all the advantages of the thermal decomposition method, such as monodispersity and high crystallinity. This reaction method also removes the issue of matching thermal decomposition temperature of the precursors but keeps the superior size control, crystallinity, and a narrow size distribution. The metal acetate precursors allow the synthesis to be used for a variety of materials. Finally the aminolytic method has the advantage of being able to utilize recycled solvents without suffering product loss or degradation

1.5 Instrumentation

1.5.1 Powder X-Ray Diffraction[77,103-108]

Powder X-ray Diffraction (XRD) is a valuable analytical technique that has successfully been shown to be useful for structural analysis for both bulk materials as well as nanoparticles. For the experiments in the following chapters, two lab X-ray diffractometers, all with a Cu-K_α source, were used. The Bruker D8 Advanced X-ray diffractometer was used for nanoparticle analysis, when available and a PDW3050 X-ray diffractometer, which was used on the majority of the analyses of my samples in this thesis.

XRD is a nondestructive and rapid method for determining the crystalline phase of a sample. A simple observation of the pattern can help determine if additional analysis is required of the sample. Comparison of a diffraction pattern of a sample to the pattern

reported in the International Centre for Diffraction Data's Powder Diffraction File (ICDD file number), the sample's lattice planes, crystalline structure, and, in some cases, identity can be determined.

A crystal is a homogenous solid with a repeating 3-D pattern of atoms with a fixed distance between them. Because of this repeating pattern, XRD will result in characteristic peak intensities and positions which correspond to particular crystal phases. Peak width and intensity depend on type of unit cell, position of atoms within the unit cell, thermal motion, and population parameters. Lattice planes within a unit cell are characterized by a Miller Index. These Miller indices can be useful in identifying an unknown sample.

X-ray diffraction patterns are due to the constructive interference of reflected x-rays that satisfy Bragg's Law. An incident x-ray of a fixed wavelength, 1.54 Å for a Cu-K_α source, that interacts with atoms in a crystal will be reflected at different angles. If the interplanar crystalline spacing, *d*, is an integer multiple of the x-ray's wavelength, the diffracted X-ray will constructively interfere. This results in the diffracted X-ray beam possessing the same angle as the incident beam. This relationship is known as Bragg's Law

$$n\lambda = 2d\sin\theta \qquad (1.5.1.1)$$

n is an order of diffraction, λ is the wavelength of the incident beam, *d* is the interplanar spacing of the crystal, and θ is the angle of reflection or incidence. This can be visualized in Figure 1.5.1.1.

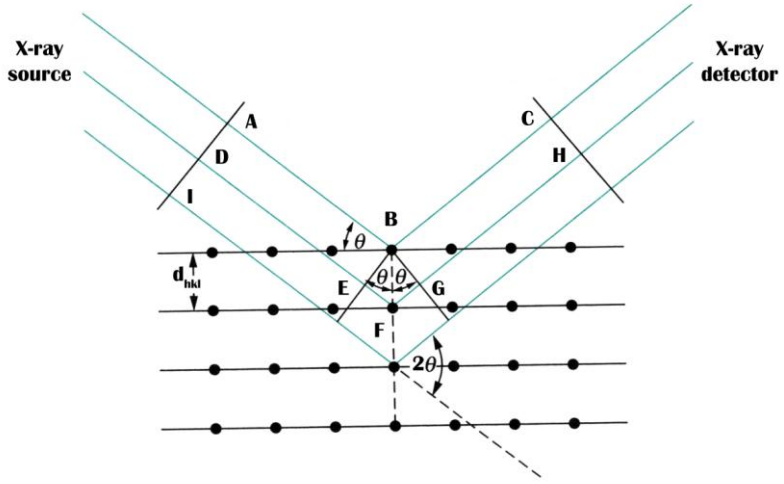

Figure 1.5.1.1 Diagram of Bragg's Diffraction.

Once detected, the diffracted beam intensity is plotted against the corresponding 2θ diffraction angle to obtain the diffraction pattern, which then can be compared to known patterns for identification purposes or used to calculate various parameters.

X-ray diffraction can also be useful to nanochemists, not only in identification of material, but also for the calculation of the average size of nanoparticles. Because there is a finite number of lattice planes that limit interference, the peaks in XRD patterns of nanomaterials broaden. In diffraction patterns, there are three factors that cause peak broadening: strains, faulting, and crystalline domain size. If the sample is fault and strain free, the broadening of the XRD pattern will correspond to the average nanoparticle size. Using a simple equation, the Scherrer equation, the average nanoparticle size can be calculated using the peak broadening. The Scherrer equation is:

$$d = K\lambda/(\beta\cos\theta) \qquad (1.5.1.2)$$

where *d* is the average dimension of the crystal perpendicular to the reflection planes, in nanometers, *K* is the Scherrer constant, a number between 0.87 and 1.0, (0.9 is used for all calculations contained in this thesis), λ is the X-ray wavelength, θ is the Bragg angle, and β is the full width at half maximum (FWHM) in radians. This calculation of the average size of nanoparticles is only valid when there is a single homogenous phase and a narrow size distribution. The average nanoparticle sizes calculated and reported this thesis will be the result of line broadening analysis from their XRD patterns.

1.5.2 Transmission Electron Microscopy (TEM)[109-114]

A highly useful characterization technique for studying nanomaterials is Transmission Electron Microscopy (TEM). TEM allows the researcher to be able to visualize the material they are working with. Being able to see the sample allows for morphology studies as well as the calculation of average size and monodispersity present in the system. In this technique, a beam of electrons pass through a thin sample. When this occurs, a 2-D projection of the sample forms on a screen or photographic film. The TEM studies were performed on a JEOL 100CX2 or a Hitachi TEM HF2000 at the Center of Nanostructure Characterization, Georgia Institute of Technology. Samples were prepared by dispersing 5-10 mg of sample into 5-10 mL of hexanes. A drop of this solution was then placed on a copper grid and allowed to dry.

Conventional light microscopy is limited by the wavelength of visible light and therefore will not be useful for imaging nanostructures. The use of a beam of electrons is a way to get around this resolution problem. Because electrons contain both particle and

wave-like properties, when they interact with matter, they will act like light and scatter or transmit. Optical lenses can not be used to focus electron beams since electrons are different from visible light. In TEM instrumentation, an electromagnetic lens system is utilized to focus the electron beam onto sample grids. Figure 1.5.2.1 is an illustration of the lens system employed by TEM.

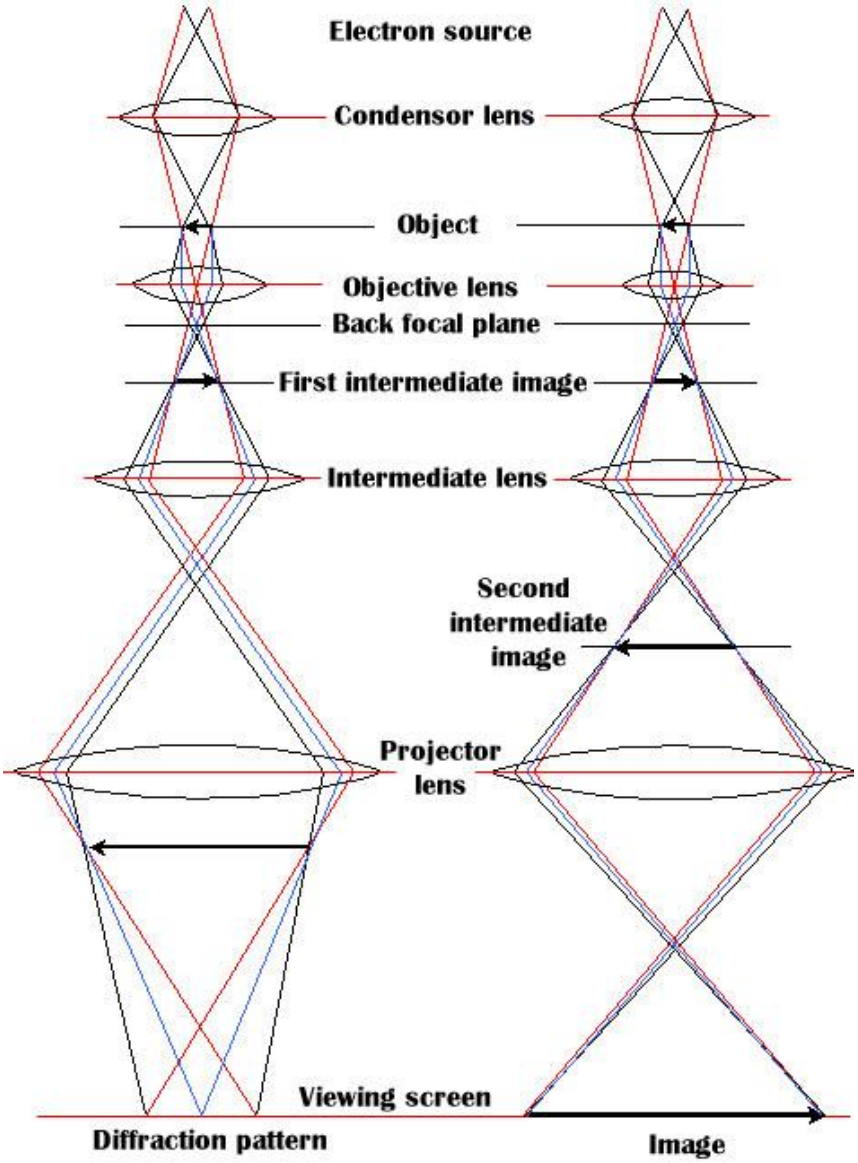

Figure 1.5.2.1 TEM lens system.

The electron beam generated by the TEM will interact differently with various materials due to differences in electron density of the sample as well as its chemical makeup. Images generated are based on those differences of electron beam/sample interactions.

A thin sample (~1μm) on a grid is required in order to obtain a useful image from TEM. It must also be able to withstand vacuum conditions since a TEM is utilized in a UHV environment. These sample grid requirements result in time consuming, sometimes difficult, sample preparations. Samples measured via TEM are also damaged due to the high energy of the electrons interacting with it and are often unrecoverable.

1.5.3 Superconducting Quantum Inference Device (SQUID)[115-122]

One of the most sensitive magnetometers, with a resolution up to 10^{-11}G, is the Superconducting Quantum Inference Device (SQUID) magnetometer. This extremely high sensitivity allows this instrument to be useful for the investigation of magnetic properties of nanoparticles over a wide range of temperatures and applied magnetic fields. The presence of a superconducting coil in SQUID magnetometers require the use of liquid helium in order to operate and to measure samples at low temperatures. All magnetic measurements presented in this thesis were performed on a Quantum Design MPMS-5S with a maximum magnetic field of 5 T.

SQUID magnetometers typically contain a superconducting ring with one to two Josephson junctions. The MPMS-5S contains two resistively-shunted junctions. A Josephson junction is constructed of a material whose electronic structure has the ability

to oscillate at high speeds when operated at extremely low temperatures, near 0 K. Figure 1.5.3.1 is a graphical schematic of a Josephson junction.

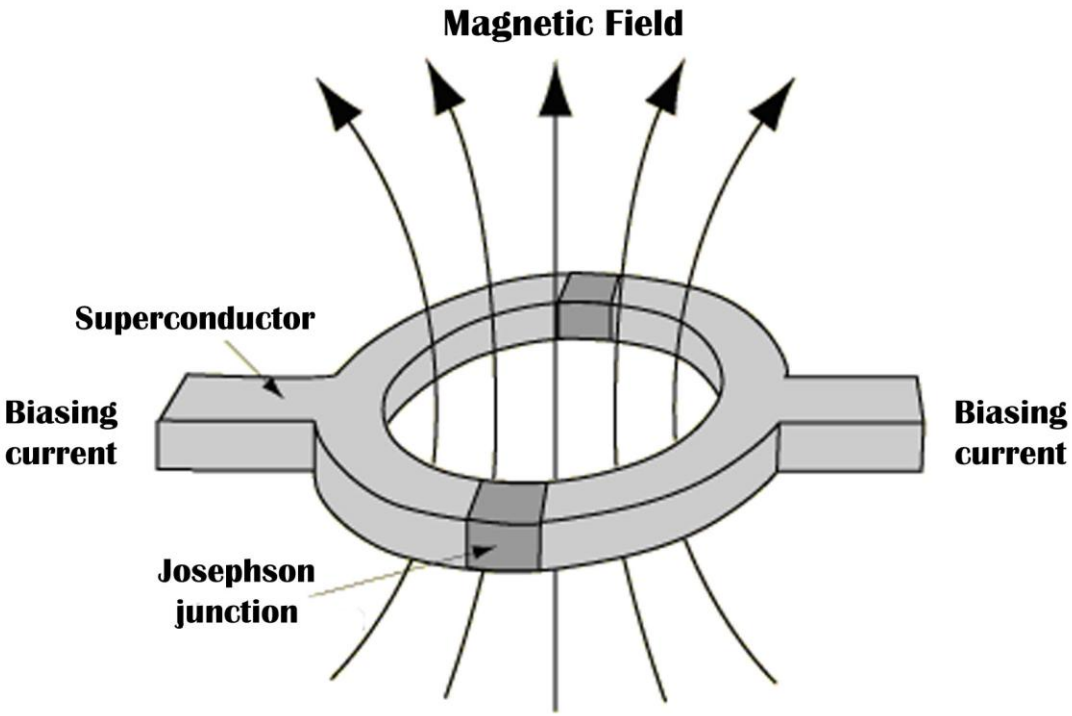

Figure 1.5.3.1: Josephson Junction.

It is composed of two superconductors that are separated by a thin piece of insulating barrier. The current that is generated when electrons pass through this barrier is known as Josephson current. When operated at near 0K, where thermal fluctuations are missing, Coulombic repulsion is overcome, and Cooper pairs of electrons form. A Cooper pair has a total spin of zero, due to spin cancellation, which results in the Pauli Exclusion Principle becoming no longer applicable and allowing the Cooper pair to settle to the same macroscopic quantum state as described by a wave function. Josephson

Effect is the current production across the Josephson junction. These junctions oscillate at high speeds when maintained at temperatures near 0K.

The magnetic moment of a sample is not measured directly; rather, the sample is moved through superconductive detecting coils that are connected to a sensor. In a SQUID magnetometer, the output voltage is proportional to the current flow within the detecting coils. When a sample is moved, its magnetic field induces a current within the detection coil. The fact that the detection coil, input coil, and all connecting wires form a superconductive loop, any magnetic flux changes cause a change in the constant current within the loop. The output voltage is therefore directly proportional to magnetic flux change generated via the sample's movement through the loop. Figure 1.5.3.2 shows a schematic diagram for the detection coil system in a MPMS-5S.

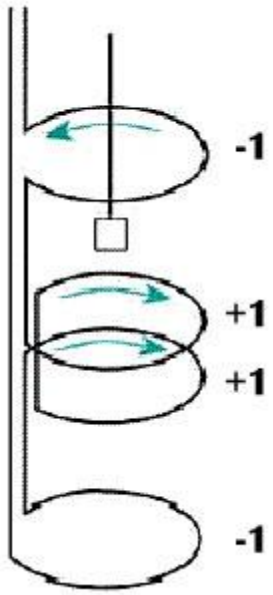

Figure 1.5.3.2: SQUID detection coil system.

This type of configuration is known as a second-order gradiometer. It consists of an upper coil turned, once, clockwise, a center coil turned, twice, counter-clockwise, and a bottom coil turned, once, clockwise. This coil configuration causes a reduction in noise as well background drift caused by the relaxation of magnetic fields of the superconducting magnet.

A typical sample preparation involves weighing out the powder and placing it into a gelatin capsule. If a hysteresis measurement is to be performed, the powder is immobilized in Icosane ($C_{20}H_{42}$) to prevent mechanical movement of the sample. The gel capsule is sealed with Kapton tape and inserted into a plastic sample straw. It is important that the materials used to contain the sample are nonmagnetic as to prevent complication in data interpretation. The sample straw is then sealed at one end using Kapton tape and the opposite end is attached to the sample rod, which is then inserted into the sample chamber. The sample chamber is under a vacuum in order to prevent atmospheric gases, O_2 and N_2, from freezing at low temperatures (< 90 K).

There are two main types of magnetic measurements made throughout this thesis. The first one measures the magnetic response of a material as a function of temperature (5-400 K) at a constant magnetic field (usually 100 G). The magnetic susceptibility is the magnetization (M) of a material divided by the applied magnetic field (H). For this thesis, it will be reported in units of emu/gG. The second measurement, performed most often in this work is a magnetic hysteresis measurement. This involves the measurement of a material's magnetic response as a function of an applied magnetic field at a constant temperature (usually 5 K or 300 K). The magnetic field strength is varied over a range of 0-5T. This type of measurement allows for the calculation of a sample's coercivity,

remnant magnetization, and saturation magnetization. Coercivity is measured in terms of field strength, *G*, while remnant and saturation magnetization are measured in emu/g.

Figure 1.5.3.3 shows the results from a magnetic susceptibility measurement. The peak of the curve is where the nanoparticle's blocking temperature occurs and where the system changes from ferrimagnetism to superparamagnetism.

These two types of magnetic measurements allow for the study and elucidation of magnetic origins and the effects of physical and chemical manipulation on magnetic nanoparticles.

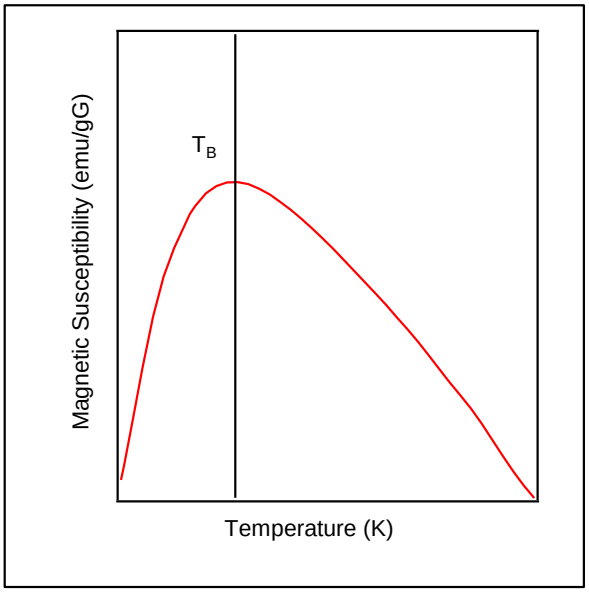

Figure 1.5.3.3: Typical temperature dependent magnetic measurement with T_B labeled.

1.5.4 Inductively Coupled Plasma Optical Emission Spectroscopy (ICP-OES)[108]

Inductively Coupled Plasma Optical Emission Spectroscopy (ICP-OES) is a technique used for the calculation of metal concentrations in a sample and has a resolution down to trace amounts(~μg/ml). A sample solution is placed in inductively coupled plasma, causing light to be emitted. When an atom or ion is excited, they

transmit characteristic wavelengths that are unique due to electron relaxation. The light measured via the ICP can then be correlated to those atoms.

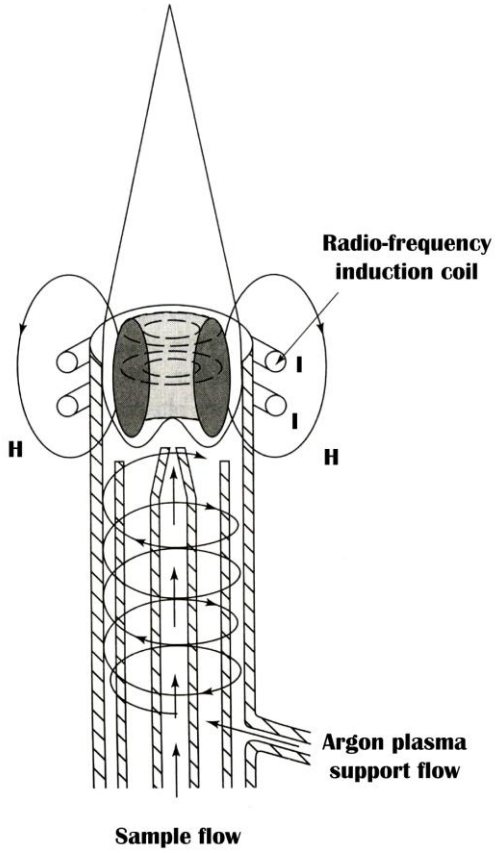

Figure 1.5.4.1 Detection system used in ICP-OES.

The relative intensity of each measured atom can then be used to quantify its concentration within the sample. These relative concentrations can then be used to calculate ratios of metal ions within the nanoparticles. This is useful to ensure that the proper amount of a dopant has been incorporated into a nanoparticle system or to provide additional proof of a nanoparticle's identity and chemical makeup. Contamination of the sample needs to be prevented since this method is so sensitive.

A standard sample preparation involves dissolving the nanoparticle powder in nitric acid under hydrothermal conditions (parabomb at 220^{o} C overnight). One milliliter of the solution is then added to nine milliliters of HPLC grade water. All ICP-OES analysis performed for were done on a Perkin Elmer Inductively Coupled Plasma Optical Emission Spectrometer (ICP), OPTIMA 7300DV, at Georgia Institute of Technology Chemical Analysis Lab, located in the IPST building.

References

(1) McCurrie, R. A. *Ferromagnetic Materials Structure and Properties*; Academic Press: New York, 1999.

(2) Jakubovics, J. P. *Magnetism and Magnetic Materials*; Institute of Metals: London, 1987.

(3) O'Handley, R. C. *Modern Magnetic Materials*; John Wiley&Sons, Inc.: New York, 2000.

(4) Morrish, A. H. *The Physical Principles of Magnetism*; John Wiley & Sons, Inc. : New York, 1965.

(5) Jiles, D. *Introduction to Magnetism and Magnetic Materials*; Chapman & Hall: London, 1990.

(6) Lafferty, P. *Magnets to Generators*; Gloucester Press: New York, 1989.

(7) Levine, S.; Johnstone, L. *The Magnet Book*; Sterling Publishing Company: New York, 1997.

(8) Cotton, F. A.; Wilkinson, G. *Advanced Inorganic Chemistry*; Wiley, 1966.

(9) Madsen, D. E.; Morup, S.; Hansen, M. F. *J. Magn. Magn. Mater.* **2006**, *305*, 95.

(10) Khodel, V. A.; Zverev, M. V.; Yakovenko, V. M. *Phys. Rev. Lett.* **2005**, *95*, 236402.

(11) Nelson, J. A.; Bennett, L. H.; Wagner, M. J. *J. Am. Chem. Soc.* **2002**, *124*, 2979.

(12) Rubin, P.; Sherman, A. *Phys. Lett. A* **2005**, *334*, 312.

(13) Williams, I. S.; R., S. *J. Phys. F* **1980**, *10*, 2551.

(14) Winterlik, J.; Fecher, G. H.; Felser, C.; C., M.; Jansen, M. *J. Am. Chem. Soc.* **2007**, *129*, 6990.

(15) Moruzzi, V. L.; Marcus, P. M. *Phys. Rev.* **1990**, *13*, 8361.

(16) Wohlfarth *Ferromagnetic Materials*; North-Holland, 1980.

(17) Griffiths, D. J. *Introduction to Electrodynamics*; Prentice Hall, 1998.

(18) Cussen, E. J.; Lynham, D. R.; Rogers, J. *Chem. Mater.* **2006**, *18*, 2855.

(19) Saltzman, W. R. *J. Phys. Chem.* **1989**, *93*, 7351.

(20) Kurath, D. *Phys. Rev. Lett.* **1959**, *3*, 431.

(21) Eshbach, J. R.; Strandberg, W. W. P. *Phys. Rev.* **1952**, *85*, 24.

(22) Schwinger, J. *Phys. Rev.* **1948**, *73*, 416.

(23) Bour, P.; Tam, C. N.; Keiderling, T. A. *J. Phys. Chem.* **1995**, *99*, 17810.

(24) Bloomfield, L. A. *How Things Work, The Physics of Everyday Life*; 2nd ed.; Wiley, 2001.

(25) Blackwood, O. H.; Kelly, W. C.; Bell, R. M. *General Physics*; 4th ed.; Wiley, 1973.

(26) Hysteresis; http://www.ndt-ed.org/EducationResources/CommunityCollege/MagParticle/Physics/HysteresisLoop.htm

(27) Osterloh, F. E.; Hiramatsu, H.; Dumas, R. K.; Liu, K. *Langmuir* **2005**, *21*, 9709.

(28) Leventis, N.; Gao, X. *Anal. Chem.* **2001**, *73*, 3981.

(29) Dhar, P.; Cao, Y.; Kline, T.; Pal, P.; Swayne, C.; Fischer, T. M.; Miller, B.; Mallouk, T. E.; Sen, A.; Johansen, T. H. *J. Phys. Chem. C* **2007**, *111*, 3607.

(30) Farrell, D.; Cheng, Y.; McCallum, R. W.; Sachan, M.; Majetich, S. A. *J. Phys. Chem. B* **2005**, *109*, 13409.

(31) Buchanan, K. S.; Zhu, X.; Meldrum, A.; Freeman, M. R. *Nano. Lett.* **2005**, *5*, 383.

(32) Legrand, J.; Petit, C.; Pileni, M. P. *J. Phys. Chem. B* **2001**, *105*, 5643.

(33) Park, S. J.; Kim, S.; Lee, S.; Kim, Z. G.; Char, K.; J., H. *J. Am. Chem. Soc.* **2000**, *122*, 8581.

(34) Tang, B.; Wang, G.; Zhuo, L.; Ge, J.; Cui, L. *Inorg. Chem.* **2006**, *45*, 5196.

(35) Liu, C.; Zou, B.; Rondinone, A. J.; Zhang, Z. J. *J. Am. Chem. Soc.* **2000**, *122*, 6263.

(36) Cullity, B. D.; Graham, C. D. *Introduction to Magnetic Materials*; Wiley & Sons: Hoboken, 2009.

(37) Dinega, D. P.; Bawendi, M. G. *Angew. Chem., Int. Ed.* **1999**, *38*, 1788.

(38) Knox, R. S. *J. Am. Chem. Soc.* **1965**, *87*, 3288.

(39) Kim, H.; Achermann, M.; Balet, L. P.; Hollingsworth, J. A.; Klimov, V. I. *J. Am. Chem. Soc.* **2005**, *127*, 544.

(40) Song, Q.; Zhang, Z. J. *J. Am. Chem. Soc.* **2004**, *126*, 6164.

(41) Leslie-Pelecky, D. L.; Rieke, R. D. *Chem. Mater.* **1996**, *8*, 1770.

(42) Lisiecki, I.; Albouy, P. A.; Pileni, M. P. *J. Phys. Chem. B* **2004**, *108*, 20050.

(43) Jun, Y. W.; Seo, J. W.; Cheon *J. Acc. Chem. Res.* **2008**, *41*, 179.

(44) Kang, Y. S.; Risbud, S.; Rablt, J. F.; Stroeve, P. *Chem. Mater.* **1996**, *8*, 2209.

(45) Xu, P.; Han, X.; Wang, M. *J. Phys. Chem. C* **2007**, *111*, 5866.

(46) Vestal, C. R.; Zhang, Z. J. *Chem. Mater.* **2002**, *14*, 3817.

(47) Rondinone, A. J.; Samia, A. C. S.; Zhang, Z. J. *J. Phys. Chem. B* **1999**, *103*, 6876.

(48) Stoner, E. C.; Wohlfarth, E. P. *Phil. Trans. R.S.L.* **1948**, *240*, 599.

(49) Neel, L. *Ann. Geophys.* **1949**, *5*, 99.

(50) Phan, N. T. S.; Gill, C. S.; Nguyen, J. V.; Zhang, Z. J.; Jones, C. W. *Angewandte Chemie International Edition* **2006**, *45*, 2209.

(51) Ramesh, K.; Chen, L.; Chen, F.; Liu, Y.; Wang, Z.; Han, Y.-F. *Catalysis Today* **2008**, *131*, 477.

(52) Li, Y.; He, D.; Cheng, Z.; Su, C.; Li, J.; Zhu, Q. *Journal of Molecular Catalysis A: Chemical* **2001**, *175*, 267.

(53) Ahmad, T.; Ramanujachary, K. V.; Lofland, S. E.; Ganguli, A. K. *Journal of Materials Chemistry* **2004**, *14*, 3406.

(54) Park, J.; Kang, E.; Bae, C. J.; Park, J.-G.; Noh, H.-J.; Kim, J.-Y.; Park, J.-H.; Park, H. M.; Hyeon, T. *The Journal of Physical Chemistry B* **2004**, *108*, 13594.

(55) Aichele, T.; Lorenz, A.; Hergt, R.; Görnert, P. *Crystal Research and Technology* **2003**, *38*, 575.

(56) Anderson, R. M.; Vestal, C. R.; Samia, A. C. S.; Zhang, Z. J. *Applied Physics Letters* **2004**, *84*, 3115.

(57) Tatarenko, A. S.; Srinivasan, G.; Bichurin, M. I. *Applied Physics Letters* **2006**, *88*, 183507.

(58) Ustinov, A. B.; Srinivasan, G.; Fetisov, Y. K. *Journal of Applied Physics* **2008**, *103*, 063901.

(59) Fu, Y.; Xiong, P.; Chen, H.; Sun, X.; Wang, X. *Industrial & Engineering Chemistry Research* **2011**, *51*, 725.

(60) Pardavi-Horvath, M. *J. Magn. Magn. Mater.* **2000**, *215-216*, 171.

(61) Harris, V. G.; Geiler, A.; Chen, Y.; Yoon, S. D.; Wu, M.; Yang, A.; Chen, Z.; He, P.; Parimi, P. V.; Zuo, X.; Patton, C. E.; Abe, M.; Acher, O.; Vittoria, C. *Journal of Magnetism and Magnetic Materials* **2009**, *321*, 2035.

(62) Vestal, C. R.; Zhang, Z. J. *J. Am. Chem. Soc.* **2003**, *125*, 9828.

(63) Greenough, R. D.; Jenner, A. G. I.; Schulze, M. P.; Wilkinson, A. J. *J. Magn. Magn. Mater.* **1991**, *101*, 75.

(64) Zhukov, A.; Cobeno, A. F.; Gonzalez, J.; Blanco, J. M.; Aragoneses, P.; Dominguez, L. *Sensors and Actuators A; Physical* **2000**, *81*, 129.

(65) Bhame, S. D. *J. App. Phys.* **2006**, *100*, 113911.

(66) McCallum, R. W.; Dennis, K. W.; Jiles, D. C.; Snyder, J. E.; Chen, Y. H. *Low Temp. Phys.* **2001**, *27*, 266.

(67) Kim, I.-B.; Han, M. H.; Phillips, R. L.; Samanta, B.; Rotello, V. M.; Zhang, Z. J.; Bunz, U. H. F. *Chemistry – A European Journal* **2009**, *15*, 449.

(68) Xia, C.; Ning, W.; Lin, G. *Sensors and Actuators B: Chemical* **2009**, *137*, 710.

(69) Yu, S.; Wu, Q.; Tabib-Azar, M.; Liu, C.-C. *Sensors and Actuators B: Chemical* **2002**, *85*, 212.

(70) Wang, G.; Meng, F.; Ding, C.; Chu, P. K.; Liu, X. *Acta Biomaterialia* **2010**, *6*, 990.

(71) Scarberry, K. E.; Dickerson, E. B.; McDonald, J. F.; Zhang, Z. J. *J. Am. Chem. Soc.* **2008**, *130*, 10258.

(72) Yim, Y. S.; Choi, J.-s.; Kim, G. T.; Kim, C. H.; Shin, T.-H.; Kim, D. G.; Cheon, J. *Chemical Communications* **2012**, *48*, 61.

(73) Datta, A.; Hooker, J. M.; Botta, M.; Francis, M. B.; Aime, S.; Raymond, K. N. *J. Am. Chem. Soc.* **2008**, *130*, 2546.

(74) Gerion, D.; Herberg, J.; Bok, R.; Gjersing, E.; Ramon, E.; Maxwell, R.; Kurhanewicz, J.; Budinger, T. F.; Gray, J. W.; Shuman, M. A.; Chen, F. F. *J. Phys. Chem. C* **2007**, *111*, 12542.

(75) Gorter, E. W. *Nature* **1950**, *165*, 798.

(76) Kronmuler, H. *Handbook of Magnetism and Advanced Magnetic Materials*; John Wiley & Sons, 2007; Vol. 5 book set.

(77) Smart, L. E.; Moore, E. A. *Solid State Chemistry*; 3rd ed.; Taylor & Francis Group: Boca Raton, 2005.

(78) Wadas, R. S. *Magnetism in Spinels Garnets and Perovskites*; Dom Slowa Polskiego: Poland, 1974.

(79) Rao, C. N. R.; Raveau, B. *Transition Metal Oxide: Structure, Properties, and Synthesis of Ceramic Oxides*; Wiley-VCH: New York, 1998.

(80) Chen, J.-C.; Hu, C.-C. *Journal of Crystal Growth* **2003**, *249*, 245.

(81) Shriver; Atkins In *Inorganic Chemistry*; W.H. Freeman and Company: New York, 1999; 3rd edition.

(82) Mathur, S.; Veith, M.; Rapalaviciute, R.; Shen, H.; Goya, G. F.; Martins Filho, W. L.; Berquo, T. S. *Chemistry of Materials* **2004**, *16*, 1906.

(83) Déchamps, M.; Djuriçić, B.; Pickering, S. *Journal of the American Ceramic Society* **1995**, *78*, 2873.

(84) Liu, C.; Zhang, Z. J. *Chem. Mater.* **2001**, *13*, 2092.

(85) Roca, A. G. *J. Phys. D: Appl. Phys.* **2009**, *42*, 224002.

(86) Teja, A. S.; Koh, P.-K. *Progress in Crystal Growth and Characterization of Materials* **2009**, *55*, 22.

(87) Zheng, L. *Advanced Materials Research* **2011**, *311-313*, 1294.

(88) Micelle; http://chemistry.tutorvista.com/biochemistry/micelle.html.

(89) Ghosh, M.; Biswas, K.; Sundaresan, A.; Rao, C. N. R. *Journal of Materials Chemistry* **2006**, *16*, 106.

(90) Schladt, T. D.; Graf, T.; Tremel, W. *Chemistry of Materials* **2009**, *21*, 3183.

(91) Song, Q.; Ding, Y.; Wang, Z. L.; Zhang, Z. J. *Chemistry of Materials* **2007**, *19*, 4633.

(92) Song, Q.; Zhang, Z. J. *J. Phys. Chem. B* **2006**, *110*, 11205.

(93) Sun, S.; Zeng, H. *J. Am. Chem. Soc.* **2002**, *124*, 8204.

(94) Cho, Y. S.; Burdick, V. L.; Amarakoon, V. R. W. *Journal of the American Ceramic Society* **1997**, *80*, 1605.

(95) Kanade, K. G.; Baeg, J. O.; Apte, S. K.; Prakash, T. L.; Kale, B. B. *Materials Research Bulletin* **2008**, *43*, 723.

(96) Sadhana, K.; Shinde, R. S.; Murthy, S. R. *International Journal of Modern Physics B: Condensed Matter Physics; Statistical Physics; Applied Physics* **2009**, *23*, 3637.

(97) Bokhimi, X.; Morales, A.; Novaro, O.; Portilla, M.; López, T.; Tzompantzi, F.; Gómez, R. *Journal of Solid State Chemistry* **1998**, *135*, 28.

(98) Cheng, F.; Shen, J.; Ji, W.; Tao, Z.; Chen, J. *ACS Applied Materials & Interfaces* **2009**, *1*, 460.

(99) Ghosh, N. N.; Pramanik, P. *Materials Science and Engineering: C* **2001**, *16*, 113.

(100) Kim, C. S.; Yi, Y. S.; Park, K. T.; Namgung, H.; Lee, J. G. *J. App. Phys.* **1999**, *85*, 5223.

(101) Thota, S.; Prasad, B.; Kumar, J. *Materials Science and Engineering: B* **2010**, *167*, 153.

(102) Zhang, Z.; Liu, S.; Chow, S.; Han, M. Y. *Langmuir* **2006**, *22*, 6335.

(103) Cullity, B. D. *Elements of X-Ray Diffraction*; 2nd ed.; Addison-Welsey, 1977.

(104) Ebsworth, E. A. V.; Rankin, D. W. H.; Cradock, S. *Structural Methods in Inorganic Chemistry*; 1st ed.; Blackwell Scientific: Oxford, 1987.

(105) Giacovazzo, C. *Fundmentals of Crystallography*; 2nd ed.; Oxford University: Oxford, 2002.

(106) Glusker, J. P.; Lewis, M.; Rosi, M. *Crystal Analysis for Chemists and Biologists*; Wiley, 1994.

(107) Percharsky, V. K. *Fundamentals of Powder Diffraction and Structural Characterization of Materials*; Kluwer Academica: Boston, 2003.

(108) Skoog, D.; Joller, F. J.; Nieman, T. A. *Principles of Instrumental Ananysis*; 5th ed.; Thomson Learning, Inc., 1998.

(109) Clarke, J. *Scientific American* **1994**, *271*, 46.

(110) Goldstein, J. I.; Newbury, D. E.; Echlin, P.; Joy, D. C.; Lifshin, E. *Scanning Electron Microscopy and X-Ray Microanalysis*, 1981.

(111) TEM; http://www.mete.metu.edu.tr/pages/tem/TEMtext/TEMtext.html.

(112) Wang, Z. L. *Elastic and Inelastic Scattering in Electron Diffraction and Imaging*; Plenum Press: New York, 1995.

(113) Wang, Z. L. *Adv. Mater.* **1998**, *10*, 13.

(114) Williams, D. B.; Carter, C. B. *Transmission Electron Microscopy*; Plenum Press: New York, 1996.

(115) Barone, A.; Paterno, G. *Physics and Applications of the Josephson Effect*; Wiley & Sons: New York, 1982.

(116) Gallop, J. C. *SQUIDs, The Joseohson Effects and Superconducting Electronics*; Adam Hilger: Bristol, 1991.

(117) Josephson, B. D. *Reviews of Modern Physics* **1974**, *46*, 251.

(118) McElfresh, M. *Fundamentals of Magnetism and Magnetic Measurments*; Quantum Design: San Diego, 1994.

(119) Rondinone, A. J.; Zhang, Z. J. *Handbook of Nanophase and Nanostructured Materials* **2003**, *2*, 252.

(120) Weinstock, H. *SQUID Sensors: Fundamentals, Fabrication and Aplications*; Kluwer Academic: Dordrecht, 1996.

(121) Josephson Junction http://hyperphysics.phy-astr.gsu.edu/hbase/solids/squid.html.

(122) Coil; http://ipc.iisc.ernet.in/~magsquid/contents.html.

Chapter 2:

$CoFe_2O_4$ and $MnFe_2O_4$ Nanoparticles Synthesized via the Aminolytic Method Using Various Carboxylate Precursors

2.1 Abstract:

Over the past decade, an inexpensive, simple, reusable, and environmentally friendly large scale synthesis method for the creation of spinel ferrite nanoparticles has been sought. The aminolytic method, a reaction between metal carboxylates and oleylamine in a non-coordinating solvent, fits the listed requirements. In this chapter, the effect of the chain length of the metal carboxylates on the synthesis of MFe_2O_4 (M = Co^{2+}, Mn^{2+} was explored. The carbon chain length was varied from a 2-carbon chain, acetate to a 9-carbon chain, nonanoate. The products were analyzed via XRD to ensure the pure phase (spinel ferrite) was obtained. The magnetic properties were measured using a SQUID magnetometer to verify that the desired magnetic properties were obtained. It was found that the reaction temperature needed for nanoparticle formation increased as the carboxylate chain length increased. The metal acetate required 240^{o}C while the metal nonanoate required 280^{o}C. The fact that the aminolytic method was able to produce the correct spinel ferrites using various metal carboxylate precursors adds to its versatility as a synthesis route for magnetic nanoparticles.

2.2 Introduction:

Spinel ferrite nanoparticles are of fundamental interest due to distinct physical properties that include size dependent blocking temperature, strong magnetic anisotropy, good chemical stability, and high coercivity. These nanoparticles have applications ranging from biomedicine, including MRI contrast agents[1] and drug delivery systems[2], to electronics, including high density data storage[3] and magneto-optic recording[4], separators[5], and sensors[6,7] (stress and gas) As a means for developing these technologies, there is a demand for a high yielding synthesis method that produces product of the same quality consistently and for as cheaply as possible must first be realized.

The spinel ferrite family is a useful tool for investigating the effects of chemical manipulations on magnetic properties, due to its well-defined crystal and magnetic structures. Spinel ferrites, with a general formula of AB_2O_4, contains two types of cation sites, A, tetrahedrally coordinated, and B, octahedrally coordinated[8]. The magnetic moments of the A sites align parallel to one another, while the B sites align parallel to each other. The tetrahedral and octahedral sites align antiparallel with each other and result in a partial cancellation of each other's magnetic moments, due to the magnitude of the magnetic moments of various metals[9]. This slight cancellation of the moments causes the system to exhibit ferrimagnetism (see Figure 2.1.1).

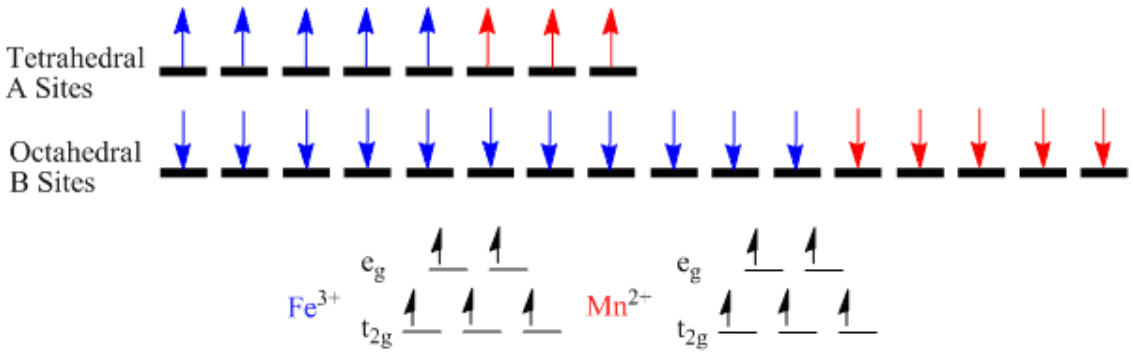

Figure 2.1.1: Alignment of magnetic moments in manganese ferrite.

There are three types of spinel ferrites depending on the site occupancy of the divalent and trivalent cations: normal, inverse, and mixed. When the divalent cation occupies A sites only and Fe(III) occupies the B sites, a normal spinel forms. An inverse spinel ferrite results when the divalent cation occupies half of the available B sites and the Fe(III) occupies the A sites and the remaining B sites. The final spinel ferrite type occurs when there is a random cation distribution of both A and B sites[8]. Most magnetic ferrites are inverse spinels, due to the Fe^{3+} being a d^5 ion with no crystal field stabilization energy, which will be the same if it occupies either a tetrahedral or octahedral site. The large M^{2+} ions will occupy B sites over A sites, while the smaller Fe^{3+} will occupy both A and B sites. $CoFe_2O_4$ is an inverse spinel ferrite while $MnFe_2O_4$ is a mixed ferrite[8].

Spinel ferrite nanoparticles exhibit superparamagnetism above its blocking temperature (T_B). Below this temperature, a "super-spin" results from the lack of magnetic domains and from ferrimagnetism[10].

Over the last few decades, extensive research into a high yielding synthesis of monodisperse spinel ferrite nanoparticles has been conducted. A desired trait of the

"perfect" synthesis method would be the ability to use various precursors and still obtain a wide range of target products from the same scheme. The various methods studied, to date, for the synthesis of spinel ferrite nanoparticles include the following: sol-gel[11,12], co-precipitation[13,14], mechanochemical[15,16], hydrothermal[17,18], and thermal decomposition[19,20]. Each method uses various techniques to control size, shape, and size distribution. They each have several drawbacks that complicate their ability to be scaled up to the industrial scale required for incorporation into the above-mentioned applications. In the sol-gel method, control can be exerted over morphology and particle size through the use of various gel and solvent systems but is hindered by the need for exact pH control and high (~600^{o}C) calcination temperatures. Some of the solvents and gel systems used in the sol-gel method require the use of either an inert atmosphere or protecting agent to prevent unwanted side reactions and impurities. The co-precipitation method, with the use of micelles, involves the oxidation of starting materials in a basic medium, often followed by a heat treatment at high temperatures. This method is useful for producing highly crystalline nanoparticles due to the high calcination temperature; however, this heat treatment step often results in low monodispersity due to agglomeration. It has been reported that the use of a hydrothermal treatment in place of the calcination step can alleviate the agglomeration problem, but results in poor crystallinity. The mechanochemical method, often called the "heat-and-beat" method, involves the grinding, or ball milling, of starting materials followed by high temperature heating to produce low monodisperse particles. One advantage of this technique is that it allows for the synthesis of large quantities of product, albeit of low quality. The thermal decomposition method, which utilizes the decomposition of one or more metal-organic

precursors to synthesize a desired product, often results in highly crystalline nanoparticles of tight size distributions. This is due to the matching of the decomposition temperature of the precursors and allows for a controlled bottom-up synthesis of nanoparticles. This method, however, is limited by the need for specific surfactants and solvents, can have impurities in the product, and often requires proper storage (inert atmosphere).

Herein we report the synthesis of $CoFe_2O_4$ and $MnFe_2O_4$ via the aminolytic method using various precursors. The aminolytic method is an improvement of the thermal decomposition method. In this synthesis technique, the nanoparticles are created in a two-step reaction: an amide bond forms between the acetate and an amine molecule. There is then a proton transfer that causes the formation of a metal hydroxide, which then undergoes a condensation reaction to form the metal oxide. It is the amide bond formation that governs the nanoparticles formation, and not the decomposition temperature of the precursor. The effect of the chain length of the metal carboxylate precursors on the synthesis of cobalt ferrite as well as manganese ferrites was explored. The carbon chain length was varied from a 2-carbon chain, acetate to a 9-carbon chain, nonanoate. $CoFe_2O_4$ was chosen to ensure that the aminolytic method would be able to handle the precursor change and still be able to produce the target product. $MnFe_2O_4$, on the other hand, was chosen to see if the precursor change would be able to produce nanoparticles that are more sensitive to reaction conditions. $MnFe_2O_4$ is the least thermally stable of the spinel ferrite family and often decomposes to metal oxides of Mn_2O_3 and Fe_2O_3 upon heat treatment in ambient atmosphere[21].

2.3 Experimental:

2.3.1 Precursor:

The metal acetate precursor was prepared by reacting metal hydroxide with either nonanoic acid, to make metal nonanoate, or valeric acid, to make metal valerate.

MnFe precursors were produced by dissolving $MnCl_2 \cdot 4H_2O$ (10 mmol) and $FeCl_3 \cdot 6H_2O$ (20 mmol) in 100 mL distilled water and stirred for 30 minutes under ambient conditions. Upon the addition of 100 mL of 1 M NaOH solution, a brown metal hydroxide precipitate formed. The mixture was stirred for another hour and then the precipitate was collected via centrifugation. The solid was washed several times with distilled water. The MnFe-hydroxide was dissolved with 50 mL of either nonanoic acid or valeric acid, depending on desired precursor. The mixture was heated at 100^oC overnight. Upon complete evaporation of the liquid, a fine powder was collected.

CoFe precursors were produced by dissolving $CoCl_2 \cdot 4H_2O$ (10 mmol) and $FeCl_3 \cdot 6H_2O$ (20 mmol) in 100 mL distilled water and stirred for 30 minutes. Upon the addition of 100 mL of 1M NaOH solution, a brown metal hydroxide precipitate formed. The mixture was stirred for another hour and then collected via centrifugation. The solid was washed several times with distilled water. The CoFe-hydroxide was dissolved with 50mL of either nonanoic acid or valeric acid, depending on desired precursor. The mixture was heated at 90^oC overnight. Upon complete evaporation of the liquid, a fine powder was collected.

2.3.2 Synthesis of $CoFe_2O_4$ and $MnFe_2O_4$ Nanoparticles

$MnFe_2O_4$ and $CoFe_2O_4$ nanoparticles were synthesized via the aminolytic reaction. 1.5 g metal valerate, or nonanoate precursor, was dissolved in a mixture of 10mL of oleylamine and 40mL of dibenzyl ether at 140^{o}C for an hour under an Ar atmosphere. The metal precursor solution was agitated at 140^{o}C an hour. The temperature was raised to 270^{o}C at a ramping rate of 5^o C/min, and the reaction solution was agitated for another hour. Upon cooling to room temperature, the nanoparticles were collected with a magnetic field and washed three times using absolute ethanol.

2.3.3 Instrumentation:

X-ray diffraction (XRD) patterns were collected with a Panalytical X'pert Pro X-Ray Diffractometer with a copper Kα source over a 15º – 85º 2θ range. Particle size was determined from the average peak broadening of the five strongest Bragg peaks using the commercial program IGOR and the Debye-Scherrer equation. Magnetic measurements were performed using a Quantum Design MPMS-5S SQUID magnetometer. Particles were immobilized in icosane ($C_{20}H_{42}$, Aldrich) for hysteresis measurements. . Inductively Coupled Plasma Atomic Emission Spectroscopy (ICP-AES) samples were prepared by digesting ~ 5 mg nanoparticles in 10 mL nitric acid overnight in parabomb at 210 ˚C. A 1 mL aliquot was diluted to 10 mL with HPLC grade water. Samples were submitted to Chemical Analysis lab at Georgia Institute of Technology for elemental analysis on a Perkin Elmer Inductively Coupled Plasma Optical Emission Spectrometer (ICP), OPTIMA 7300DV.

2.4 Results/Discussion:

The X-ray diffraction patterns shown in Figure 2.4.1 indicate phase pure $CoFe_2O_4$ nanoparticles were produced via the aminolytic method using oleylamine, dibenzyl ether, and CoFe-carbonate precursors of various carbon chain lengths. The patterns show excellent crystallinity for all $CoFe_2O_4$ nanoparticles synthesized. The relative peak intensity and position of the diffraction patterns match that of the standard pattern (22-1086) and is indicated in Figure 2.4.1.

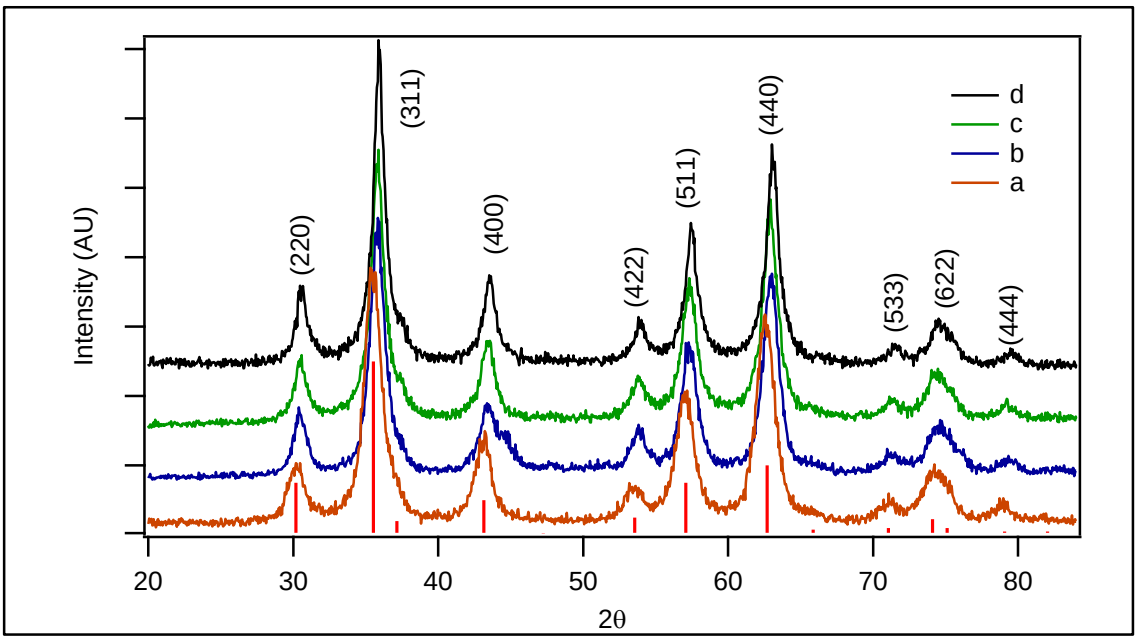

Figure 2.4.1: $CoFe_2O_4$ nanoparticles produced using (a) acetate (10.2 nm), (b) propionate (8.6 nm), (c) valerate (12 nm), and (d) nonanoate precursors (9 nm).

Cobalt ferrite produced using various carbon chain length precursors was chosen due to its high stability and ease of production via normal aminolytic method conditions. I wanted to make sure that the pure phase product could be synthesized despite using

different precursors, then move to a more challenging product to fully test the versatility of the aminolytic method. Table 2.4.1 shows Inductively Coupled Plasma Atomic Emission Spectroscopy (ICP-AES) results for the cobalt ferrite produced and indicates that the Fe^{3+} to Co^{2+} ratio is the desired 2:1.

Table 2.4.1: ICP-AES of $CoFe_2O_4$.

	Acetate	Propionate	Valerate	Nonanoate
Theoretical	2	2	2	2
Actual	1.98	2.1	2.06	2.11

This indicates that the proper spinel ferrite nanoparticles were produced despite changing the chain length of the precursor. An interesting side note is that, in order to produce the nanoparticles using the CoFe-valerate precursor, a higher reaction temperature was required. This trend continues as the chain length of the precursor increases. For the propionate precursor, a reaction temperature of 250^{o}C was essential while the valerate precursor required 260^{o}C and 270^{o}C for the nonanoate precursor. This is due to the longer chain lengths of the precursors possessing a higher diffusion energy requirement for the amine to come in contact with the carbonate end of the chain and therefore react to form the desired amide bond.

Table 2.4.2 Minimum temperature required for proper phase/composition formation.

	Acetate	Propionate	Valerate	Nonanoate
Temperature	~240^{o}C	~250^{o}C	~260^{o}C	~270^{o}C

Once the product was identified to be of the correct phase and composition, magnetic studies were performed. The first was a temperature dependent study where the magnetic susceptibility of the nanoparticles was monitored under a constant magnetic field of 100G. Figure 2.4.2 shows the results. Clearly, a blocking temperature for each cobalt ferrite nanoparticle system produced via the above-methods can be seen and is indicated in the figure.

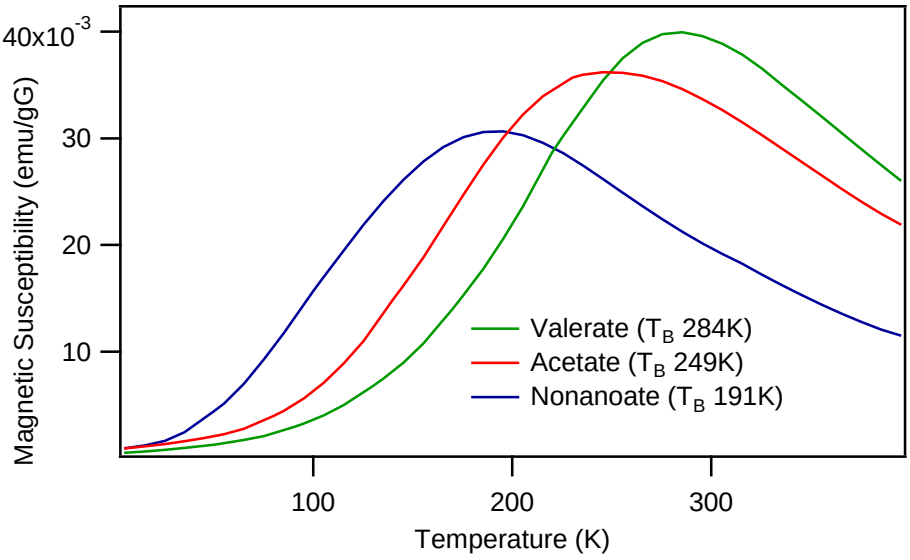

Figure 2.4.2: Temperature dependent magnetization of $CoFe_2O_4$ nanoparticles from acetate, valerate, and nonanoate precursors. See Figure 2.4.1 for sizes.

The reason for the different blocking temperatures despite the same composition is due to the energy barrier (E_A) for rotation of magnetization orientation in a single domain particle. This energy has best been described by the Stoner-Wohlfarth theory[22]:

$$E_A = KV\sin^2\theta \qquad (2.4.1.1)$$

K is the anisotropy of the system under investigation, *V* is the volume of the nanoparticle, and θ is the angle between an applied magnetic field and the nanoparticle's easy axis. The blocking temperature of a nanoparticle is the temperature at which the moments of the nanoparticle are no longer blocked and thus are able to overcome E_A[23]. As expected, the blocking temperature increases with increasing nanoparticle size. The size of the $CoFe_2O_4$ particles produced using valerate, acetate and nonanoate precursors were calculated to be 12.0nm, 10.2nm 9.0nm respectively.

The second magnetic study performed was a field dependent magnetic study, in which the $CoFe_2O_4$ nanoparticle's magnetic moment is monitored as a function of applied magnetic field at a constant temperature (5K). The results of the expected hysteresis curves can be seen in Figure 2.4.3.

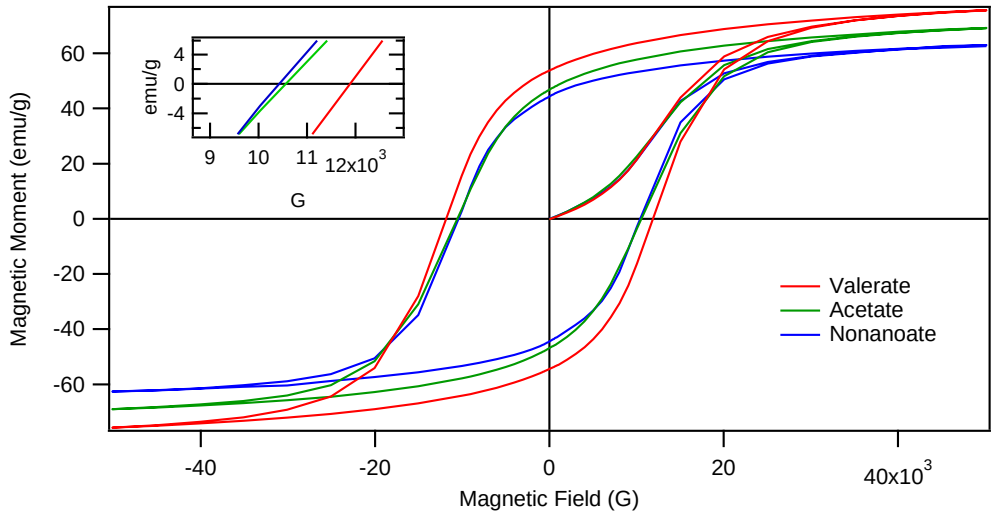

Figure 2.4.3: Hysteresis curves of $CoFe_2O_4$ nanoparticles from valerate, and nonanoate precursors. Inset shows expanded x-axis for viewing of crossover. See Figure 2.4.1 for sizes.

The expected trends for the remnant magnetization and saturation magnetization are observed. Saturation magnetization represents the highest amount of magnetic moments alignment with an applied magnetic field. It makes sense that this value would increase with an increase in nanoparticle size (volume) due to the higher number of magnetic moments present. Remnant magnetization, on the other had, represents the magnetization retained by the nanoparticle once the applied magnetic field is removed and is expected to have the same trend as the saturation magnetization. This is, again, due to the higher number of magnetic moments present in the larger nanoparticles and thus has a higher capacity to retain more of the applied field. The coercivity of uniaxial single roaming nanoparticles is derived from the Stoner-Wohlfarth theory[22]:

$$H_C = \frac{2K}{\mu_o M_S} \qquad (2.4.1.2)$$

μ_o is the permeability of vacuum and M_s is the saturation magnetization. Since the magnetic anisotropy is directly proportional to activation energy as well as coercivity, the hysteresis loop is expected to widen with increasing particle volume. This trend can be seen in Figure 2.4.3. The blocking temperatures, coercivity, remnant magnetization, and saturation magnetization all correspond to literature values, further indication that changing the precursor chain length still allows for the production of $CoFe_2O_4$ nanoparticles.

Table 2.4.3: Compiled magnetic data for $CoFe_2O_4$ nanoparticles from acetate, valerate, and nonanoate precursors.

	H_C (G)	M_R (emu/g)	M_S (emu/g)
Valerate	11,888	53.73	75.69
Acetate	10,563	46.78	69.18
Nonanoate	10,403	43.60	62.30

The next step was then to further test the versatility of the aminolytic method and its ability to accommodate varying precursor carboxylate chain lengths. $MnFe_2O_4$ nanoparticles were chosen for this purpose because it is the least thermally stable and will often decompose to Mn_2O_3 and Fe_2O_3, upon heat treatment under ambient conditions[21]. It also has the ability to produce MnO side products in other synthesis methods. It should be noted that no special considerations or conditions were imposed on the aminolytic reaction when $MnFe_2O_4$ was synthesized. Figure 2.4.4 shows the XRD patterns of the nanoparticles produced using MnFe precursors of various chain lengths, oleylamine, and dibenzyl ether. The absence of impurity peaks indicates that the particles produced are highly pure and phase stable. The peak position and relative intensity matches that of the standard pattern (ICDD File 10-319) and is indicated in Figure 2.4.4.

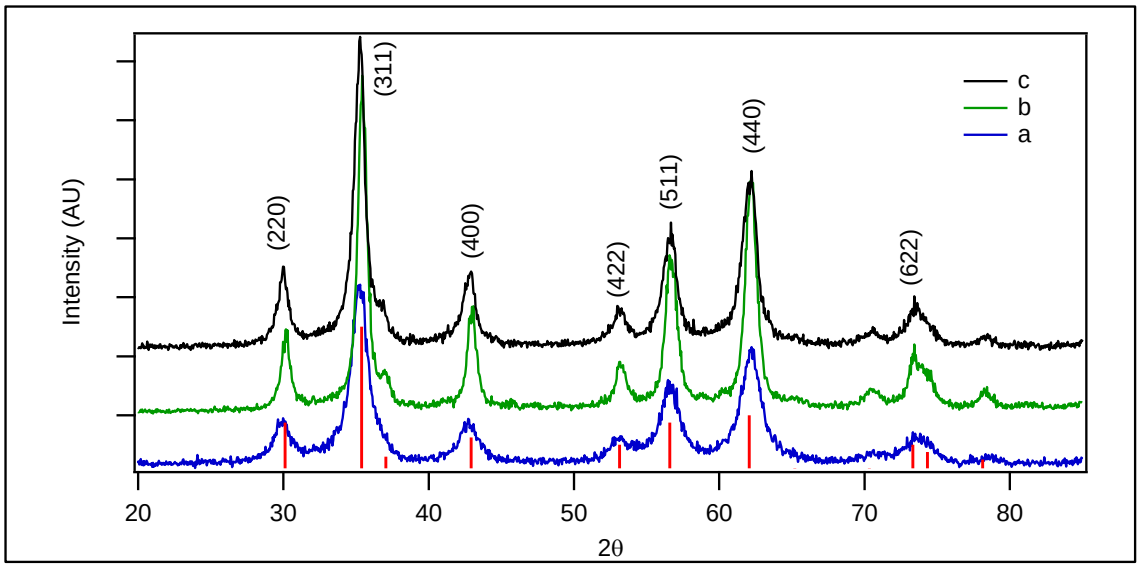

Figure 2.4.4: $MnFe_2O_4$ nanoparticles produced using (a) acetate (6.7nm), (b) valerate (5.2nm), and (c) nonanoate precursors(8.1nm).

Table 2.4.2 shows the ICP-AES results for the manganese ferrites produced and indicates that the Fe^{3+} to Mn^{2+} ratio is the desired 2:1.

Table 2.4.2: ICP-AES of $MnFe_2O_4$.

	Acetate	Valerate	Nonanoate
Theoretical	2	2	2
Actual	2.05	1.91	1.96

This further shows that the desired ferrite nanoparticles were produced despite changing the chain length of the precursor. The same reaction temperature requirements mentioned above are present in this system. The valerate precursor required 265^{o}C and 275^{o}C for the nonanoate precursor. This again is due to the longer chain lengths of the precursors possessing a higher diffusion energy requirement for the amine to come in

contact with the carboxylate end of the chain and therefore react to form the desired amide bond.

Magnetic studies were also performed on the $MnFe_2O_4$ nanoparticles. The first was the temperature dependent study and the results can be viewed in Figure 2.4.5.

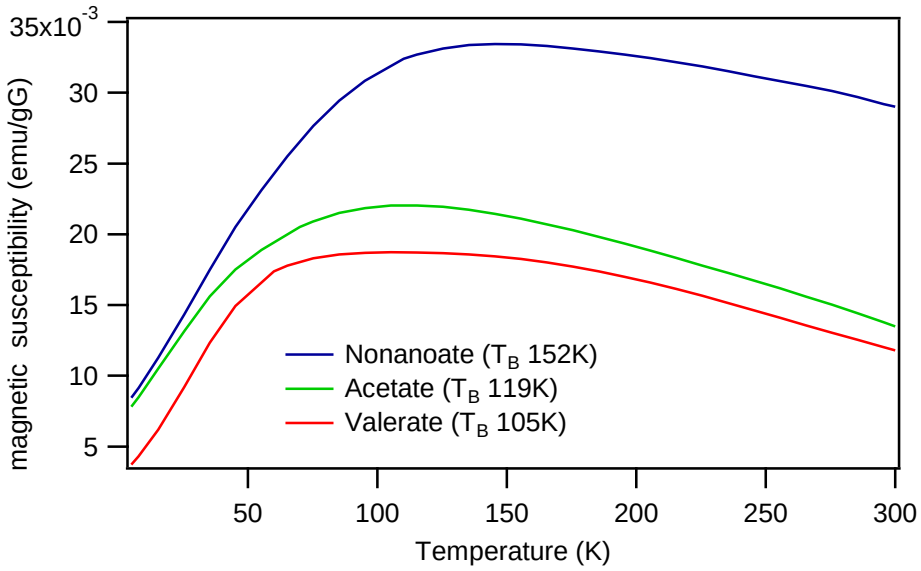

Figure 2.4.5: Temperature dependent magnetization of $MnFe_2O_4$ nanoparticles from acetate, valerate, and nonanoate precursors. See 2.4.4 for sizes.

The blocking temperatures for nanoparticles produced with the various precursors are indicated in the figure. Again, the reason for the different blocking temperatures for the different systems is due to the different sizes of nanoparticles produced. This goes back the Stoner-Wohlfarth theory, where E_a is proportional to nanoparticle volume. The sizes of the particles produced via nonanoate, acetate, and valerate precursors were calculated via peak broadening in the XRD pattern and were found to be 8.1nm, 6.7nm, and 5.2nm, respectively.

The second magnetic study that was performed was the field dependent study, and the results can be seen in Figure 2.4.6. The expected trends in coercivity, remnant magnetization, and saturation magnetization can be seen in the figure. These trends are due to difference in nanoparticle size between the different systems. The system that has the larger average nanoparticle size will have the larger coercivity, M_r and M_s values, which is seen in Figure 2.4.6.

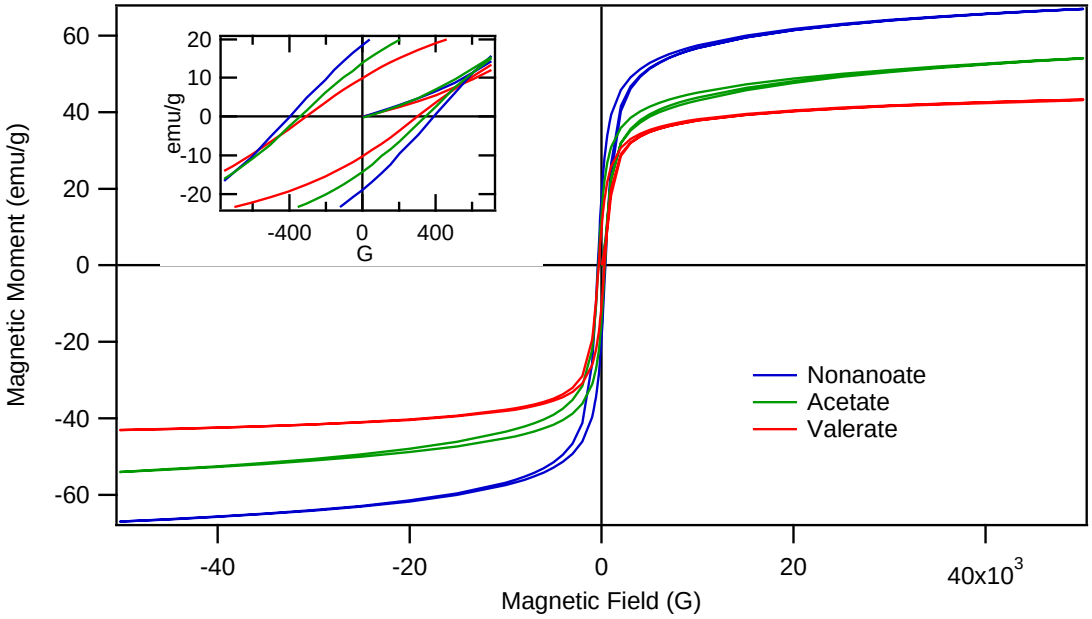

Figure 2.4.6: Hysteresis curves of $MnFe_2O_4$ nanoparticles from acetate, valerate, and nonanoate precursors. Inset is expanded view of origin. See 2.4.4 for sizes.

Table 2.4.5: Compiled magnetic data for $MnFe_2O_4$ nanoparticles from acetate, valerate, and nonanoate precursors.

	H_C (G)	M_R (emu/g)	M_S (emu/g)
Nonanoate	390	18.38	66.94
Acetate	344	13.82	54.06
Valerate	300	9.84	43.29

.

2.5 Conclusion:

Synthesis of $CoFe_2O_4$ and $MnFe_2O_4$ via the aminolyic method using CoFe and MnFe precursors with various chain lengths was demostrated. The particles produced were tested via XRD and ICP-AES to verify that the desired phase and composition were obtained. The absence of impurity peaks in the XRD and the correct ratios of Fe-to-Co and Fe-to-Mn signal this. Temperature dependent and field dependent magnetic studies were performed. These measurements of the nanoparticles depended on volume as well as the divalent cation in the ferrite system. These measurements were in excellent agreement with theory and literature values[19]. This chapter shows that the aminolytic method is quite versitile in its ability to produce high quality nanoparticles despite the use of various precursors while reducing the amount of waste byproduct and is able to produce the reaction-sensitive manganese ferrite despite the various MnFe precursors.

2.6 References:

(1) Kim, D.-H.; Zeng, H.; Ng, T. C.; Brazel, C. S. *Journal of Magnetism and Magnetic Materials* **2009**, *321*, 3899.

(2) Scarberry, K. E.; Dickerson, E. B.; McDonald, J. F.; Zhang, Z. J. *Journal of the American Chemical Society* **2008**, *130*, 10258.

(3) Gao, X.; Liu, L.; Birajdar, B.; Ziese, M.; Lee, W.; Alexe, M.; Hesse, D. *Advanced Functional Materials* **2009**, *19*, 3450.

(4) Xia, G. *Nanotechnology* **2010**, *21*.

(5) Li, C.-J.; Wang, J.-N.; Wang, B.; Gong, J. R.; Lin, Z. *Materials Research Bulletin* **2012**, *47*, 333.

(6) Devi, P. I.; Rajkumar, N.; Renganathan, B.; Sastikumar, D.; Ramachandran, K. *Sensors Journal, IEEE* **2011**, *11*, 1395.

(7) Gadkari, A. B.; Shinde, T. J.; Vasambekar, P. N. *Sensors Journal, IEEE* **2011**, *11*, 849.

(8) McCurrie, R. A. *Ferromagnetic Materials Structure and Properties*; Academic Press: New York, 1999.

(9) Jiles, D. *Introduction to Magnetism and Magnetic Materials*; Chapman&Hall: London, 1990.

(10) Gorter, E. W. *Nature* **1950**, *165*, 798.

(11) Shi, M.; Zuo, R.; Xu, Y.; Jiang, Y.; Yu, G.; Su, H.; Zhong, J. *Journal of Alloys and Compounds* **2012**, *512*, 165.

(12) Wang, Z.; Fei, W.; Qian, H.; Jin, M.; Shen, H.; Jin, M.; Xu, J.; Zhang, W.; Bai, Q. *Journal of Sol-Gel Science and Technology* **2012**, *61*, 289.

(13) Jian, G.; Fu, Q.; Zhou, D. *Journal of Magnetism and Magnetic Materials* **2012**, *324*, 671.

(14) Vestal, C. R.; Zhang, Z. J. *Journal of Solid State Chemistry* **2003**, *175*, 59.

(15) Manova, E.; Paneva, D.; Kunev, B.; Estournès, C.; Rivière, E.; Tenchev, K.; Léaustic, A.; Mitov, I. *Journal of Alloys and Compounds* **2009**, *485*, 356.

(16) Shi, Y.; Ding, J.; Yin, H. *Journal of Alloys and Compounds* **2000**, *308*, 290.

(17) Baruwati, B.; Nadagouda, M. N.; Varma, R. S. *The Journal of Physical Chemistry C* **2008**, *112*, 18399.

(18) Hou, X.; Feng, J.; Xu, X.; Zhang, M. *Journal of Alloys and Compounds* **2010**, *491*, 258.

(19) Bao, N.; Shen, L.; Wang, Y.; Padhan, P.; Gupta, A. *Journal of the American Chemical Society* **2007**, *129*, 12374.

(20) Jia, Z.; Ren, D.; Zhu, R. *Materials Letters* **2012**, *66*, 128.

(21) Tailhades, P.; Rousset, A.; Bendaoud, R.; Fert, A. R.; Gillot, B. *Materials Chemistry and Physics* **1987**, *17* 521.

(22) Wohlfarth *Ferromagnetic Materials*; North-Holland, 1980.

(23) Leslie-Pelecky *Chem. Mater.* **1996**, *8*.

Chapter 3

The Effect of Cu Substitution on the Magnetic Properties of Manganese Ferrite Nanoparticles

3.1 Abstract:

Magnetic nanoparticles are being increasingly incorporated into biomedicines and drug delivery systems. The magnetic properties of spinel ferrite materials are particularly useful in directing medicine linked to the nanoparticles due to their strong magnetic response and chemical robustness. Quantum couplings of magnetic ions in the spinel ferrite system govern their magnetic properties and responses. An understanding of the couplings between these metal ions allows for tailoring of magnetic properties to obtain the desired response needed for various applications. Copper doping in the manganese ferrite systems allows for the investigation of the effects of orbital Jahn-Teller distortion as well as orbital angular momentum on the effect of magnetic properties. To fully investigate these quantum coupling effects, a series $Cu_xMn_{1-x}Fe_2O_4$ nanoparticles, where *x* ranges from 0.0 to 0.2, was synthesized via the aminolytic reaction. The Cu^{2+} ion will occupy the tetrahedral (A) sites in spinel ferrites or the octahedral (B) sites, depending on the synthesis used. In lower temperature synthesis techniques, such as the aminolytic method, the copper will initially occupy the A sites, which results in an increase in net magnetization of the system. As the concentration Cu^{2+} is increased, it will start to occupy the B sites and will cause an overall decrease in magnetic response, which

explains the drop in coercivity, remnant magnetization, and saturation magnetization when the Cu^{2+} concentration reaches 10%.

3.2 Introduction:

Research into nanometer-sized magnetic systems has been drawing attention because of a wide range of applications in data storage[1,2], sensors[3,4], ferrofluids[5], separation technologies[6,7], and biomedicine[8,9]. Control over fundamental magnetic properties, such as remnant magnetization and coercivity, requires a better understanding of the origins of magnetism and the effects that orbital angular momentum, quantum couplings, and the Jahn-Teller effect. Studying the magnetic properties of $Cu_xMn_{1-x}Fe_2O_4$ is a methodical way to study these effects on magnetism.

The spinel ferrite system has a well-defined crystal and magnetic structure and is useful for studying the effects of chemical manipulations on magnetic properties. Spinel ferrites, usually denoted as AB_2O_4, contain two cation sites, A, having a tetrahedral coordination, and B, having an octahedral coordination, bridged by oxygen, which coordinates to the central metal cations[10]. The magnetic moments of the tetrahedral sites align parallel with respect to each other, while the octahedral site ions align parallel to one another. The moments in the tetrahedral and octahedral sites align antiparallel with each other and result in a partial cancellation of each other's magnetic moments, due to the magnitude of the magnetic moments of various magnetic cations, which causes the system to exhibit ferrimagnetism (see Figure 3.2.1). Spinel ferrite nanoparticles show superparamagnetism above its blocking temperature (T_B) while below this temperature

there is antiferromagnetic ordering due to the net magnetic moments pointing along the easy axis.

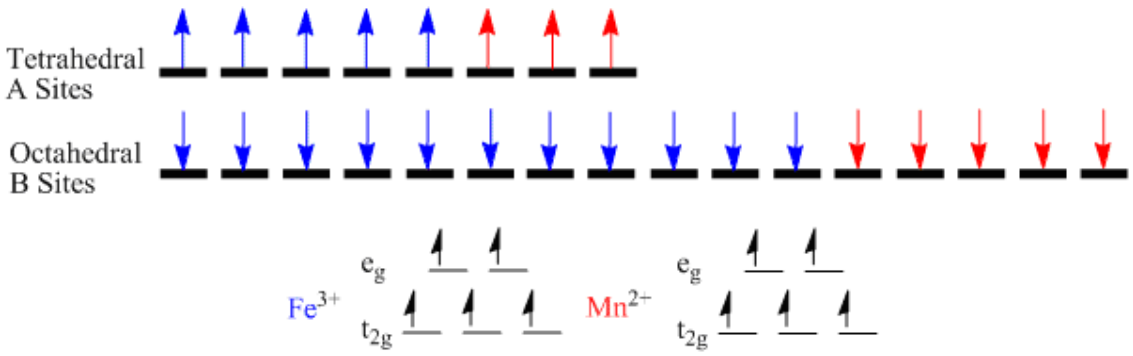

Figure 3.2.1 Unequal antiparallel alignment of magnetic moments in manganese ferrite.

The manganese ferrite system is a mixed spinel where the Mn^{2+} ion randomly occupies both the tetrahedral and octahedral sites[11]. The copper ferrite system, on the other hand, can form either a normal or inverse spinel, depending on the reaction conditions[12]. When the copper ferrite is an inverse spinel, Fe^{2+} randomly occupies the A and B sites, while the copper occupies the B sites only. This results in a slight tetragonal distortion due to Jahn-Teller effects. In the normal spinel, the iron occupies A and B sites again, while the Cu^{2+} will fill the A sites, where its Jahn-Teller distortion is diminished[13].

Nanoparticles of the $Cu_xMn_{1-x}Fe_2O_4$ system allows for the study of the role of the Jahn-Teller distortion ferrites Cu^{2+} ion doping. Depending on the synthesis method, the Cu^{2+} will either occupy the A or B site. When the copper ion occupies the B site, the net magnetic moment of the nanoparticles is expected to decrease. This is because the Mn^{2+}, which has an electron configuration of $t_{2g}^3e_g^2$ ($5\mu_B$), is being replaced with Cu^{2+}, which has a configuration of $t_{2g}^6e_g^3$ ($1\mu_B$). When the copper occupies the A sites, it is replacing manganese and will result in an increase in overall net magnetic moments in the system

due to the reduction in the cancellation between A and B sites. When Cu^{2+} occupies tetrahedral sites, the magnetic anisotropy of the nanoparticle is also expected to increase. While in the tetrahedral site, Mn^{2+} shows no orbital angular momentum, Cu^{2+} does. This system is fundamentally interesting to see how the randomness of the Mn^{2+} occupancy will affect where the copper ions will dope and the overall effect on the magnetic properties of the system.

Spinel ferrite nanoparticles have been synthesized through a variety of methods, including mechanochemical[14,15], sol-gel[16,17], co-precipitation[18,19], hydrothermal[20,21], and thermal decomposition[22,23]. Each method has its merits and drawbacks. For example, the mechanochemical method, which involves the grinding and high temperature heating of starting materials, produces polydispersed particle systems but allows for the creation of large quantities of product. The sol-gel method of hydrolysis and condensation reactions of precursors results in controlled size and morphology. It, however, suffers from the need for protecting agents as well as long reaction times. The co-precipitation method, which can utilize micelles, involves the oxidation of metal starting materials in a basic medium followed by heat treatment, oftentimes above 500^{o}C. This method is useful for producing highly crystalline nanoparticles but, because of the need for the heat treatment step it often results in low monodispersity. The calcination step in the co-precipitation method can be replaced with hydrothermal treatment to help lessen the agglomeration problem but results in low crystallinity. Commonly, highly crystalline and monodispersed nanoparticles are produced via a thermal decomposition method with metal organic precursors; however, there is a need to tailor the precursors to contain decomposition temperatures that are similar in order to form nanoparticles of the desired composition.

Herein, we report a fast, simple, cheap, one-pot synthesis technique for the production of $Cu_xMn_{1-x}Fe_2O_4$ nanocrystals using inexpensive metal chlorides and sodium propanoate in a moderately hot oleylamine solvent. The magnetic properties as a function of Cu substitution have also been characterized.

3.3 Experimental:

The *In-Situ* aminolytic method was used to synthesize a series of nanoparticles of $Cu_xMn_{1-x}Fe_2O_4$, where x = 0.0, 0.05, 0.08, 0.1, 0.16 and 0.20. $MnCl_2 \bullet 4H_2O$ (Alfa Aesar, ACS grade), 1-x mmol, $FeCl_3$ (Alfa Aesar 98%), 2 mmol, $CuCl_2 \bullet 2H_2O$ (Alfa Aesar, ACS grade), x mmol, and sodium propionate, CH_3CH_2COONa, 5 mmol (TCI, Reagent Grade), were dissolved in 50 mL of oleylamine (TCI, ACS grade) and stirred for one hour at 140^{o}C while purged with Ar. Then the temperature was raised to 240^{o}C at a ramping rate of 5^{o}C/min and the reaction solution was agitated for another hour. The nanoparticles were cooled to room temperature, separated with a strong magnet, and washed several times using absolute ethanol followed by DI water. The resulting solid was allowed to dry at room temperature overnight.

3.3.1 Instrumentation:

X-ray diffraction (XRD) patterns were collected with a Panalytical X'pert Pro X-Ray Diffractometer with a copper Kα source over a 15º – 85º 2θ range. Particle size was determined from the average peak broadening of the five strongest Bragg peaks using the commercial program IGOR and the Debye-Scherrer equation. Magnetic measurements were performed using a Quantum Design MPMS-5S SQUID magnetometer. Particles

were immobilized in icosane ($C_{20}H_{42}$, Aldrich) for hysteresis measurements. Inductively Coupled Plasma Atomic Emission Spectroscopy (ICP-OES) samples were prepared by digesting ~5 mg nanoparticles in 10mL nitric acid overnight in a parabomb at 210^{o}C. A 1 mL aliquot was diluted to 10 mL with HPLC grade water. Samples were submitted to the Chemical Analysis Lab at Georgia Institute of Technology for elemental analysis on a Perkin Elmer Inductively Coupled Plasma Optical Emission Spectrometer (ICP), OPTIMA 7300DV.

3.4 Data/Discussion:

The XRD pattern shown in Figure 3.4.1 indicates that a pure spinel phase $Cu_xMn_{1-x}Fe_2O_4$ nanoparticles was synthesized via the in-situ aminolytic reaction using metal chloride precursors in oleylamine solvent/reactant.

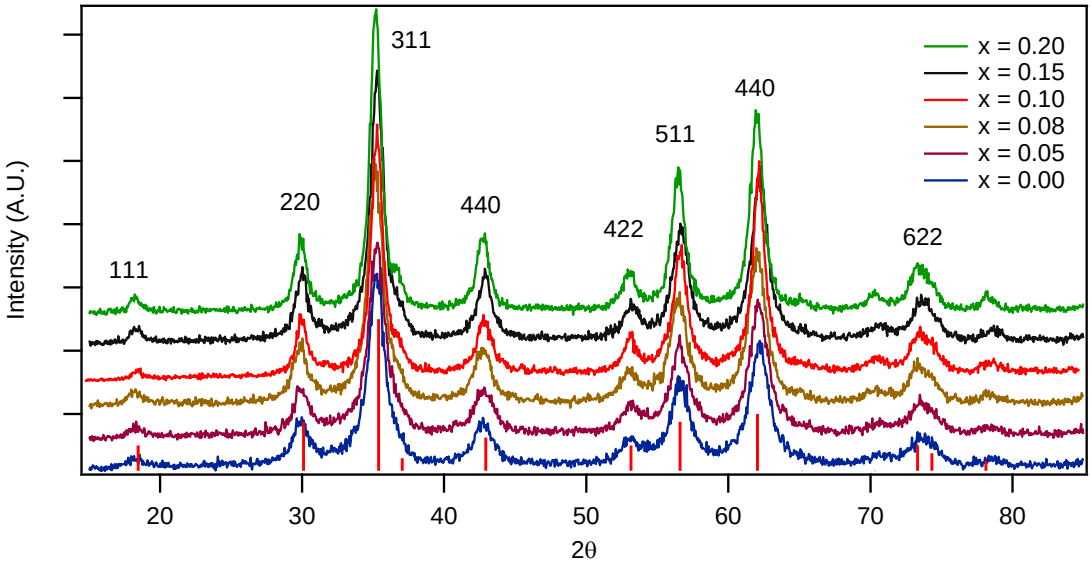

Figure 3.4.1: XRD patterns of $Cu_xMn_{1-x}Fe_2O_4$ nanoparticles

Excellent crystallinity was observed at a reaction temperature of or above 240^{o}C. Peak position and relative intensity of the products' diffraction pattern matched the standard powder diffraction pattern (ICDD File 10-319). Average particle size was calculated by the Scherrer equation using the Bragg peak broadening data and found to be ~11 nm. The sizes of the nanoparticles were calculated using the five most intense Bragg peaks. ICP-OES data confirmed the cationic ratio between Cu^{2+}&Mn^{2+}:Fe^{3+} of 1:2 was maintained for all nanoparticles produced and theoretical Mn composition calculated from the molar ratio in reagents and the actual composition in nanoparticles by elemental analysis. This data is contained in Table 3.4.1:

Table 3.4.1: ICP-OES $Cu_xMn_{1-x}Fe_2O_4$

Theoretical Cu Percentage	0	5	8	10	15	20
Actual Cu Percentage	0	5.89	8.3	9.8	15.7	20.1

Field dependent magnetization measurements at 5K show that hysteresis curve changes with increasing copper ion content of the nanoparticles (Figure 3.4.2).

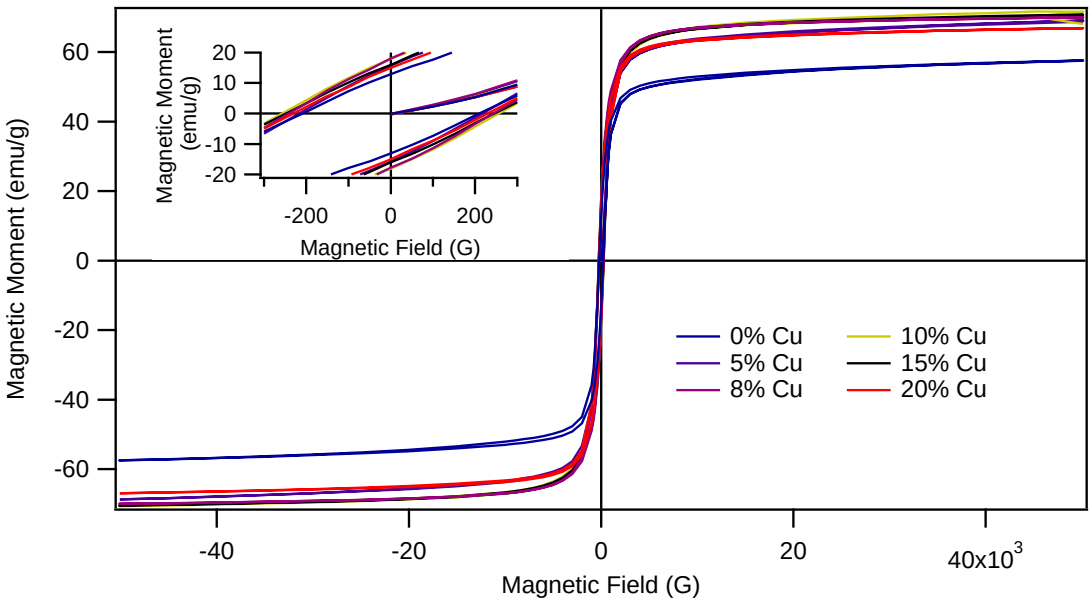

Figure 3.4.2: Field dependent measurement of $Cu_xMn_{1-x}Fe_2O_4$ nanoparticles.

For the doped nanoparticles, remnant and saturation magnetization increase with increasing copper doping (Figure 3.4.3 B and C) until 10 % replacement. At this point, there is a marked decrease in remnant magnetization and saturation magnetization. The magnetic arrangement of the spinel system is antiparallel coupling of two parallel magnetically aligned sheets. Since the octahedral and tetrahedral sites are aligned in opposite directions, doping with the copper ion on the tetrahedral sites will increase the net magnetic moment, as shown in Figure 3.4.3. This increase occurs despite the Cu^{2+} $1\mu_B$ moment compared to the $5\mu_B$ moment of Mn^{2+} ion that it replaces. This magnetic response arises because the tetrahedral sites that cancel out some of the magnetic moments of the octahedral sites now contain ions of a lower magnetic moment and increases the overall magnetic moment of the system. When the doping percent of copper hits 10%, the copper ions starts to occupy the octahedral sites. The reduced magnetic

moment of the Cu^{2+} results in a drop in the overall magnetic moment of the nanoparticle, and thus, a drop in the remnant magnetization and saturation magnetization values.

Coercivity represents the applied field strength required to surpass the anisotropy barrier and allow the magnetic moments of the nanoparticles to align with the applied field. Stoner-Wohlfarth theory shows this phenomenon with the following equation:

$$H_C = \frac{2K}{(\mu_0 M_S)} \tag{3.4.1}$$

K is the magnetic anisotropy, μ_o is the permeability of a vacuum, and M_s is the saturation magnetic[24]. Because magnetic anisotropy is directly proportional to coercivity as well as activation energy, the hysteresis loop is expected to widen as the volume of the nanoparticle increases. In order to rule this complication out and allow for the study of the copper's concentration effect on coercivity, particle size was maintained at 11 nm. The coercivity increases with increasing Cu^{2+} concentration due to the continued swapping of a low magnetic anisotropy ion (Mn^{2+}) with a higher magnetic anisotropy ion (Cu^{2+}). See Figure 3.4.3A. When the copper concentration hits 10%, the copper starts to occupy the octahedral sites, where Jahn-Teller distortion occurs and lowers the copper's orbital angular momentum contribution to its magnetic anisotropy. This, accompanied with the reduced overall magnetic moment of the nanoparticle, results in a decrease in the coercivity of the system. This reduction in the coercivity is in agreement with a lowering of the magnetization reversal energy barriers. The extent of the energy barrier decrease through a reduction of magnetic couplings results from the weaker magnetic moment of Cu^{2+}.

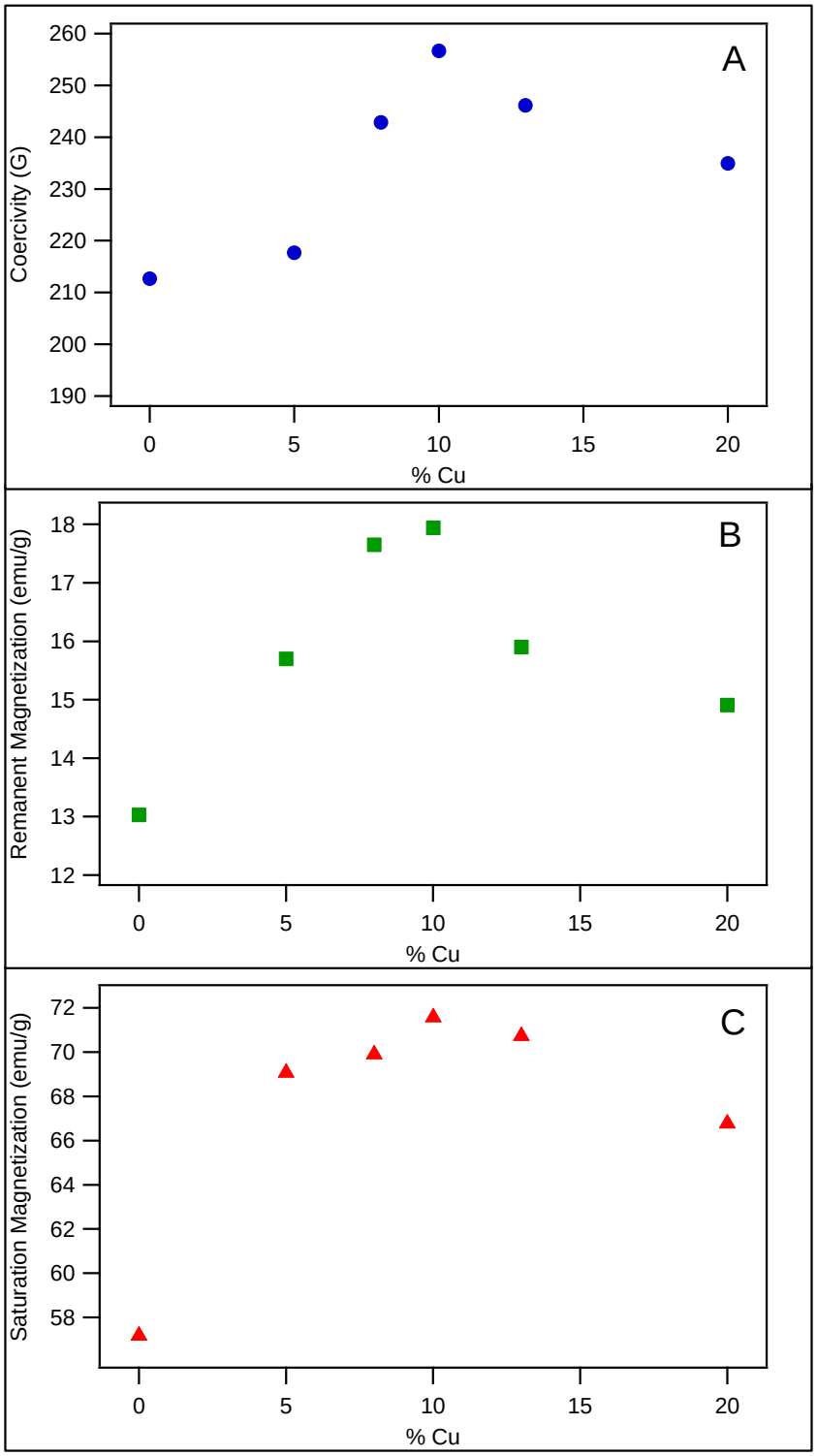

Figure 3.4.3: (A) Doping dependency of coercivity for Cu doped nanoparticles. (B) Size dependence of remnant magnetization. (C) Size dependence of saturation magnetization.

A second magnetic study was performed to investigate the effect of copper doping on the blocking temperature of the nanoparticles. The results of the magnetic susceptibility measurements can be seen in Figure 3.4.4.

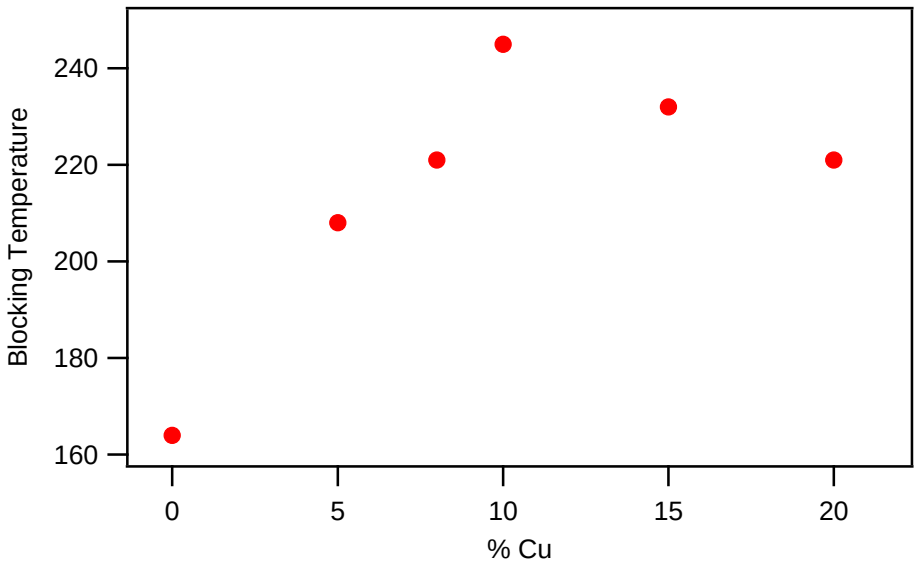

Figure 3.4.4: Blocking Temperature (T_B) dependence on copper doping for ~11 nm $Cu_xMn_{1-x}Fe_2O_4$ nanoparticles.

Stoner-Wohlfarth theory describes the energy barrier (E_A) for the rotation of magnetization orientation of single domain particle as

$$E_A = KV\sin^2\theta \qquad (3.4.2)$$

K is the anisotropy of the material, *V* is the volume of the nanoparticle, and θ is the angle between an applied magnetic field and the easy axis of magnetization. The blocking

temperature of a material is the temperature at which the magnetic moments of the nanoparticles are no longer blocked and are able to overcome the energy barrier, E_A[25]. We speculate that the blocking temperature initially increases because the activation energy barrier is increased by the increased Cu^{2+} ion occupancy of the tetrahedral sites in the spinel structure. The Cu^{2+} ions, while in the tetrahedral sites, possesses a higher magnetic anisotropy compared to Mn^{2+} due to the lack of Jahn-Teller distortion which results in a higher orbital angular momentum for copper. Mn^{2+} ions have zero angular momentum due to its electron configuration of $t_2^2e^3$, compared to Cu^{2+} whose electron configuration is $t_2^4e^5$. When the copper concentration reaches 10%, the copper starts to occupy the octahedral sites, where Jahn-Teller distortion occurs, and removes copper's orbital angular momentum contribution, and produces a decrease in the blocking temperature. This loss of orbital angular momentum results in the lowering of the magnetic anisotropy of the system, and thus leads to a reduction of the energy barrier. The extent of the energy barrier decrease through a reduction of magnetic couplings results from the weaker magnetic moment of Cu^{2+}.

3.5 Conclusion:

A series of $Cu_xMn_{1-x}Fe_2O_4$ nanoparticles, where x = 0.0, 0.05, 0.08, 0.1, 0.16 and 0.20, were synthesized via the *in-situ* aminolytic method. XRD and IC-OES were performed to ensure that the proper phase and chemical composition was obtained. The lack of impurity peaks in the XRD indicates that the ferrite structure was produced while the ICP shows that the targeted ratio of Cu&Mn:Fe was synthesized. Field dependent magnetic measurements were performed via SQUID to investigate the effect of replacing

Mn with Cu on the ferrite's magnetic properties. It was shown that initial doping with copper lead to an increase in coercivity, remnant magnetization, and saturation magnetization until 10% of the manganese was replaced. Increasing the copper percentage above 10% lead to a marked decrease in coercivity, remnant magnetization, and saturation magnetization. We feel that the initial increase in the ferrites' magnetic properties is due to the location of the copper in the tetrahedral sites of the spinel structure. Despite the lower magnetic moment of copper compared to Mn^{2+}, when copper occupies the A sites, there is an overall increase in the nanoparticle's magnetic moment due to a reduction of magnetic cancellation in the magnetic unit cell. Once above 10%, the Cu^{2+} will start to occupy the octahedral sites of the spinel structure and will result in lowering the overall magnetic moment of the system. Finally blocking temperature was calculated for the copper doped series and showed that while the copper occupied the tetrahedral sites, the blocking temperature increased. Once the system hit 10% Cu^{2+}, the copper starts to fill octahedral sites, where Jahn-Teller distortion removes orbital angular momentum, and results in a drop in T_b. The ability to tailor a nanoparticle's magnetic property by simply changing its chemical composition during synthesis will open a door into a wide range of applications, ranging from biomedicine to data storage to sensors.

3.6 References:

(1) Pascu, O.; Caicedo, J. M.; Lopez-Garcia, M.; Canalejas, V.; Blanco, A.; Lopez, C.; Arbiol, J.; Fontcuberta, J.; Roig, A.; Herranz, G. *Nanoscale* **2011**, *3*, 4811.

(2) Ren, Y.; Li, N.; Feng, J.; Luan, T.; Wen, Q.; Li, Z.; Zhang, M. *Journal of Colloid and Interface Science* **2012**, *367*, 415.

(3) Sandu, I.; Presmanes, L.; Alphonse, P.; Tailhades, P. *Thin Solid Films* **2006**, *495*, 130.

(4) Allione, M.; Torre, B.; Casu, A.; Falqui, A.; Piacenza, P.; Corato, R. D.; Pellegrino, T.; Diaspro, A. *Journal of Applied Physics* **2011**, *110*, 064907.

(5) Fannin, P. *Measurement Science and Technology*. **1993**, *4*.

(6) Phan, N. T. S.; Gill, C. S.; Nguyen, J. V.; Zhang, Z. J.; Jones, C. W. *Angewandte Chemie International Edition* **2006**, *45*, 2209.

(7) Fu, Y.; Xiong, P.; Chen, H.; Sun, X.; Wang, X. *Industrial & Engineering Chemistry Research* **2011**, *51*, 725.

(8) Yim, Y. S.; Choi, J.-S.; Kim, G. T.; Kim, C. H.; Shin, T.-H.; Kim, D. G.; Cheon, J. *Chemical Communications* **2012**, *48*, 61.

(9) Scarberry, K. E.; Dickerson, E. B.; McDonald, J. F.; Zhang, Z. J. *Journal of the American Chemical Society* **2008**, *130*, 10258.

(10) Smart, L. E., and Moore, E. A *Solid State Chemistry: An Introduction*; Taylor & Francis Group: Boca Raton, FL 2005; Vol. 3.

(11) Liu, C.; Zou, B.; Rondinone, A. J.; Zhang, Z. J. *The Journal of Physical Chemistry B* **2000**, *104*, 1141.

(12) Gingasu, D.; Mindru, I.; Patron, L.; Cizmas, C.-B. *Journal of Alloys and Compounds* **2008**, *460*, 627.

(13) Laokul, P.; Amornkitbamrung, V.; Seraphin, S.; Maensiri, S. *Current Applied Physics* **2011**, *11*, 101.

(14) Naĭden, E.; Zhuravlev, V.; Itin, V.; Terekhova, O.; Magaeva, A.; Ivanov, Y. *Physics of the Solid State* **2008**, *50*, 894.

(15) Lazarević, Z. Ž.; Jovalekić, Č.; Recnik, A.; Ivanovski, V. N.; Mitrić, M.; Romčević, M. J.; Paunović, N.; Cekić, B. Đ.; Romčević, N. Ž. *Journal of Alloys and Compounds* **2011**, *509*, 9977.

(16) Li, J.; Yuan, H.; Li, G.; Liu, Y.; Leng, J. *Journal of Magnetism and Magnetic Materials* **2010**, *322*, 3396.

(17) Li, J.-J.; Zhai, C.-X.; Liu, M.-L. *Solid State Communications* **2005**, *134*, 759.

(18) Liu, C.; Zhang, Z. J. *Chemistry of Materials* **2001**, *13*, 2092.

(19) Scano, A.; Ennas, G.; Frongia, F.; La Barbera, A.; López-Quintela, M.; Marongiu, G.; Paschina, G.; Peddis, D.; Pilloni, M.; Vázquez-Vázquez, C. *Journal of Nanoparticle Research* **2011**, *13*, 3063.

(20) Baruwati, B.; Nadagouda, M. N.; Varma, R. S. *The Journal of Physical Chemistry C* **2008**, *112*, 18399.

(21) Hou, X.; Feng, J.; Xu, X.; Zhang, M. *Journal of Alloys and Compounds* **2010**, *491*, 258.

(22) Bao, N.; Shen, L.; Wang, Y.; Padhan, P.; Gupta, A. *Journal of the American Chemical Society* **2007**, *129*, 12374.

(23) Malkinski, L.; Lim, J.-H.; Chae, W.-S.; Lee, H.-O.; Kim, E.-M.; Jung, J.-S. *Electronic Materials Letters* **2009**, *5*, 87.

(24) Leslie-Pelecky *Chem. Mater.* **1996**, *8*.

(25) Stoner, E. C.; Wohlfarth, E. P. *Magnetics, IEEE Transactions on* **1991**, *27*, 3475.

Chapter 4

Novel Synthesis of Manganese Oxide Nanoparticles and Size-Dependent Magnetic Properties

4.1 Abstract:

Manganese oxide nanoparticles have a multitude of possible applications as gas sensors, catalysts, and airborne agent traps. These nanoparticles have distinct advantages over their bulk counterparts due to unique magnetic properties and enhanced surface-to-volume ratio. In this chapter, a simple, one-pot synthesis method (aminolytic method) for the preparation of a range of different sized MnO and Mn_3O_4 nanoparticles in pure single-phase with monodispersity is reported; these nanoparticles were characterized by XRD and SQUID. Although bulk MnO is antiferromagnetic, their nanoparticles show ferromagnetic ordering at low temperatures. We believe that the material is exhibiting this magnetic behavior due to uncompensated surface spins arising from the incomplete Mn^{2+} coordination. MnO nanoparticles also show an inverse relation of magnetic properties with size. As the size of the nanoparticle is decreased, the blocking temperature as well as coercivity, saturation magnetization, and remnant magnetization also decreases. It is believed that this is due to the high number of uncompensated spins contained in the samples with the smaller nanoparticles and the high ratio of size-to-volume that accompanies them. Spinel Mn_3O_4 nanoparticles were characterized using the same methods as above. Mn_3O_4 showed the expected trends in their magnetic measurements, in that the coercivity, magnetization saturation, and remnant

magnetization all increased with an increase in nanoparticle volume, which agrees with the Stoner-Wohlfarth model. Finally a core/shell system was creating using the aminolytic method to grow a MnO shell on a $CoFe_2O_4$ core.

4.2 Introduction:

Research into manganese oxides (MnO and Mn_3O_4) over the past few years has increased due to the nano-revolution. Studying nanoscaled MnO and Mn_3O_4 has allowed for the investigation of the fundamental characteristics of magnetic ordering, which has opened up avenues for their integration into novel applications. These nanoparticles have a wide range of potential applications, as electrode material for lithium-ion batteries[1,2], ion exchange resins [3,4], microelectronics[3,4], soft magnetic materials[5,6], catalysts[7,8], and sensors[9,10].

These applications are possible due to MnO's unique magnetic properties on the nanoscale. Due to bulk MnO's NaCl-type crystal structure, it is paramagnetic at room temperature. As the temperature is decreased below its Néel temperature of 118K[11], it transitions from a paramagnetic to an antiferromagnetic state. When the crystallite size of MnO is reduced to the nanometer scale, the material develops ferromagnetic ordering rather than antiferromagnetism. Investigation into the possible mechanism for the appearance of this ferromagnetism will be included in this paper.

Mn_3O_4 belongs to the spinel class of metal oxides where Mn^{2+} occupies the tetrahedral sites and Mn^{3+} occupies the octahedral sites. At room temperature, the stable structure is a tetragonal hausmannite with the space group $I4_1|amd$ (a = 5.762 Å, c= 9.470Å).[12] Jahn-Teller distortion in Mn^{3+} results in oxygen octrahedral distortion in a

tetragonal fashion. A Jahn-Teller transition, a first order transition which occurs around 1200^{o}C, results in considerable lattice deformation and further heating transforms the structure into a pure cubic crystal structure.

In order to study MnO and Mn_3O_4's unique magnetic properties as well as the possibility for utilization in current technologies, a simple, cheap, fast method producing highly crystalline monodisperse nanoparticles is needed. Over the last few years, several different synthetic methods have been published, including but not limited to vapor deposition[13], sol-gel[14,15], thermal decomposition[16-18], nonaqueous synthesis[19], and sonochemical[20] methods. While each technique has its advantages, there are also drawbacks that complicate their ability to be useful on the industrial scale. Vapor deposition allows for the production of highly crystalline nanoparticles, but requires high temperatures and monitoring of the reaction atmosphere to prevent impurities. The sol-gel method allows for control over morphology and particle size, but it suffers from slow reaction times, exact pH control, high calcination temperatures, and requires an inert atmosphere or protecting agent. The thermal decomposition method results in highly crystalline nanoparticles of tight size distributions, but it is limited by the need for specialized surfactants and solvents, impurities in the product, and proper storage requirements (inert atmosphere). The nonaqueous method maintains control over particle shape, size, and distribution; however, it does require the use of a glove box and long reaction times. Although the sonochemical method utilizes specialized equipment and high calcination temperatures, it produces particles with monodispersity as well as high crystallinity.

Herein a fast, simple, cheap, one-pot synthesis technique for the production of MnO and Mn_3O_4 nanoparticles via the aminolytic method is reported. This technique involves a controlled reaction of Mn-acetate and oleylamine, by means of an amide bond formation followed by a condensation reaction to form the metal oxide. It also allows for the separation of the nucleation and growth stages of nanoparticle formation, which results in controlled morphology and size distribution. The use of a simple non-coordinating, high-boiling solvent and surfactant, as well as forgivable atmosphere requirements, causes this method to be more apt for the industrial formation of MnO and Mn_3O_4 nanoparticles. Investigation into MnO's unusual magnetic properties present in the nanoscale and a discussion of a possible mechanism to explain these abnormal properties are included below. Structural and magnetic properties of the Mn_3O_4 nanoparticles produced are also discussed. Finally the aminolytic method's versatility is tested further by the synthesis of a core/shell system. The addition of MnO to a highly magnetic core, such as $CoFe_2O_4$, will increase its relevance to catalytic applications. By adding manipulability, separation of the MnO catalyst from a product would help in reducing production costs incurred by purification and separation requirements.

4.3 Experimental:

4.3.1 Precursor:

Manganese acetate precursor was prepared as follows. $MnCl_2 \cdot 4H_2O$ (40 mmol) in 100 mL distilled water and stirred for 30 minutes under ambient conditions. Upon the addition of 100 mL of 1 M NaOH solution, a light brown metal hydroxide precipitate formed. The mixture was stirred for another hour and then the precipitate was collected

via centrifugation. The solid was washed several times with distilled water. The Mn-hydroxide was dissolved in 50 mL of glacial acetic acid (99%) and heated at 70°C overnight. Upon complete evaporation of the liquid, a fine powder of $Mn^{2+}(CH_3COO^-)_2$ was collected.

4.3.2 MnO:

All samples of MnO were synthesized via the aminolytic reaction. Manganese acetate (~1.5 g) was dissolved in a mixture of 20 mL oleylamine and 30 mL dibenzyl ether under an argon atmosphere at 140ºC for one hour. The temperature was raised to 240ºC at a ramping rate of 5ºC/min, and the solution was agitated for an additional hour. Upon cooling to room temperature, the nanoparticles were separated via centrifugation (at 2000 rpm for 10 minutes), washed three times using absolute ethanol, and dried in air overnight.

4.3.3 Mn_3O_4:

All samples of Mn_3O_4 were synthesized via the aminolytic reaction. Manganese acetate (~1.5 g) was dissolved in 30 mL oleylamine and 20 mL dibenzyl ether under an argon and oxygen atmosphere at 140ºC for one hour. The temperature was raised to 200ºC at a ramping rate of 5ºC/min, and the solution was stirred for an additional hour. Upon cooling to room temperature, the nanoparticles were separated via centrifugation (at 2000 rpm for 10 minutes), washed four times using absolute ethanol, and dried in air overnight.

4.3.4 $CoFe_2O_4$/MnO Core/Shell Synthesis

Core/shell $CoFe_2O_4$/MnO nanoparticles were prepared via the aminolytic method. Manganese acetate, made in-house, and $CoFe_2O_4$ cores (prepared prior to coating via the aminolytic method) were added to a mixture of 15 mL dibenzyl ether and 5 mL oleylamine and heated to 140^{o}C under argon gas flow for one hour. The temperature was raised to 240^{o}C at a ramping rate of 5^{o}C/min and held there for another hour. The particles were collected using a strong magnet, washed several times with absolute ethanol, and dried overnight in air.

4.3.5 Instrumentation:

X-ray diffraction (XRD) data was collected with a Panalytical X'pert Pro X-Ray Diffractometer with a copper Kα source over a 15º – 85º 2θ range. Particle size was determined from the average peak broadening of the five strongest Bragg peaks using the commercial program IGOR and the Debye-Scherrer equation assuming a shape factor of 0.9 (spherical). Magnetic measurements were performed using a Quantum Design MPMS-5S SQUID magnetometer. Particles were immobilized in icosane ($C_{20}H_{42}$, Aldrich) for hysteresis measurements. Transmission electron microscopy (TEM) studies were performed using a JEOL 100CX2 instrument operating at 100 kV.

4.4 Data/Discussion:

4.4.1 MnO:

The nanoparticles synthesized via the aminolytic method using manganese acetate, oleylamine, and dibenzyl ether are pure halite-phased MnO as indicated by the X-ray diffraction pattern shown in Figure 4.4.1. The absence of impurity peaks and the sharpness of the peaks show that the material is highly crystalline and pure. The peak position and relative intensity of the products' diffraction patterns match the standard powder diffraction pattern (ICDD File Number 4-326). A commercial program, IGOR, and the Debye-Scherrer equation, which utilizes Bragg peak broadening, was used to calculate the average size of the nanoparticles and is indicated in Figure 4.4.1.

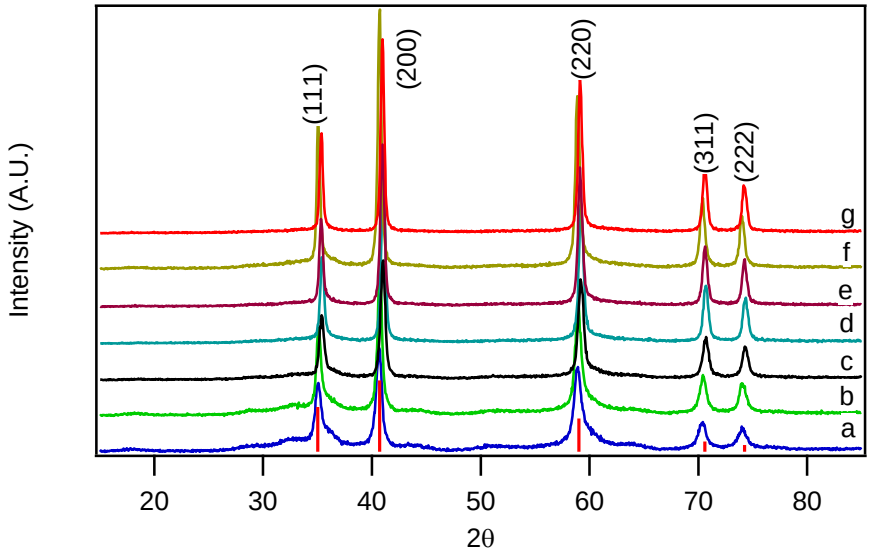

Figure 4.4.1: XRD of MnO nanoparticles produced (a) 11.5 nm, (b) 15.0 nm, (c) 17.0 nm, (d) 20.6 nm, (e) 21.9 nm, (f) 22.6 nm, (g) 24 nm.

TEM images of a representative sample of MnO nanoparticles synthesized by our method are shown in Figure 4.4.2. This sample was calculated from the XRD patter and Debye-Scherrer equation and found to have an average size of 20 nm. As it can be seen from the image, the nanoparticles are sphere-like, with an average size of 19.1 nm that corresponds well with the calculated size of 20 nm. The size distribution of the nanoparticles from the TEM images is about 11%.

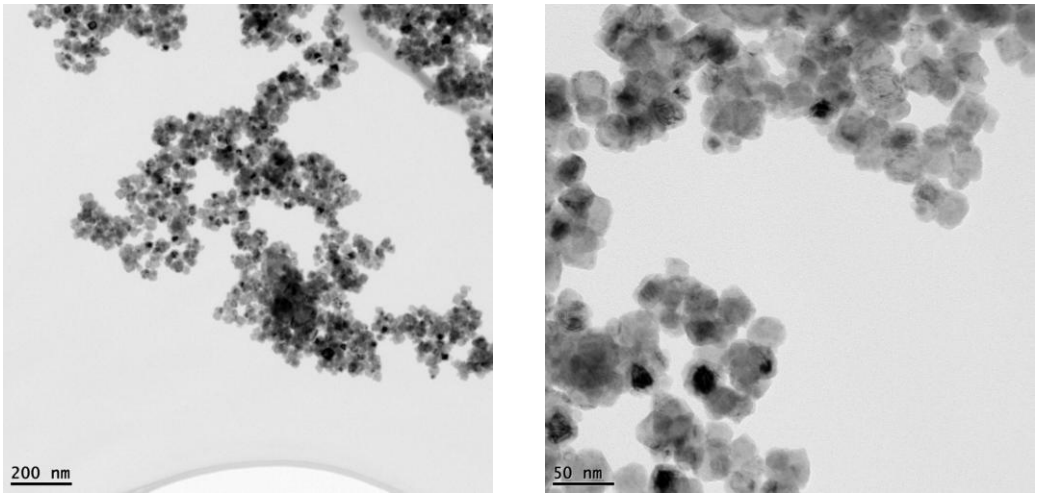

Figure 4.4.2: TEM of ~19 nm MnO nanoparticles.

It has been reported that MnO nanoparticles show slight ferromagnetic ordering, despite bulk MnO possessing antiferromagnetic ordering with a T_N of 122 K[11]. In those previous reports, this magnetism was attributed to uncompensated spins due to reduced surface manganese coordination at the nanoparticle surface. Figure 4.4.3 shows the temperature-dependent magnetic susceptibility measurements at 100 G of various-sized nanoparticles.

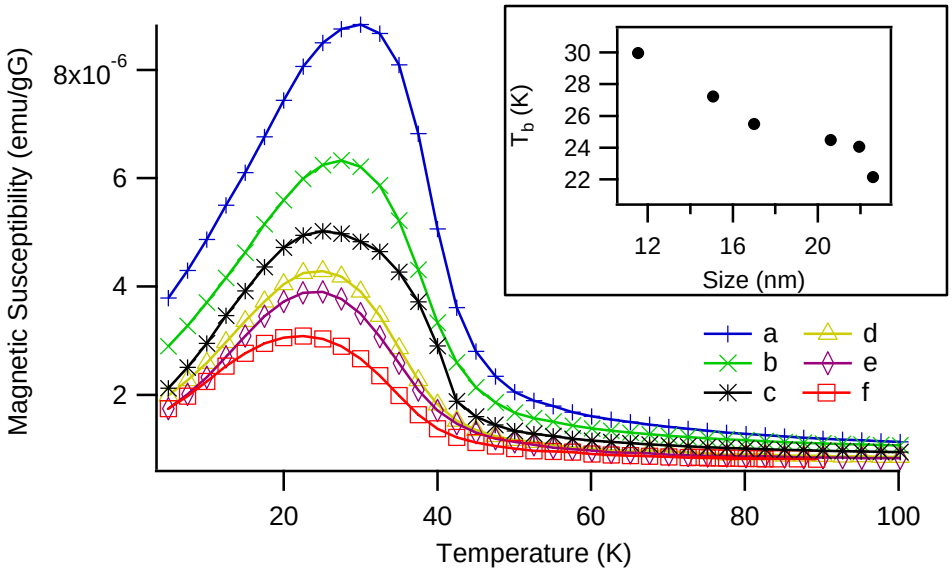

Figure 4.4.3: Temperature-dependent magnetization of MnO nanoparticles. (a) 11.5 nm, (b) 15.0 nm, (c) 17.0 nm, (d) 20.6 nm, (e) 21.9 nm, (f) 22.6 nm. Inset shows the size dependence on the blocking temperature of the nanoparticles.

As it can be seen, there is an inverse relation between the magnetic susceptibility and size of the MnO system. As the size of the nanoparticle is reduced, there is an increase in susceptibility. Since the ferromagnetism that is measured at low temperatures is due to the uncompensated spins that occur at the particle surface, the systems that have a larger surface area per gram (smaller nanoparticles) will result in more surface spins and therefore a higher magnetic susceptibility than the systems that have a lower surface area (larger nanoparticles). From this figure, blocking temperatures (T_B) of different sizes of nanoparticles were calculated. There is an inverse dependence of blocking temperature on size that is better visualized with the inset for Figure 4.4.3. As the size of the nanoparticle is increased, the blocking temperature decreases. The range of the blocking

temperatures from largest to smallest nanoparticle system is quite small, ~8 K. The blocking temperature range for a similarly sized cobalt ferrite nanoparticles would be ~100 K[21]. Since the range is quite small for the MnO system, the cause of this inverse relation can only be speculated on. What is believed to be occurring is a change in the mechanism that causes the magnetic moments to align. In larger nanoparticles, the overall energy of the nanoparticle is reduced by the parallel alignment of the spins with the surface. When enough thermal energy is added to the system, the spins will utilize a curling mechanism to align the moments with the applied field[22]. This mechanism requires a lower amount of thermal energy and thus results in a lower blocking temperature. The smaller nanoparticles, on the other hand, do not force the spins parallel to the surface, and result in a higher fraction of spins that are perpendicular[22]. In order to align the moments with an applied field, a coherent turning mechanism is employed, requiring more thermal energy, and results in a higher blocking temperature.

Field-dependent magnetization measurements performed at 5 K show expected hysteresis curves, as seen in Figure 4.4.4. The coercivity, remnant magnetization, and saturation magnetization decrease with increasing particle size (Figure 4.4.5).

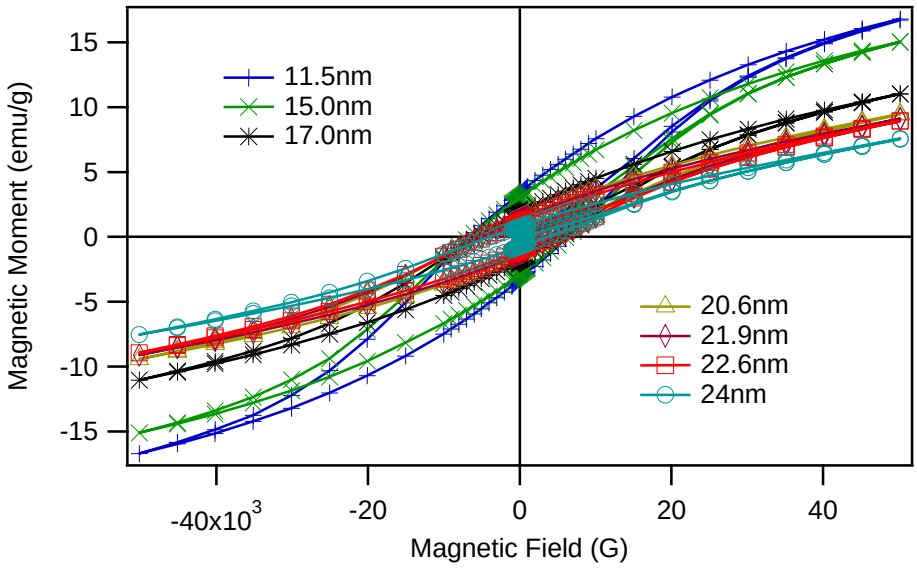

Figure 4.4.4: Hysteresis curves for MnO nanoparticles at 5 K.

The coercivity of single domain nanoparticles is the magnetic field strength needed to surpass the anisotropy barrier and allows the magnetic moments of the nanoparticle to align with the applied field[23]. Since MnO is antiferromagnetic at 5 K, the coercivity shown in Figure 4.4.4 and the inverse correlation of size and coercivity seen in Figure 4.4.5A arises from the uncompensated spins on the surface of the particles. As described earlier, the larger nanoparticles, in an effort to reduce the overall energy of the system, the spins will align parallel to the nanoparticle surface. These particles will use a curling mechanism in order to align the moments with the applied field. This mechanism requires a lower amount of field strength to cause full alignment and results in a lower coercivity. The smaller nanoparticles, whose spins are more perpendicular to the surface, will use the coherent turning mechanism to fully align the moments. This requires stronger field strength and, thus, a higher coercivity.

The amount of magnetization that remains in the system once the magnetic field is removed is known as remnant magnetization[24]. In this system, there is an inverse relationship of remembrance with size, as seen in Figure 4.4.5B. As the particle size increases, the remnant magnetization decreases. This is once again due to the large number of spins per volume that the smaller nanoparticles possess.

Saturation magnetization is the state reached when an increase in an applied external field cannot increase the magnetization of the system[24]. Shown in Figure 4.4.5C, there is an increase in saturation as the average size of the nanoparticles decreases. As the average particle size of the system increases, the number of spins per volume decreases and leads to an overall lower saturation magnetization.

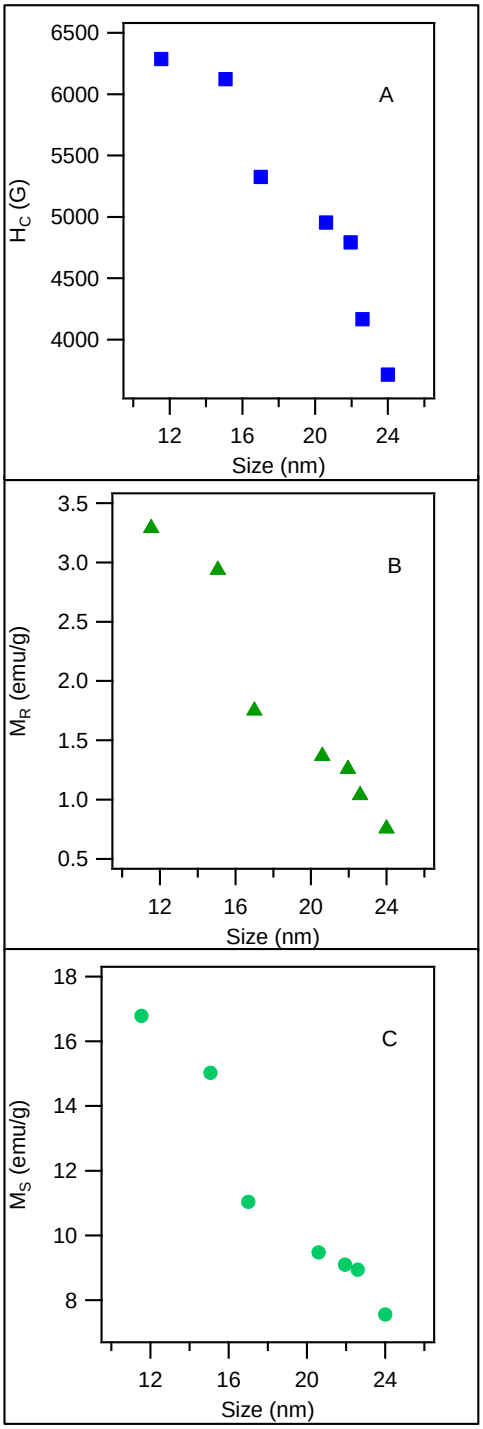

Figure 4.4.5: (A) Size dependence of coercivity for MnO nanoparticles. (B) Size dependence of remnant magnetization. (C) Size dependence of saturation magnetization.

4.4.2 Mn_3O_4:

The nanoparticles that were created using the aminolytic method utilizing manganese acetate, oleylamine, and dibenzyl ether under a mix of argon and oxygen are pure hausmannite-phased Mn_3O_4, as indicated by the X-ray diffraction pattern shown in Figure 4.4.6.

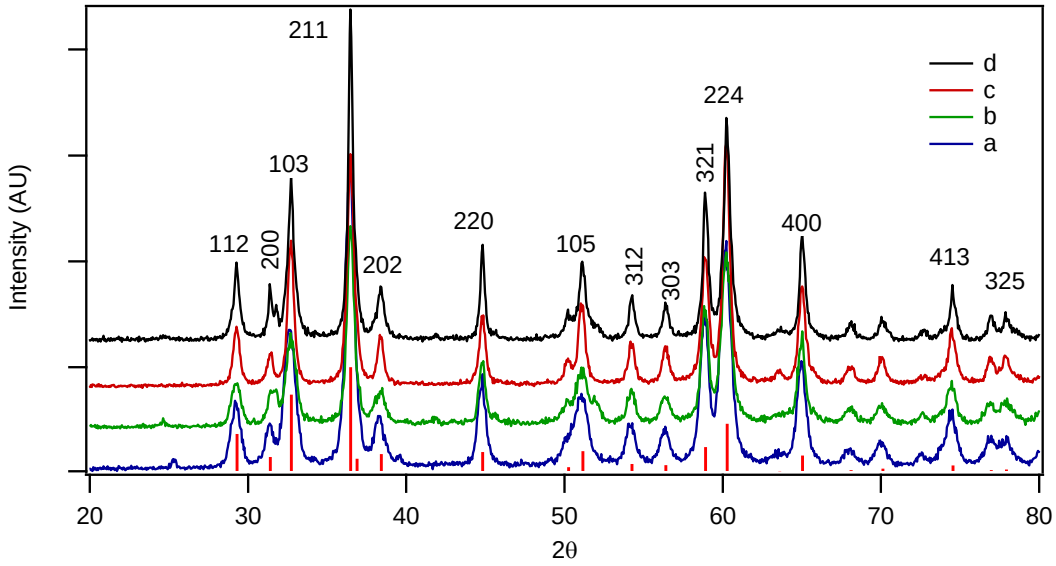

Figure 4.4.6: XRD of Mn_3O_4 nanoparticles (a) 16.5 nm, (b) 19.0 nm (c) 22.7 nm, (d) 26.1 nm.

The absence of impurity peaks and the sharpness of the peaks show that the particles are highly crystalline and pure. The peak position and relative intensity of the products' diffraction patterns match the standard powder diffraction pattern (ICDD File Number 04-007-1841). A commercial program, IGOR, and the Debye-Scherrer equation, which utilizes Bragg peak broadening, was used to calculate the average size of the nanoparticles and is indicated in Figure 4.4.6.

It has been reported that Mn_3O_4 nanoparticles are ferrimagnetic with a Curie temperature of 41 K[25]. Above this temperature, the nanoparticles are paramagnetic; however, below this temperature, the material has antiferromagnetic ordering with incomplete cancellation of magnetic moments from the Mn^{3+} and the Mn^{2+}, resulting in ferrimagnetic behavior. This is due to the uneven number of Mn^{3+} in octahedral sites (16) and Mn^{2+} in tetrahedral sites (8) that is found in the spinel class of nanoparticles.

Field-dependent magnetization measurements at 5 K show the expected hysteresis curves and can be seen in Figure 4.4.7. The coercivity, remnant magnetization, and saturation magnetization dependence on size can be seen in Figure 4.4.8.

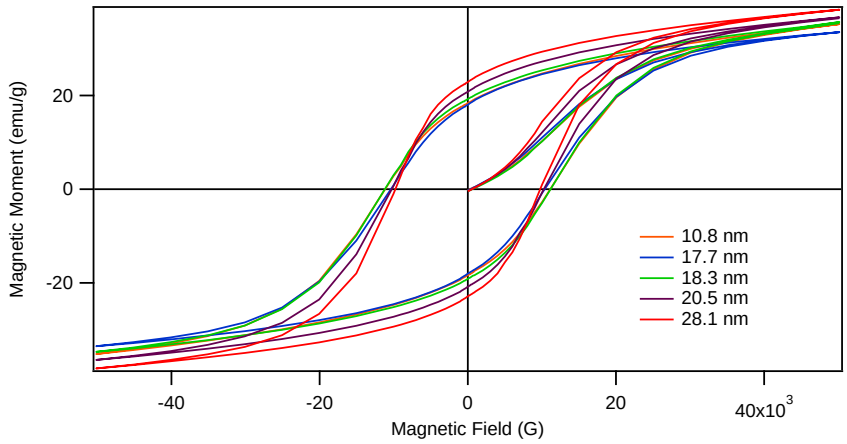

Figure 4.4.7: Hysteresis curves for Mn_3O_4 nanoparticles at 5 K.

As the size of the nanoparticles increase, there is an associated increase in saturation magnetization. This is expected for when the volume of the nanoparticles increases, there is an increase in the number of net magnetic moments contained in an individual nanoparticle. With more magnetic moments present, a higher maximum magnetic saturation is possible when an external magnetic field is applied. This trend can

be seen in Figure 4.4.8A. Following the same trend as saturation magnetization, remnant magnetization also increases with an increase in nanoparticle volume. This again is due to the increase in net magnetic moments that accompanies an increase in volume. With more moments present, the particle will retain a higher amount of the applied magnetic field once it has been removed (Figure 4.4.8B). A similar trend occurs with coercivity in this series of Mn_3O_4 nanoparticles to a certain point. There is an increase in the field strength needed to align the moments of the nanoparticles, until about 18.3 nm, where a decrease in coercivity occurs. This trend can be seen in Figure 4.4.8C.

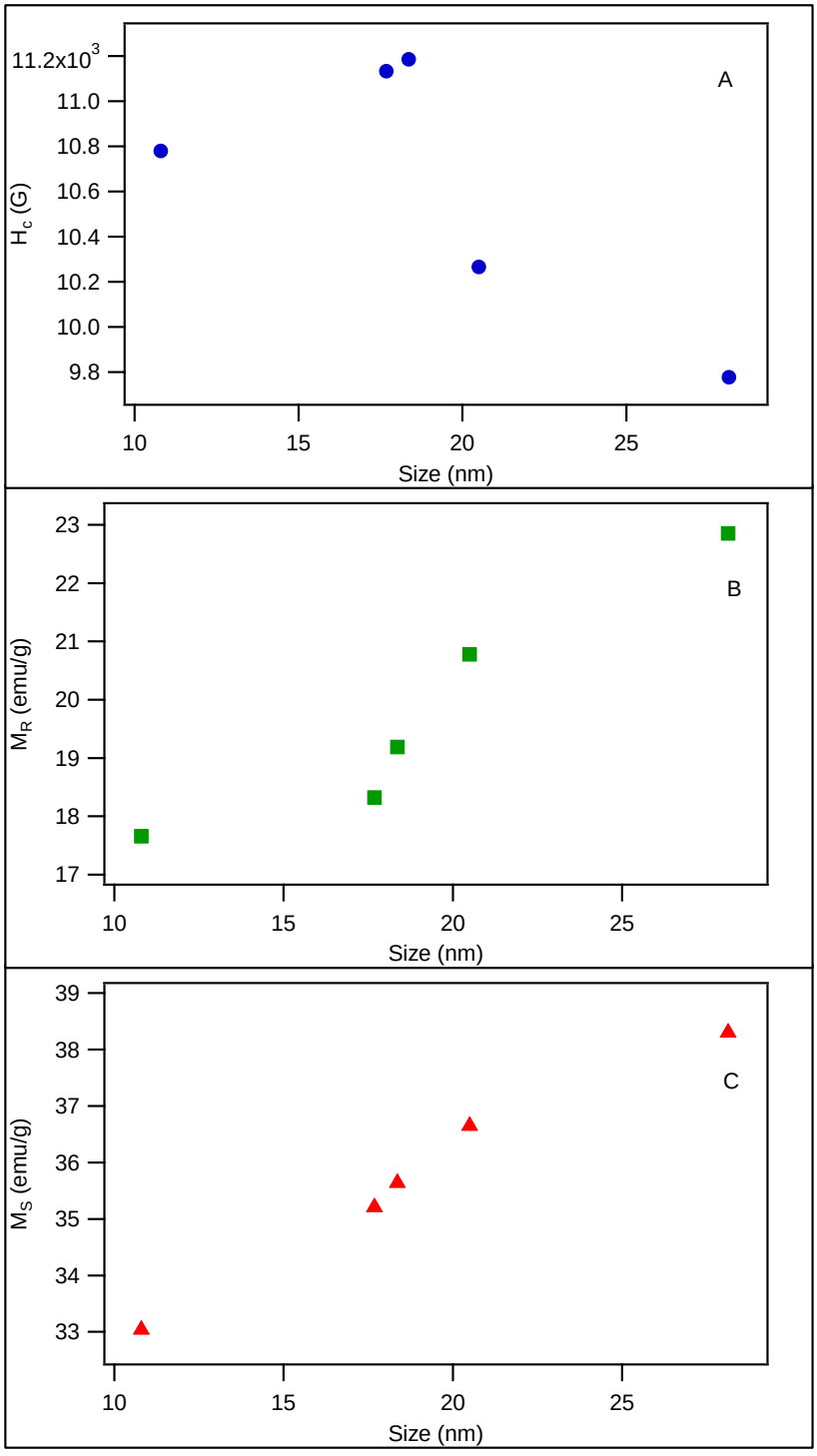

Figure 4.4.8: (A) Size dependence of coercivity for Mn_3O_4 nanoparticles. (B) Size dependence of remnant magnetization. (C) Size dependence of saturation magnetization.

Coercivity is the field strength required to overcome a magnetization reversal energy barrier at a given temperature. There are several different mechanisms that can be used to cause magnetization reversal: coherent rotation, magnetization curling, and domain wall motion. Since the size of the nanoparticles is kept small, coherent rotation and curling are the most important, as there are no domain walls to move. The increase in coercivity until 18.3 nm is consistent with an increase magnetization reversal barrier. The change from an increase to a decrease in coercivity with an increase in nanoparticle size does not fit with magnetic anisotropy. This indicates a change of mechanism for magnetic reversal from coherent rotation to curling. For smaller nanoparticles, the magnetostatic energy (the energy of a magnet in its own field) needed for coherent reversal is less than the exchange energy needed for curling and results in the preference of reversal via coherent rotation. Once the size of the nanoparticles crosses 18.3 nm, there is a lower energy cost of exchange energy versus magnetostatic energy, and results in the use of curling mechanism for magnetic reversal. With regards to the curling mechanism, the total exchange energy during reversal increases with an increase in particle size at a less than linear rate, resulting in a coercivity decrease with particle diameter increase. This can be explained via the following equation:

$$h_{ci} \geq \frac{2}{3} - \frac{1.39}{(D/D_0)^2} \qquad (4.4.1)$$

Where h_{ci} is coercivity, D is the diameter of the nanoparticle and D_0 is described as:

$$D_0 = \frac{2A^{1/2}}{M_S} \tag{4.4.2}$$

A is the exchange constant (force keeping adjacent spins parallel) and M_S is the saturation magnetization of the particle. This shows that for small nanoparticles, coherent rotation is the preferred mechanism for magnetic reversal, while for larger particles curling is utilized.

4.4.3 $CoFe_2O_4$/MnO Core/Shell

The core/shell system was synthesized using a $CoFe_2O_4$ nanoparticle core that was produced via the aminolytic method. This is important in that the ferrite core was coated with unreacted oleylamine surfactant. This coating allows for the manganese acetate to react at the core's surface rather than the solution. The amount of manganese acetate precursor added to the system was intentionally kept low as to prevent the formation of seeds in the dibenzyl ether. When the synthesis was completed, the product was collected utilizing a magnetic field. Since MnO is paramagnetic at room temperature, some MnO nanoparticles that may have formed within the solution may also have been collected. In order to remove this undesired product, the particles collected were suspended in an ethanol solution and magnetically separated using a magnet and a peristaltic pump(Variable Flow mini-pump). Since the $CoFe_2O_4$ core has a strong magnetic interaction, the coated nanoparticles will be attracted to the magnets, while the far less magnetically interacting MnO will pass the magnets into a separate beaker. This allows for the collection of only the MnO coated cores. Figure 4.4.9 shows an XRD of

core/shell sample. The blue pattern corresponds to the $CoFe_2O_4$ core before any coating occurs while the red pattern is the magnetic core coated with MnO.

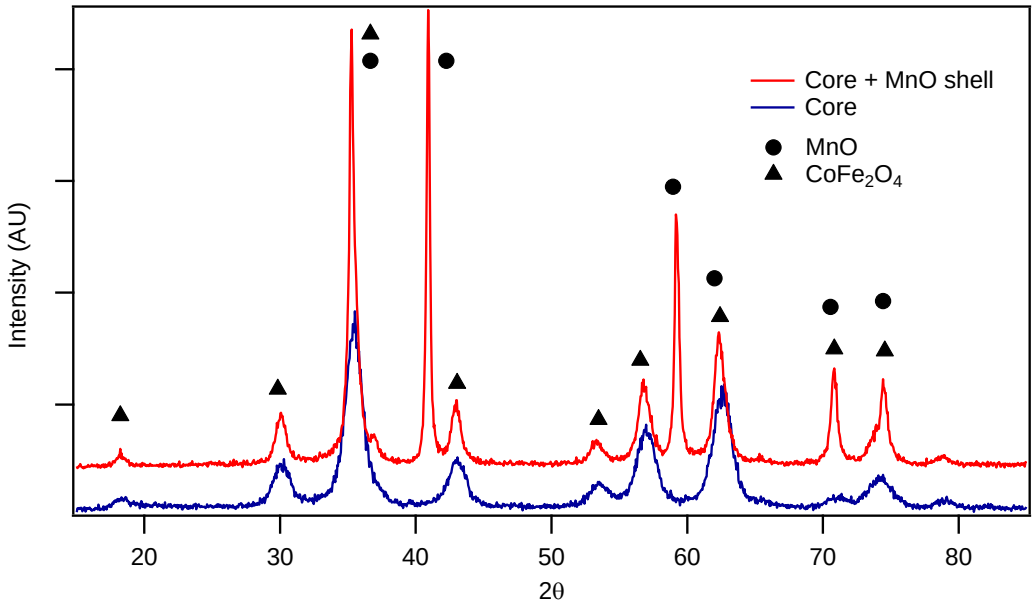

Figure 4.4.9: XRD pattern of the core/shell system. Blue pattern indicates the $CoFe_2O_4$ core. The red pattern is the $CoFe_2O_4$/MnO core shell system.

The various peaks have been labeled with the corresponding phase contributor. As seen in Figure 4.4.9, each peak is attributed to either MnO or the $CoFe_2O_4$ core. Using the commercial program IGOR and Scherrer equation for the peak broadening of XRD patterns, the average size of the core was 7.0 nm while the MnO shell was calculated to be 4.1 nm.

Since both the core and the shell show magnetic properties, investigation into the magnetic properties of the core/shell system was performed. The first magnetic

measurement taken was temperature-dependent. The core and the core/shell system were both measured and compared and can be seen on Figure 4.4.10.

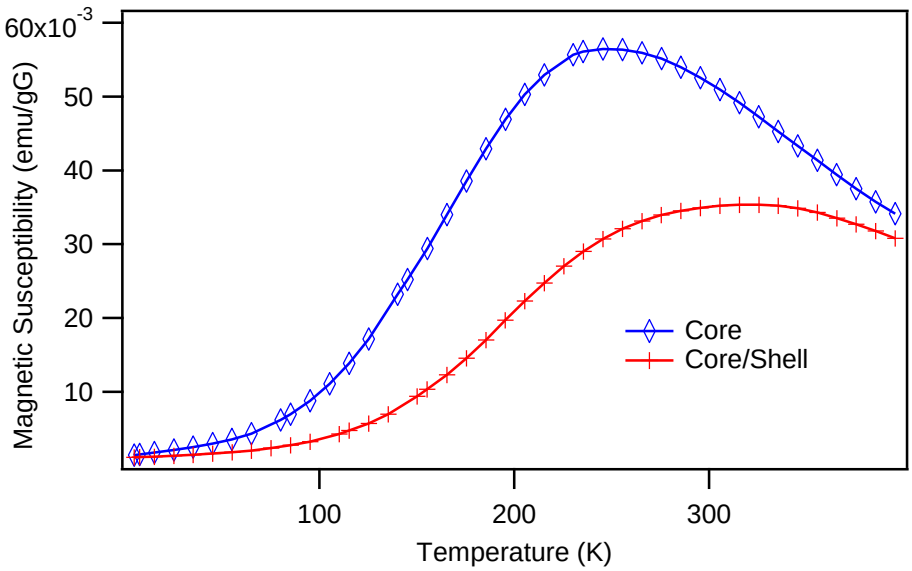

Figure 4.4.10: Temperature dependent measurement of the $CoFe_2O_4$/MnO core/shell system at 100 G

The first thing to note is the increase in blocking temperature of the core/shell (320 K) compared to the core alone (249 K). Stoner-Wohlfarth theory describes the energy barrier (E_A) for the rotation of magnetization orientation in a single domain particle:

$$E_A = KV\sin^2\Theta \qquad (2.4.1.1)$$

where *K* is the anisotropy of the material, *V* is the volume of the nanoparticle, and Θ is the angle between an applied magnetic field and the easy axis of a nanoparticle. The

blocking temperature of a material is the temperature at which the moments of the nanoparticle are no longer blocked and thus are able to overcome the energy barrier, E_A. This increase in T_B is due to the MnO's magnetic moment contribution to the system. The volume of the core does not change; however, by adding the MnO shell, the volume of magnetic material does increase, leading to a higher blocking temperature. Since MnO alone shows some magnetic ordering, it is expected that by adding it to a $CoFe_2O_4$ core, the temperature required to transition from a magnetically ordered state to a superparamagnetic state will be higher. The second thing to note in the temperature-dependent plot is the decrease in magnetic susceptibility of the core/shell compared to the core. The y-axis on a temperature-dependent plot is normalized for the weight of the sample measured. When the core is coated in MnO, the weight of the nanoparticle becomes a combination of $CoFe_2O_4$ and MnO. MnO's magnetic susceptibility is quite low compared to $CoFe_2O_4$; therefore, one gram of $CoFe_2O_4$ core will have more of the higher magnetically susceptible material compared to one gram of the $CoFe_2O_4$/MnO core/shell and would result in a higher magnetic susceptibility plot. This is exactly what can be seen in the plot that is shown in Figure 4.4.10.

The second magnetic study performed on the core/shell system was a field-dependent measurement. The results of this study can be seen in Figure 4.4.11.

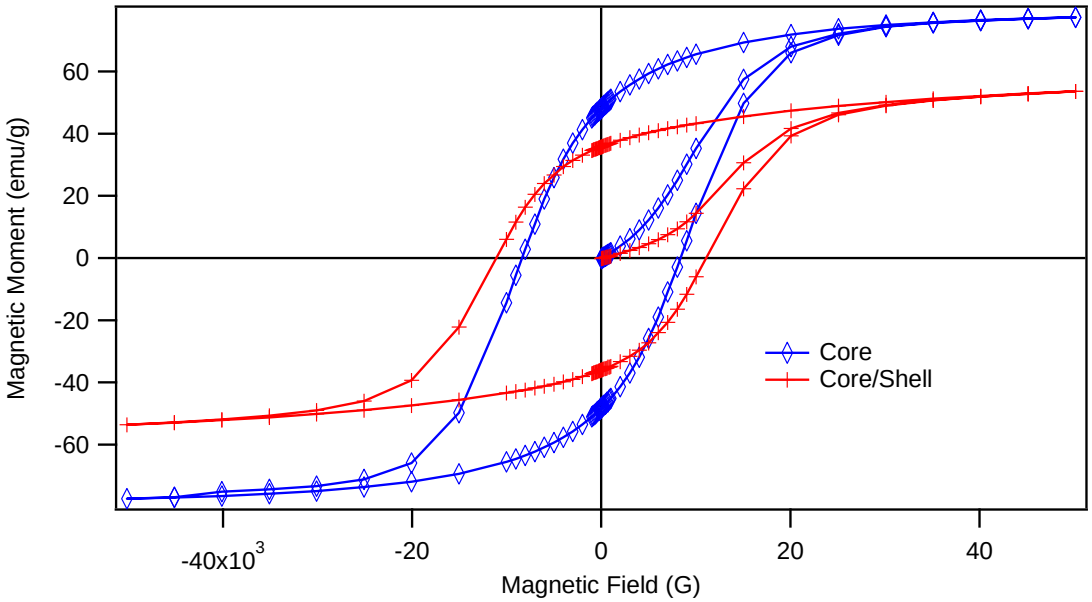

Figure 4.4.11: Hysteresis curves $CoFe_2O_4$/MnO core/shell system at 5 K.

The blue hysteresis loop is the core, while the red loop is the core/shell system. As expected, the saturation magnetization of the core/shell is lower when compared to the core. This again is due to the coating of a core that possesses a large overall magnetic moment with a material of a lower overall magnetic moment. Per gram, the core/shell system has a lower combined magnetic moment when compared to the core alone, and therefore is unable to reach the same saturation value. This is also true of the remnant magnetization. The core/shell system is unable to retain as much of the magnetic field after it has been removed when compared to the same amount of the core alone. The final feature to note is the increase in the coercivity of the core/shell system compared to the core alone. Coercivity is the field strength needed to surpass the anisotropy barrier and to allow the magnetization of the nanoparticles to align with the field. This is described by the Stoner-Wohlfarth theory.

$$H_c = 2K/(\mu_o M_s) \quad (4.4.1)$$

where μ_o is the vacuum permeability, M_s is the magnetic saturation, and K is the anisotropy of the system. K is composed of two anisotropy values and can be described as

$$K = K_{xtal} + (6/d)K_s \quad (4.4.2)$$

where K_{xtal} is the magnetocrystalline anisotropy, d is the diameter of the particle, and K_s is the surface anisotropy. Since the overall volume of the magnetic core/shell is higher than the core alone, which leads to a higher blocking temperature, it is expected that the hysteresis would increase, due to the increase in the particle's overall magnetic moment. The hysteresis increase could also be due to an increase in the magnetocrystalline anisotropy, surface anisotropy, or a combination of these two. It is not certain whether either of these values is increasing due to the addition of the MnO shell, but a decrease in surface anisotropy can be ruled out. If it did in fact decrease, the hysteresis of the core/shell system is expected to be lower than the core alone.

4.5 Conclusion:

Synthesis of manganese oxide via the aminolytic reaction utilizing oleylamine and dibenzyl ether has been demonstrated, and the trend in magnetic properties regarding size is in agreement with literature values[17]. We believe the magnetic properties of the MnO nanoparticles are due to the uncompensated spins at the surface, which is increased for

the smaller nanoparticle samples due to enhanced surface-to-volume ratio. We have also discussed a possible mechanism to describe the abnormal trends witnessed in these systems. These materials should be good candidates for chemical sensor applications since large changes in magnetic properties are expected when exposed to various environments.

We have also shown that, with a slight change in reaction conditions, the product can be tuned to produce Mn_3O_4 nanoparticles. It was shown that these particles are phase-pure and contain no impurities. Field-dependent magnetic measurements were performed on this system and showed the M_R and M_S both increase with an increase in nanoparticle size, as expected. The hysteresis of the Mn_3O_4 nanoparticles increased with size until ~18 nm, where the mechanism for magnetic alignment changed from a coherent turning to a curling effect.

The aminolytic method was also employed for the creation of a core/shell system using $CoFe_2O_4$ nanoparticles as the core and MnO for the shell. We have accounted for all peaks in the XRD as belonging to the $CoFe_2O_4$ core or the MnO shell, with no impurity peaks. We have also shown the results for the temperature-dependent and the field-dependent magnetic measurements and explained all changes in the magnetic behavior of the core when compared to the core/shell.

4.6 References

(1) Wei, W.; Cui, X.; Mao, X.; Chen, W.; Ivey, D. G. *Electrochimica Acta* **2011**, *56*, 1619.

(2) Wu, M.-S.; Lee, R.-H. *Journal of Power Sources* **2008**, *176*, 363.

(3) Chen, Z. W.; Jiao, Z.; Wu, M. H.; Shek, C. H.; Wu, C. M. L.; Lai, J. K. L. *Progress in Materials Science* **2011**, *56*, 901.

(4) Fang, M.; Tan, X.; Liu, M.; Kang, S.; Hu, X.; Zhang, L. *Cryst. Eng. Comm.* **2011**, *13*, 4915.

(5) Ahmad, T.; Ramanujachary, K. V.; Lofland, S. E.; Ganguli, A. K. *Journal of Materials Chemistry* **2004**, *14*, 3406.

(6) Park, J.; Kang, E.; Bae, C. J.; Park, J.-G.; Noh, H.-J.; Kim, J.-Y.; Park, J.-H.; Park, H. M.; Hyeon, T. *The Journal of Physical Chemistry B* **2004**, *108*, 13594.

(7) Phan, N. T. S.; Gill, C. S.; Nguyen, J. V.; Zhang, Z. J.; Jones, C. W. *Angewandte Chemie International Edition* **2006**, *45*, 2209.

(8) Ramesh, K.; Chen, L.; Chen, F.; Liu, Y.; Wang, Z.; Han, Y.-F. *Catalysis Today* **2008**, *131*, 477.

(9) Kim, I.-B.; Han, M. H.; Phillips, R. L.; Samanta, B.; Rotello, V. M.; Zhang, Z. J.; Bunz, U. H. F. *Chemistry – A European Journal* **2009**, *15*, 449.

(10) Xia, C.; Ning, W.; Lin, G. *Sensors and Actuators B: Chemical* **2009**, *137*, 710.

(11) Lines, M. E.; Jones, E. D. *Physical Review* **1965**, *139*, A1313.

(12) Gorbenko, O. Y.; Graboy, I. E.; Amelichev, V. A.; Bosak, A. A.; Kaul, A. R.; Güttler, B.; Svetchnikov, V. L.; Zandbergen, H. W. *Solid State Communications* **2002**, *124*, 15.

(13) Chang, Y. Q.; Yu, D. P.; Wang, Z.; Long, Y.; Zhang, H. Z.; Ye, R. C. *Journal of Crystal Growth* **2005**, *281*, 678.

(14) Cheng, F.; Shen, J.; Ji, W.; Tao, Z.; Chen, J. *ACS Applied Materials & Interfaces* **2009**, *1*, 460.

(15) Thota, S.; Prasad, B.; Kumar, J. *Materials Science and Engineering: B* **2010**, *167*, 153.

(16) Ghosh, M.; Biswas, K.; Sundaresan, A.; Rao, C. N. R. *Journal of Materials Chemistry* **2006**, *16*, 106.

(17) Schladt, T. D.; Graf, T.; Tremel, W. *Chemistry of Materials* **2009**, *21*, 3183.

(18) Song, Q.; Ding, Y.; Wang, Z. L.; Zhang, Z. J. *Chemistry of Materials* **2007**, *19*, 4633.

(19) Djerdj, I.; Arčon, D.; Jagličić, Z.; Niederberger, M. *The Journal of Physical Chemistry C* **2007**, *111*, 3614.

(20) Aslani, A.; Bazmandegan-Shamili, A.; Kaviani, K. *Physica B: Condensed Matter* **2010**, *405*, 3972.

(21) Song, Q.; Zhang, Z. J. *The Journal of Physical Chemistry B* **2006**, *110*, 11205.

(22) Cullity, B. D.; Graham, C. D. *Introduction to Magnetic Materials*; Wiley & Sons: Hoboken, 2009.

(23) Liu, C. R., Adam J.; Zhang, Z. J. *Pure Appl. Chem.* **2000**, *72*.

(24) Leslie-Pelecky, D. L.; Rieke, R. D. *Chemistry of Materials* **1996**, *8*, 1770.

(25) Winkler, E.; Zysler, R. D.; Fiorani, D. *Physical Review B* **2004**, *70*, 174406.

Chapter 5

Phase Selective Synthesis of ZrO_2 Nanoparticles

5.1 Abstract

Zirconium oxide is an important industrial material with applications ranging from micro-electronics to ceramic coatings, fuel cells to catalysts. Nanoscale applications of ZrO_2 depend on the size and phase of the oxide. Current methods used to synthesize nanoparticles of ZrO_2 either involve dangerous/expensive precursors or equipment or require extensive high temperature heat treatments that destroy monodispersity. This chapter reports the synthesis of monoclinic and cubic zirconia nanoparticles using modified hydrothermal and aminolytic methods, respectively. The synthesis techniques were simplified along with the use of simple starting materials in order to facilitate the scale-up process required for industry. The nanoparticles produced using these improved methods where highly pure, with sphere-like morphology. The size of the nanoparticles was found to be ~35 nm for the monoclinic nanoparticles, and ~15 nm for the cubic. The optimized annealing time and temperature was determined to be 20 hours at 600^{o}C for monoclinic formation and 2 hours at 400^{o}C for the cubic formation. Since ZrO_2 has applications in catalysis to enhance manipulation of the material, zirconia was coated on a magnetic core, $CoFe_2O_4$. This coating was accomplished using the aminolytic method. An amorphous shell was coated on the magnetic core and was converted to either fully cubic or a monoclinic/cubic mix using a tube furnace or a hydrothermal treatment. All

nanoparticles were characterized using XRD and TEM for phase purity and average size calculation.

5.2 Introduction

Research into synthesis and applications of nanoscale zirconium oxide (ZrO_2) have been investigated over the last 10 years due to its chemical and physical properties. These properties include chemical and corrosion inertness to about 2100^oC, high fracture toughness, low thermal conductivity, wide band gap (3-5 eV), and ionic and electrical conduction[1-3].

Zirconia has three phases: monoclinic (m-ZrO_2), tetragonal (t-ZrO_2), and cubic (c-ZrO_2). In bulk ZrO_2, the monoclinic phase is stable at room temperature and undergoes a phase transition to tetragonal at about 1150^oC. Upon further heating, the tetragonal phase will transform into the cubic phase at about 2370^oC[4]. When you consider nanocrystalline zirconia at room temperature, the phase can be either monoclinic or cubic, simply depending on the synthesis conditions used to produce them. The ability to control the phase growth of nanoparticles is of high importance today due to the unique properties and applications that can be obtained with certain phases. This is especially true with zirconia. Some applications based on the monoclinic phase zirconia are ceramic coatings[1], bioactive coatings[5], sensing materials for UV-dosimeters[6], and gate dielectrics in microelectronics[2]. Cubic phase zirconia nanoparticle-based applications include electrolyte material in solid oxide fuel cells[7,8], oxygen sensors[9], and catalysis/catalyst supports[10]. There have been reports of the use of cubic and monoclinic ZrO_2 as a catalyst in the decomposition of water into hydrogen and water[11].

Over the past decade, investigations into core/shell systems have shown that some reactive shells (i.e. catalysts) grown on a magnetic core affords fundamental control over a reaction[12]. With only an applied magnetic field, one could stop a reaction by removal of a catalyst. By growing a ZrO_2 shell over a core such as $CoFe_2O_4$ one would gain such control when using zirconia to decompose water. $CoFe_2O_4$ spinel nanoparticles are a good candidate for the core material due to enhanced magnetic properties and chemical stability[13,14].

There are several different methods for the synthesis of monoclinic and cubic zirconia, including hydrothermal, mechanochemical, spray pyrolysis, sol-gel, and emulsion coprecipitation; however, these synthesis techniques have drawbacks that would complicate their ability to be useful on the industrial scale. The hydrothermal method[15,16], which is able to produce both the monoclinic and cubic phase, suffers from slow reaction rates and often requires either a buffering agent or strong hydroxide. The mechanochemical method[17], which can produce c-ZrO_2, results in nanoparticles of poor crystallinity. This method also requires the use of a process control agent, which forms a by-product at the end of the reaction that needs to be removed before the ZrO_2 can be used. The chemical vapor deposition method[18] can produce highly crystalline cubic zirconia nanoparticles but requires complex, expensive equipment and starting materials. There is also a need for constant monitoring of the reaction, and high temperatures are required. The sol-gel method[19,20] is able to produce both monoclinic and cubic nanoparticles but suffers from slow reaction times, exact pH control, high calcination temperature, and a need for an inert atmosphere or protecting agent. The emulsion coprecipitation method[21] results in either the monoclinic or cubic ZrO_2 but contains

irregular sizes and shapes due to local concentration gradients. A surfactant, and sometimes a cosurfactant, is needed and the reaction produces a large amount of toxic waste compared to the amount of product made.

Herein, we report a simple synthesis for the production of highly phase-pure cubic and monoclinic zirconia nanoparticles as well as core/shell composites. The goal here is to simplify the synthesis technique, while reducing the amount of waste produced in order to be applicable to the industrial scale. This technique involves a two step process; the aminolytic method of Zr-acetate followed by either a calcination or hydrothermal step depending on the desired phase of ZrO_2. The aminolytic reaction is the controlled reaction of Zr-acetate and oleylamine, by means of an amide bond formation followed by a condensation reaction to form the metal oxide. It also allows for the separation of the nucleation and growth stages of nanoparticle formation, which results in controlled morphology and size distribution. The use of a simple non-coordinating, high-boiling solvent and a surfactant, as well as forgivable atmosphere requirements, makes this method more apt for the formation of c-ZrO_2 and m-ZrO_2 nanoparticles on an industrial level.

5.3 Experimental:

5.3.1 Cubic ZrO_2 synthesis

Cubic ZrO_2 nanoparticles were prepared via the aminolytic method. Zirconium(IV) acetate (~1.5 g) was dissolved in a mixture of 10 mL oleylamine and 40 mL dibenzyl ether, stirred for one hour at 140^{o}C while under an argon atmosphere. The temperature was raised to 240^o C at a ramping rate of 5^o C/min, and the reaction solution

was agitated for an additional hour. Upon cooling to room temperature, the nanoparticles were collected and washed with ethanol three times via centrifugation, and dried overnight in air. The resulting powder was annealed in air.

5.3.2 Monoclinic ZrO_2 synthesis

Monoclinic ZrO_2 nanoparticles were prepared via the aminolytic method. Zirconium(IV) acetate (~1.5 g) was dissolved in a mixture of 10 mL oleylamine and 40 mL dibenzyl ether, stirred for one hour at 140^o C while under an argon atmosphere. The temperature was raised to 240^o C at a ramping rate of 5˚C/min, and the reaction solution was agitated for an additional hour. Upon cooling to room temperature, the nanoparticles were collected and washed three times with ethanol via centrifugation, and dried overnight in air. The product was collected, washed, and transferred to a Teflon sleeve and sealed in a parabomb. The parabomb was heated (~180^o C) overnight. The nanoparticles were collected and dried. The sample was annealed in air.

5.3.3 $CoFe_2O_4/ZrO_2$ Core/Shell synthesis (c-ZrO_2 shell)

Cubic core/shell $CoFe_2O_4/ZrO_2$ nanoparticles were prepared by the aminolytic method[1]. Zirconium(IV) acetate (0.32 g) and $CoFe_2O_4$ cores (0.3 g prepared prior to coating via aminolytic method) were added to a mixture of 15 mL dibenzyl ether and 5 mL oleylamine and heated to 140^o C under an argon gas flow for one hour. The temperature was raised to 240^{o}C at a ramping rate of 5^{o}C/min and held there for another hour. The particles were collected using a strong magnet, washed several times with

absolute ethanol, and dried overnight in air. The amorphous ZrO_2 shell was converted to the cubic phase via annealing. The resulting product was gray/black.

5.3.4 $CoFe_2O_4/ZrO_2$ Core/Shell synthesis (mixed c/m-ZrO_2 shell)

Mixed cubic and monoclinic core/shell $CoFe_2O_4/ZrO_2$ nanoparticles were prepared by the aminolytic method[1]. Zirconium(IV) acetate (0.32 g) and $CoFe_2O_4$ cores (0.3 g) were added to a mixture of 15 mL dibenzyl ether and 5 mL oleylamine and heated to 140^{o}C under an argon gas flow for one hour. The temperature was raised to 240^{o}C at a ramping rate of 5^{o}C/min and held there for another hour. The particles were collected using a strong magnet, washed several times with absolute ethanol, and dried overnight in air. The amorphous ZrO_2 shell was converted to a mixed monoclinic and cubic shell via hydrothermal treatment. The sample was placed in a Teflon sleeve with a mixture of distilled water/1 M NaOH (1:1) and sealed in a parabomb. The parabomb was heated (180^o C) for 20 hours. The nanoparticles were collected and dried in air overnight. The sample was annealed in air.

5.3.5 Instrumentation

X-ray diffraction (XRD) data was collected with a Panalytical X'pert Pro X-Ray Diffractometer with a Cu Kα source over a 15º – 85º 2θ range. Particle size was determined from the average peak broadening of the five strongest Bragg peaks using the commercial program IGOR and the Debye-Scherrer equation assuming a shape factor of 0.9 (spherical).Transmission electron microscopy (TEM) studies were performed using a

JEOL 100CX2 instrument operating at 100 kV. Energy dispersive X-ray spectroscopy (EDS)measurements were performed using a EDS analyzer attached to the JEOL TEM,

5.4 Results/Discussion

5.4.1 Cubic ZrO_2

Figure 5.4.1 shows the product that was formed when the amorphous material collected from the aminolytic method was heated for extensive time at 600^{o} C. The ZrO_2 formed matches the standard pattern for cubic phase to a much higher degree than the tetragonal standard pattern. This can be seen in figure 5.4.1.

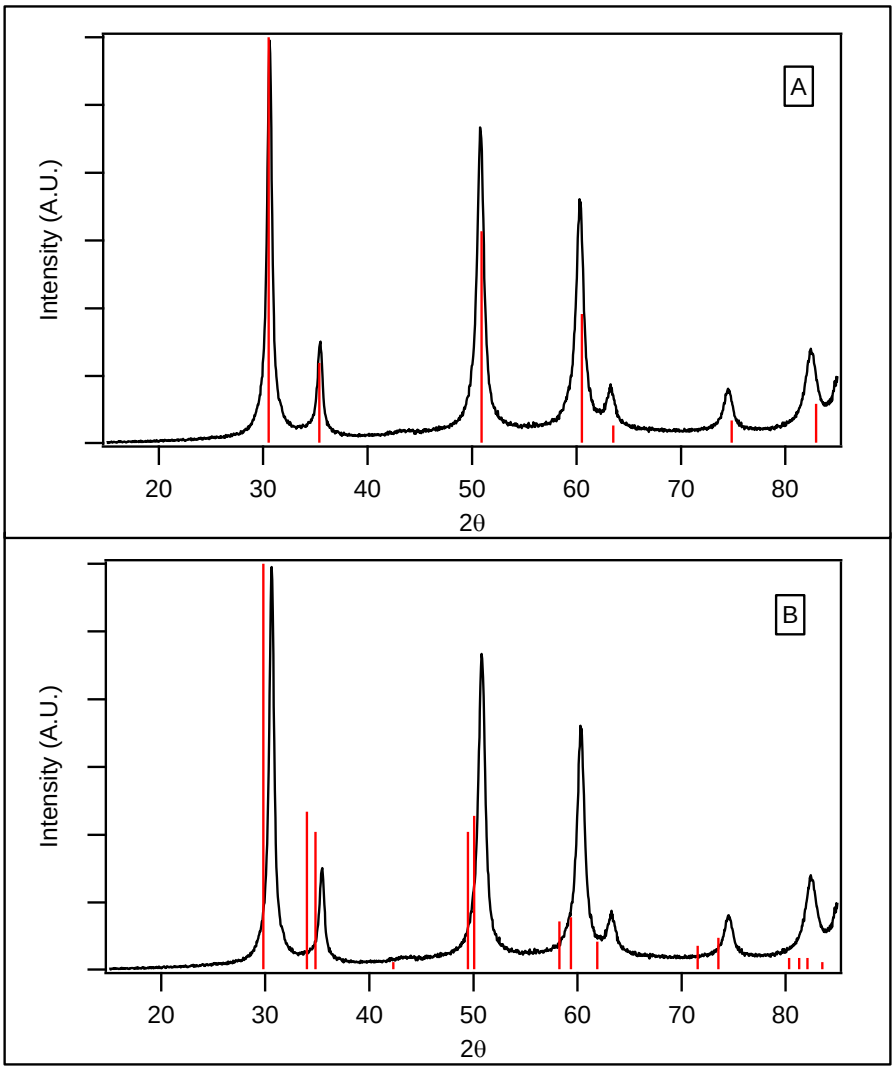

Figure 5.4.1: XRD patterns comparing standard peaks for cubic (A) and tetragonal (B).

As shown in Figure 5.4.1, the sample pattern contains no splitting of peaks at ~35°, ~50°, ~68°, and ~73° that accompanies the tetragonal structure. The splitting of these peaks is due the elongation of one of the crystallographic axes that is characteristic of the tetragonal crystal structure. Cubic ZrO_2 nanoparticle formation is preferred over tetragonal phase due to the lack of the elongated axis. As the grain size of ZrO_2 is decreased, the cubic (isotropic) morphology is preferred over a tetragonal (anisotropic)

one. This occurs in order to reduce the increase in surface energy that accompanies the reduction of grain size to the nanoscale[22].

Figure 5.4.2 shows the XRD pattern for the temperature dependence on the formation of cubic-phased nanoparticles from our method. The samples were heated from 300-500^{o}C for 20 hours.

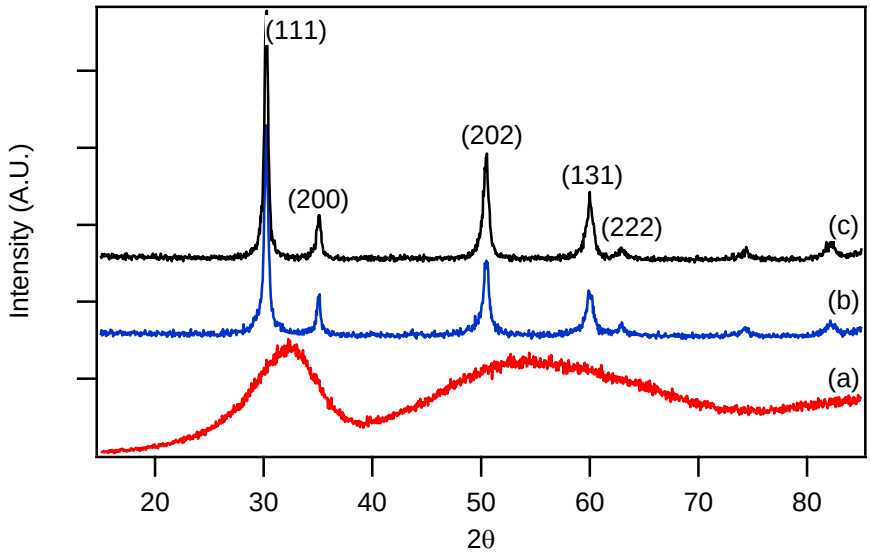

Figure 5.4.2: XRD patterns of the cubic samples after annealing in air for 20 hours at different temperatures (a) 300^{o}C, (b) 400^{o}C, (c) 500^{o}C.

At less then 300^{o}C, the sample is amorphous and remains so until the annealing temperature is raised to 400^{o}C where a conversion from an amorphous phase to the cubic phase occurs. The peaks are quite sharp and do not contain any impurities, showing the powder is a pure cubic-phased zirconia.

The XRD patterns of the time dependence on the formation of the cubic phase can be seen in Figure 5.4.3. The time ranges between 1-4 hours while the temperature is held at 400°C.

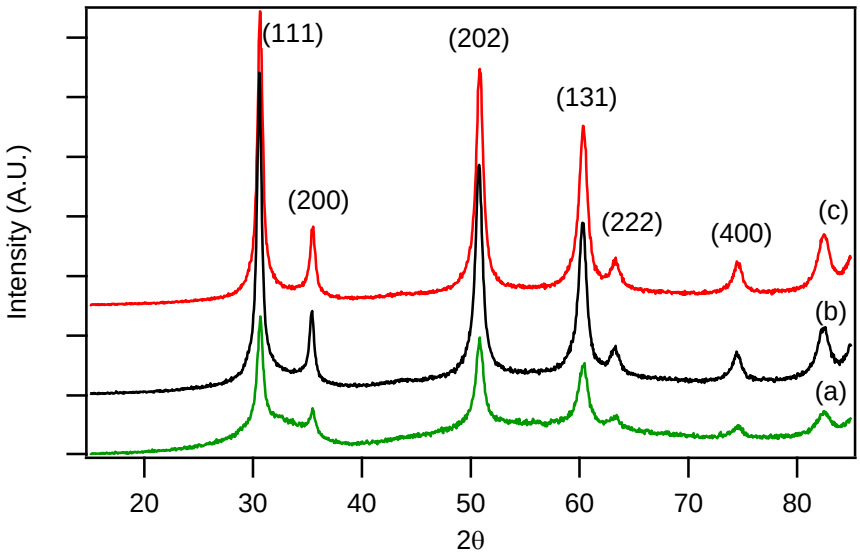

Figure 5.4.3: XRD patterns of cubic samples heated at 400°C for different lengths of time; (a) 1 hour, (b) 2 hours, (c) 4 hours.

Pattern (a) shows that, at one hour, the nanoparticles are a mix of amorphous and cubic nanoparticles. When the time is increased to 2 hours, there is a full conversion of the amorphous phase to the cubic phase. Again, the lack of extra peaks shows that the material is a pure cubic-phased zirconia. The peaks were assigned based on the cubic ($Fm\bar{3}m$) structure[23](PDF 04-014-0303). The average size of the cubic nanoparticles synthesized using the aminolytic method was ~15 nm using the Scherrer equation for the peak broadening of a reprehensive XRD pattern.

A TEM image of the nanoparticles synthesized by our method is shown in Figure 5.4.4. As it can be seen from the image, the nanoparticles are sphere-like with an average size (14.2) that corresponds well with the calculated size of 15 nm. The size distribution of the nanoparticles from the TEM images is about 12%.

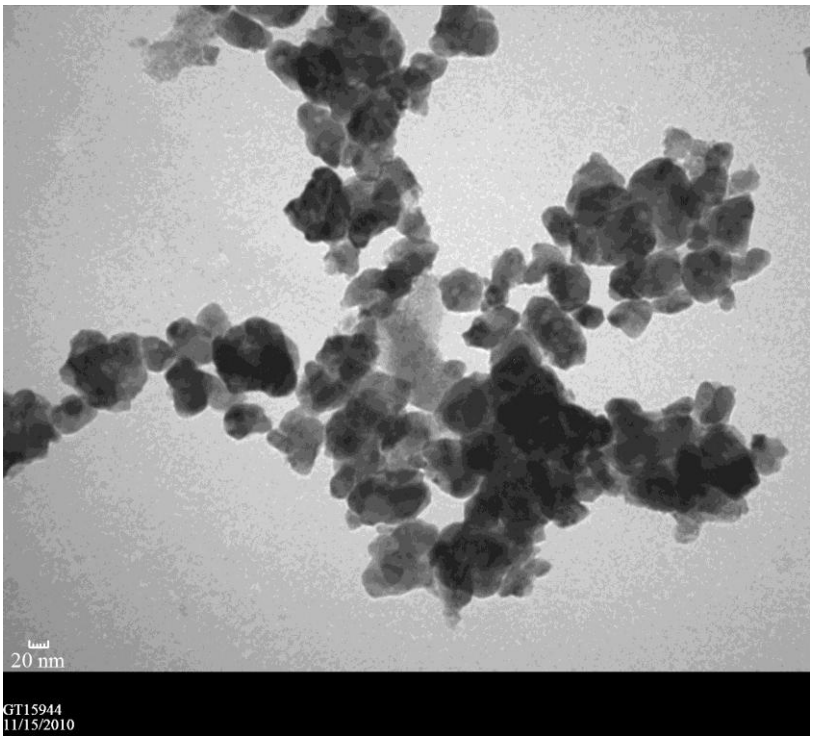

Figure 5.4.4: TEM image of the c-ZrO_2 nanoparticles synthesized at 400^oC for 2 hours.

5.4.2 Monoclinic ZrO_2

In the synthesis of the monoclinic ZrO_2 nanoparticles, it is important to note that the solid that is collected and dried after the hydrothermal treatment is a mixed phase system, meaning that the sample contains both cubic and monoclinic phases. Only when the powder is annealed in air is there a conversion of the mixed system to the monoclinic

phase. Figure 5.4.5 shows the XRD patterns of the time dependence of this conversion to the monoclinic phase.

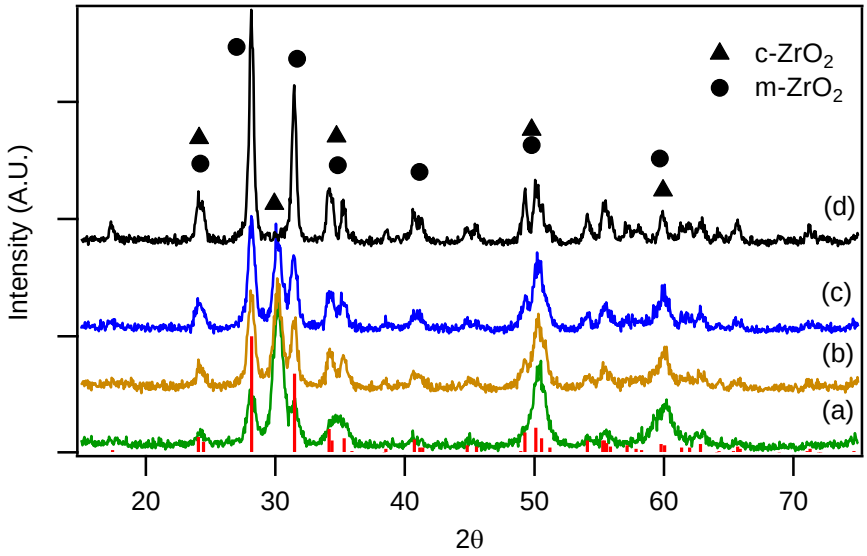

Figure 5.4.5: XRD patterns of the monoclinic samples after annealing in air for 20 hours at different temperatures (a) 400°C, (b) 500°C, (c) 550°C, (d) 600°C. Red lines indicate monoclinic ZrO_2 standard.

The samples were heated from 400-600°C for 20 hours per sample. At 400° the powder is still a mixed system, though as the temperature is increased, the cubic peak at ~30° decreases in intensity and completely vanishes at 600°. The monoclinic peaks located at ~28° and ~31° sharpen and increase in intensity, showing a conversion from this mixed system to that of a completely monoclinic-phased system. The peaks match that of the standard pattern (JCPDS 37-1484)[24]. The XRD pattern of the time dependence of the formation of the monoclinic phase from the mixed system can be seen in Figure 5.4.6.

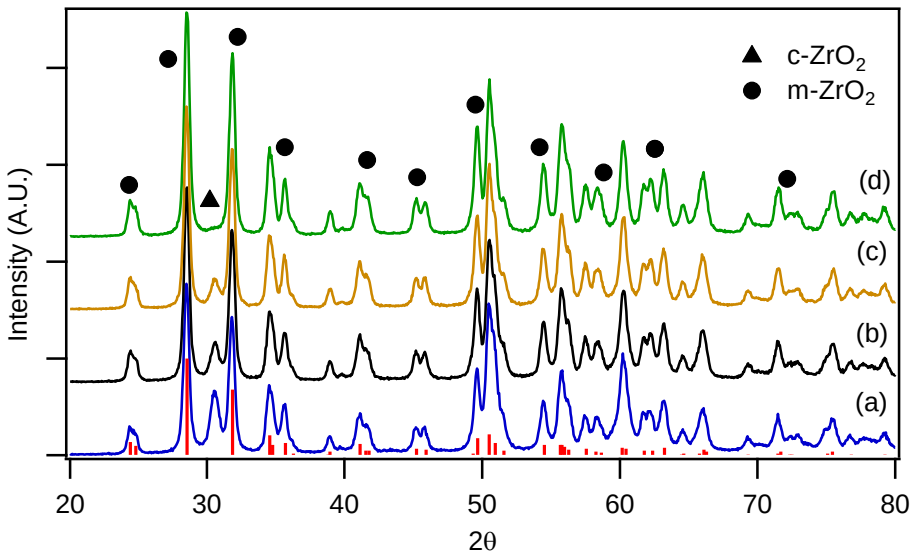

Figure 5.4.6: XRD patterns of monoclinic samples heated at 600°C for different lengths of time; (a) 8 hours, (b) 12 hours, (c) 15 hours, (d) 20 hours. Red lines indicate m-ZrO_2 standard.

The temperature was held at 600° while the time was varied from 8-20 hours. It can be seen that as the samples were annealed for longer periods of time, the cubic peak at ~30° again decreases and fully disappears at 20 hours, while the monoclinic peaks sharpen and grow in intensity. The XRD pattern for the sample annealed at 600°C for 20 hours shows no cubic peaks and no other impurities, meaning that the sample is purely monoclinic zirconia nanoparticles. Using the Scherrer equation for the peak broadening of XRD patterns, the average size of the monoclinic nanoparticles synthesized using our method was ~35 nm.

A TEM image of the nanoparticles synthesized by our method is shown in Figure 5.4.7. The average size from TEM images (34.3 nm) corresponds well with the calculated

size of 35 nm and has a size distribution of about 12%. The morphology of the nanoparticles, as seen in the TEM image, is sphere-like.

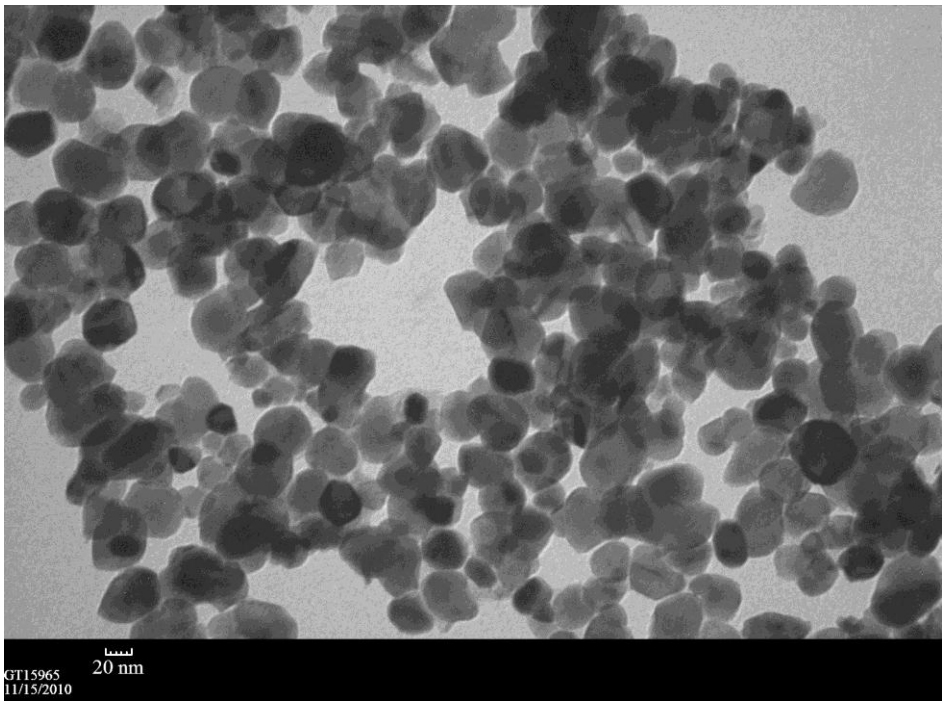

Figure 5.4.7: TEM image of the monoclinic ZrO_2 nanoparticles synthesized at 600^{o}C for 20 hours.

5.4.3 $CoFe_2O_4/ZrO_2$ Core/Shell

The core/shell system was synthesized using a $CoFe_2O_4$ nanoparticle core that was produced via the aminolytic method. The core contained oleylamine surfactant coating the surface. This is important as this coating allows for the zirconium acetate to react at the surface of the nanoparticle and not in the solution. The amount of zirconium acetate precursor added to the system was kept low intentionally to prevent seeds from forming in the solvent rather than at the nanoparticle surface. When the synthesis was completed, the product was collected utilizing a magnetic field. Since ZrO_2 is

nonmagnetic, any zirconia that formed without a core would be poured off and only the magnetically coated particles would remain. Figure 5.4.8 shows an XRD of core/shell sample where the shell has been converted to ZrO_2 with a cubic phase. The red pattern corresponds to the $CoFe_2O_4$ core before any coating occurs. The blue pattern is the magnetic core coated with amorphous ZrO_2 (a-ZrO_2).

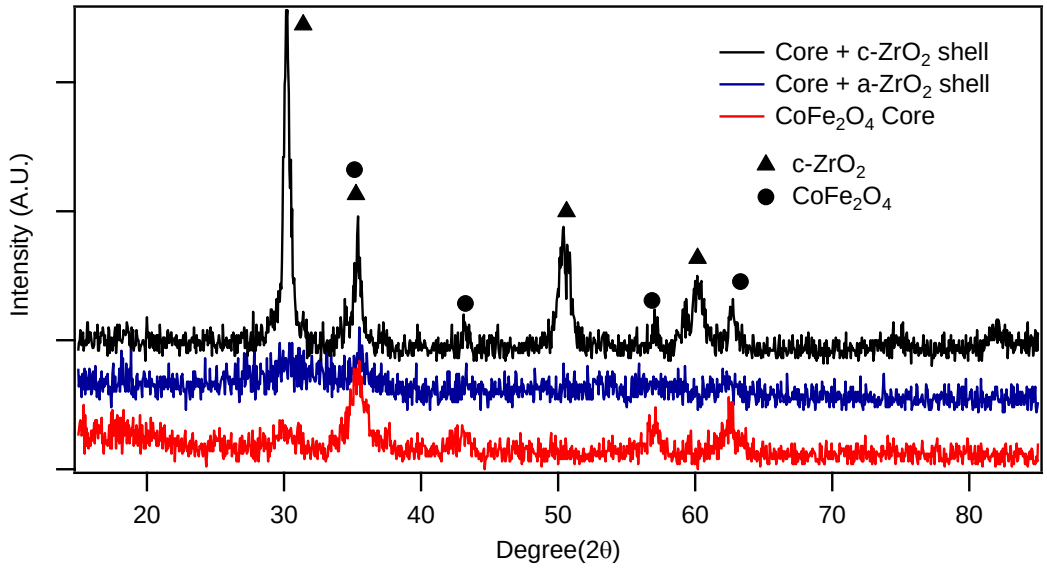

Figure 5.4.8: XRD pattern of the core/shell system. Red pattern indicates the $CoFe_2O_4$ core. The blue pattern is the amorphous ZrO_2 shell on the $CoFe_2O_4$ core. The black pattern is the cubic ZrO_2 shell on the $CoFe_2O_4$ core.

The broad peaks are indicative of amorphous zirconia[25]. When the sample is heated to 400^{o}C for 20 hours, there is a conversion from amorphous to cubic phase. This can be seen in the black pattern in Figure 5.4.8. The various peaks have been labeled with the corresponding phase contributor. The size of the core and the core/shell were calculated using the using the Scherrer equation and found to be 9.5 nm and 13 nm

respectively. In order to form a core/shell system with a phase mixed shell, an extra step is required. After the core is coated with amorphous zirconia using the aminolytic method, it is placed in a Teflon sleeve with a mixture of water and NaOH, and sealed in a parabomb and heated overnight. It has been shown that the use of 10 M NaOH will cause a phase conversion of cubic to monoclinic phase under similar conditions[26]. A similar approach was used to force a full conversion of the shell on the core/shell nanoparticles to a pure monoclinic phase, but it was unsuccessful. A 50% conversion was all that was achieved. Unsatisfied with the requirement of such a dangerous reactant, different concentrations of NaOH were tested. It was determined that a 0.5 M NaOH, was able to produce the same mixed phase shell as the 10 M. Figure 5.4.9 shows an XRD of core/shell sample, where the shell has been converted to a ZrO_2 mixed phase. The red pattern is the $CoFe_2O_4$ core, while the blue pattern is the core/shell system. The peaks and their corresponding phases are labeled as before. The size of the core and core/shell was calculated to be 8.1 nm and 12.2 nm respectively.

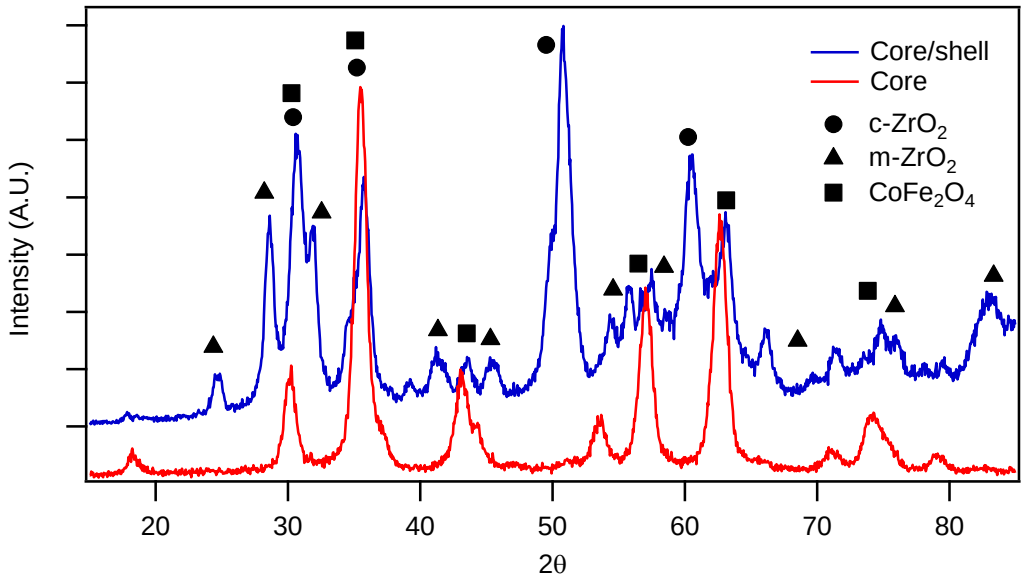

Figure 5.4.9: XRD pattern of the core/shell system. Red pattern indicates the $CoFe_2O_4$ core. The blue pattern is mixed cubic/monoclinic ZrO_2 shell on the $CoFe_2O_4$ core, with the corresponding peaks labeled.

Figure 5.4.10 shows a high resolution TEM image of the $CoFe_2O_4$/c-ZrO_2 core/shell system. As shown in the image, the particles are fused together, forming a large mass. This is believed to be due to agglomeration, resulting from the high temperatures and long heating time used to cause the amorphous ZrO_2 shell to crystallize into c-ZrO_2. To ensure complete transformation, the highest tested temperature of 600^oC and longest heating time of 20 hours was utilized. This would result in the agglomeration problem seen in the TEM image. A way to rectify the situation is to optimize the heating temperatures and time, as was performed in the sections above. A slower ramping rate to reach the final temperature or the addition of a stabilizing agent may also prevent agglomeration and help the particles to become separate core/shell nanoparticles.

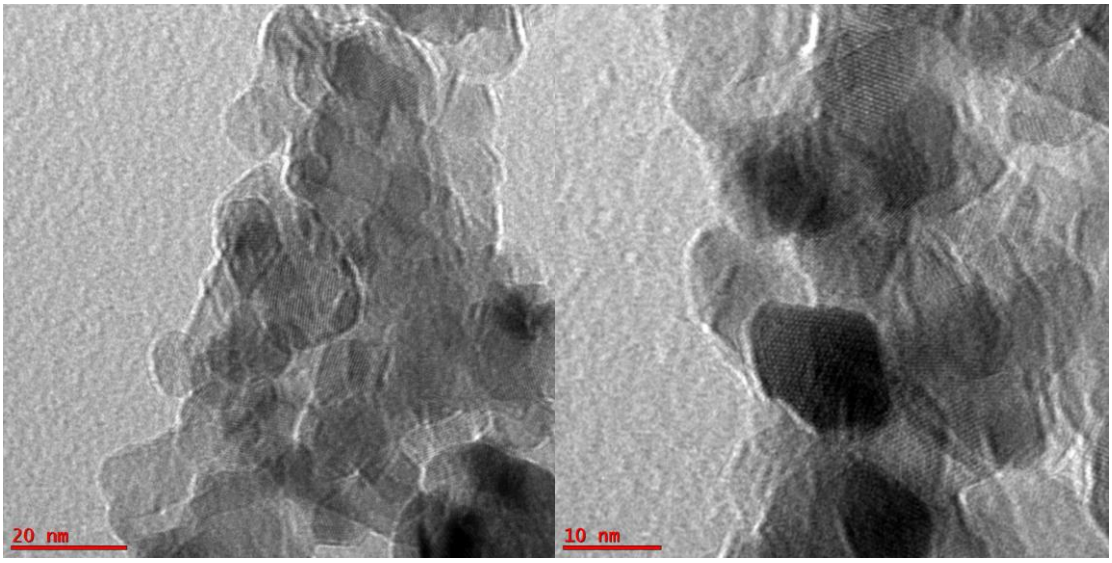

Figure 5.4.10 TEM images of the core/shell $CoFe_2O_4$/c-ZrO_2 nanoparticles.

Finally, Energy Dispersive X-ray Spectroscopy (EDX) was performed on the core/shell nanoparticles to ensure the presence of all parts and the absence of impurities. The spectrum is shown in Figure 5.4.11. and contains the necessary Co, Fe, and O for the core and the Zr and O for the shell. The copper and carbon found correspond to the carbon-coated copper grid that the measurement was performed on. The last element measured, Si, is due to scattered electrons striking the detector which can occur with a high energy electron beam.

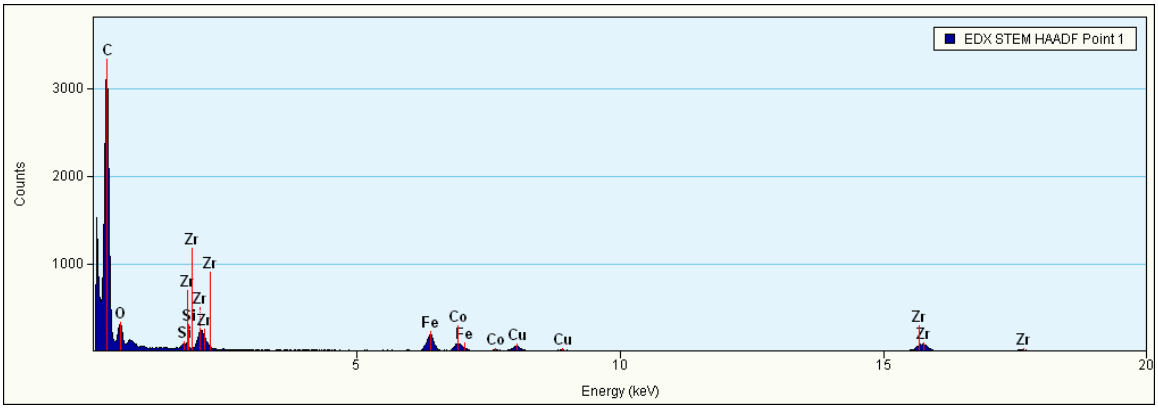

Figure 5.4.11 EDX spectrum of core/shell $CoFe_2O_4$/c-ZrO_2 nanoparticles.

5.5 Conclusion

Highly pure monoclinic and cubic zirconia nanoparticles were synthesized using a simple procedure, the aminolytic method, and starting materials of $ZrCl_4$. The heating conditions for the production of cubic nanoparticles where optimized and found to be the best for a temperature of 400^{o}C for 2 hours. The monoclinic nanoparticles required an optimized temperature and time of 600^{o}C for 20 hours for the best results. The nanoparticles produced were spherical with size distributions of ~15%. Synthesis of a core/shell system utilizing a magnetic $CoFe_2O_4$ core was also explored. Core/shells with a cubic phase shell, as well as with a cubic/monoclinic shell, were produced using a combination of the aminolytic method and hydrothermal/calcination steps. The XRD and TEM images show the ZrO_2 nanoparticles are single-phase and free of impurities, while the core/shell systems contain both the magnetic core and a ZrO_2 shell. The HRTEM did show an agglomeration problem due to the high temperatures and long heating times utilized to ensure full conversion of the shell to the desired crystal phase. More work needs to be performed to optimize the temperature and heating times to prevent the agglomeration problem while preserving the target crystal phase. The overall results of

this chapter do show that these nanoparticles can be produced on an industrial scale with little to no drawbacks, as well as the possibility of using the aminolytic method in the production of core/shell systems.

5.6 References

(1) Garvie, R. C.; Hannink, R. H.; Pascoe, R. T. *Nature* **1975**, *258*, 703.

(2) Wilk, G. D.; Wallace, R. M.; Anthony, J. M. *Journal of Applied Physics* **2001**, *89*, 5243.

(3) Zhang, Q.; Shen, J.; Wang, J.; Wu, G.; Chen, L. *International Journal of Inorganic Materials* **2000**, *2*, 319.

(4) Gao, P.; Meng, L. J.; dos Santos, M. P.; Teixeira, V.; Andritschky, M. *Thin Solid Films* **2000**, *377-378*, 32.

(5) Wang, G.; Meng, F.; Ding, C.; Chu, P. K.; Liu, X. *Acta Biomaterialia* **2010**, *6*, 990.

(6) Salas, P.; De la Rosa-Cruz, E.; Diaz-Torres, L. A.; Castaño, V. M.; Meléndrez, R.; Barboza-Flores, M. *Radiation Measurements* **2003**, *37*, 187.

(7) Minh, N. Q. *Journal of the American Ceramic Society* **1993**, *76*, 563.

(8) Susnik, D.; Holc, J.; Hrovat, M.; Zupancic, S. *Journal of Materials Science Letters* **1997**, *16*, 1118.

(9) Yu, S.; Wu, Q.; Tabib-Azar, M.; Liu, C.-C. *Sensors and Actuators B: Chemical* **2002**, *85*, 212.

(10) Li, Y.; He, D.; Cheng, Z.; Su, C.; Li, J.; Zhu, Q. *Journal of Molecular Catalysis A: Chemical* **2001**, *175*, 267.

(11) Reddy, V.; Hwang, D.; Lee, J. *Korean Journal of Chemical Engineering* **2003**, *20*, 1026.

(12) Phan, N. T. S.; Gill, C. S.; Nguyen, J. V.; Zhang, Z. J.; Jones, C. W. *Angewandte Chemie International Edition* **2006**, *45*, 2209.

(13) Liu, C.; Zhang, Z. J. *Chemistry of Materials* **2001**, *13*, 2092.

(14) Liu, C.; Zou, B.; Rondinone, A. J.; Zhang, Z. J. *The Journal of Physical Chemistry B* **2000**, *104*, 1141.

(15) Kanade, K. G.; Baeg, J. O.; Apte, S. K.; Prakash, T. L.; Kale, B. B. *Materials Research Bulletin* **2008**, *43*, 723.

(16) Tahir, M. N.; Gorgishvili, L.; Li, J.; Gorelik, T.; Kolb, U.; Nasdala, L.; Tremel, W. *Solid State Sciences* **2007**, *9*, 1105.

(17) McCormick, P. G.; Tsuzuki, T.; Robinson, J. S.; Ding, J. *Advanced Materials* **2001**, *13*, 1008.

(18) Srdić, V. V.; Winterer, M. *Journal of the European Ceramic Society* **2006**, *26*, 3145.

(19) Bokhimi, X.; Morales, A.; Novaro, O.; Portilla, M.; López, T.; Tzompantzi, F.; Gómez, R. *Journal of Solid State Chemistry* **1998**, *135*, 28.

(20) Roy, S.; Ghose, J. *Materials Research Bulletin* **2000**, *35*, 1195.

(21) Déchamps, M.; Djuriçić, B.; Pickering, S. *Journal of the American Ceramic Society* **1995**, *78*, 2873.

(22) Tsunekawa, S.; Ito, S.; Kawazoe, Y.; Wang, J. T. *Nano Letters* **2003**, *3*, 871.

(23) Joo, J.; Yu, T.; Kim, Y. W.; Park, H. M.; Wu, F.; Zhang, J. Z.; Hyeon, T. *Journal of the American Chemical Society* **2003**, *125*, 6553.

(24) Jiao, X.; Chen, D.; Xiao, L. *Journal of Crystal Growth* **2003**, *258*, 158.

(25) Wu, C.; Zhao, X.; Ren, Y.; Yue, Y.; Hua, W.; Cao, Y.; Tang, Y.; Gao, Z. *Journal of Molecular Catalysis A: Chemical* **2005**, *229*, 233.

(26) Noh, H.-J.; Seo, D.-S.; Kim, H.; Lee, J.-K. *Materials Letters* **2003**, *57*, 2425.

Chapter 6

Novel Synthesis of YIG and YIP Nanoparticles Produced via the Aminolytic Method and Magnetic Characterization

6.1 Abstract:

Yttrium iron garnet (YIG) and yttrium iron perovskite (YIP) nanoparticles have a multitude of applications, ranging from laser diodes to magnetic microwaves, biomedicine to photocatalysts. These nanoparticles have distinct advantages over their bulk counterparts due to unique magnetic properties and enhanced surface-to-volume ratio as a result of their nanoscaled size. Current synthesis techniques used to produce YIG and YIP nanoparticles require high calcination temperatures, which reduce monodispersity, as well as techniques that are sensitive to contamination. This chapter investigates the aminolytic reaction for the preparation of monodisperse YIG and YIP nanoparticles in pure single-phase. The particles were characterized via XRD and SQUID measurements. It was found that a heat treatment of 800^{o}C for 5 hours is required for full conversion from amorphous YIG to crystalline product (46 nm). The YIP nanoparticles (45nm), on the other hand, required 700^{o}C for 10 hours for full conversion. The SQUID data shows that YIG is a magnetically soft material with a coercivity value of 74.90 G but has high saturation and remnant magnetization values of 39 emu/g and 10.05 emu/g, respectively. YIP, on the other hand, is magnetically hard (18,757 G) with values of saturation and remnant magnetization of 1.53 emu/g and 0.796 emu/g, respectively.

6.2 Introduction:

Yttrium iron garnet ($Y_3Fe_5O_{12}$, YIG) nanoparticles belong to the ferromagnetic class of cubic garnets, with a general formula of $M_3Fe_5O_{12}$, and is one of the most studied and well-known of this class[1]. Another class of yttrium iron oxide is yttrium iron perovskite ($YFeO_3$, YIP), which belongs to a class of oxides whose general formula is A(III)B(III)O_3. Interest in these oxides is due to several key physical and chemical properties that they possess, including controllable saturation magnetization, narrow ferromagnetic resonance line widths, tunable Curie temperature, and low dielectric loss[2,3]. The above properties allow for the integration of YIG and YIP into a wide range of applications, such as magnetic microwave technologies[4,5], laser diodes[6], magneto-optical data storage[7,8], biomedicine[9,10], and antenna equipment[11].

YIP and YIG synthesized from standard solid state reactions using Y_2O_3 and iron oxide starting materials usually require long reaction times (above 24 hours) at high temperatures (>1200^{o}C) and can result in a substantial amount of impurities in the final product[12]. Over the past decade, synthetic methods that have more forgiving conditions were devised. Sol-gel methods[13,14], with a wide range of solvents and gels, allow a large drop in crystallization temperature. The trade off, however, is the need for pH control, slow reaction times, and an inert atmosphere or protecting agents. Coprecipitation[15] synthesis of YIG nanoparticles has been useful in the study of various Y/Fe ratios. This method utilizes the coprecipitation of metal hydroxides with some nonionic surfactant, followed by a calcination step, to form the final product. The resulting product is often either impure or has a particle size in the micrometer range. The calcination step in the coprecipitation step can be replaced with a hydrothermal treatment to promote the

formation of pure YIG[16,17]. The drawback to this is that there is a need for excess yttrium in the parabomb. The thermal decomposition method for the production of YIP[18,19] results in highly crystalline, monodisperse nanoparticles but is limited by the need for specialized starting materials and solvents and by impurities in the product. Spray drying techniques[20] for the production of YIG and YIP thin films has gained interest over the past few years due to fast reactions (minutes to a few hours) able to produce a large quantity of product; however, this method suffers from the need for specialized equipment, high calcination temperatures, and the correct forming additives to achieve the desired Y/Fe ratios. Sonochemical synthesis[21] allows for the formation of YIG and YIP nanoparticles that are phase-pure while requiring lower calcination temperatures. The trade off for this technique is the use of specialized equipment, long reaction times, and an inert atmosphere.

Herein we report a simple, fast synthesis for pure YIG and YIP nanoparticles that have low thermal and forgiving atmosphere requirements. This technique involves a controlled reaction of yttrium and iron chlorides with sodium acetate in oleylamine, by means of an amide bond formation followed by a condensation reaction to form the metal oxide. It also allows for the separation of the nucleation and growth stages of nanoparticle formation, which results in controlled morphology and size distribution. The use of a surfactant, as well as forgivable atmosphere requirements, allows this method to be more apt for the industrial formation of YIG and YIP nanoparticles. Structural and magnetic properties will also be discussed.

6.3 Experimental:

6.3.1 YIG

YIG precursor was prepared via an in-situ aminolytic method. $Y(NO_3)_3 \bullet 6H_2O$, $FeCl_3$ and sodium acetate, in a mole ratio of 3:5:26, were dissolved in 50 mL of oleylamine at 140^oC for one hour under an oxygen-rich environment. The temperature was raised to 240^oC at a ramping rate of 5^oC/min, and the solution was agitated for an additional hour. The resulting solid was collected via centrifugation and washed several times with ethanol followed by water to remove excess oleylamine and $NaCl/NaNO_3$ byproduct. The product was then allowed to dry overnight in air. The resulting solid was ground and annealed in air via a tube furnace at different temperatures, ranging from 500-800^oC.

6.3.2 YIP

YIP precursor was prepared via an in-situ aminolytic method. $Y(NO_3)_3 \bullet 6H_2O$, $FeCl_3$ and sodium acetate in a mole ratio of 1:1:6, were dissolved in 50 mL of oleylamine at 140^oC for one hour under an argon atmosphere. The temperature was raised to 240^oC at a ramping rate of 5^oC/min, and the solution was stirred for an additional hour. The resulting solid was collected via centrifugation, washed several times with ethanol to remove excess oleylamine, and then washed several times with distilled water to remove the $NaCl/NaNO_3$ byproduct. The solid was then allowed to dry overnight in air. The resulting powder was ground and annealed in air via a tube furnace at different temperatures, ranging from 500-800^oC.

6.3.3 Instrumentation:

X-ray diffraction (XRD) data was collected with a Panalytical X'pert Pro X-Ray Diffractometer with a Cu Kα source over a 15º – 85º 2θ range. Particle size was determined from the average peak broadening of the five strongest Bragg peaks using the commercial program IGOR and the Debye-Scherrer equation assuming a shape factor of 0.9 (spherical). Magnetic measurements were performed using a Quantum Design MPMS-5S SQUID magnetometer. Particles were immobilized in icosane ($C_{20}H_{42}$, Aldrich) for hysteresis measurements. Transmission electron microscopy (TEM) studies were performed using a JEOL 100CX2 instrument, operating at 100 kV. ICP-MS was collected using a PerkinElmer, NexION 300D. Particles were dissolved in nitric acid in hydrothermal conditions overnight and then diluted to concentrations on the order of ppm, in order to be measured by the ICP-MS.

6.4 Data/Results:

The synthesis of YIP and YIG is a two-step process. The first step is the preparation of a precursor via the aminolytic method. Yttrium nitrate is mixed with iron chloride in a 3:5 ratio for the garnet and a 1:1 ratio for the perovskite. The reaction then follows standard in-situ aminolytic conditions of heating to allow for the suspension of the metal ions in the oleylamine solvent, followed by raising the temperature above the reaction threshold to form the precursor. This precursor is then collected, washed, and dried overnight. The second step in the process of these garnets and perovskites is heating the precursors in a tube furnace to allow for the crystallization of the final product. The required time and temperature were then optimized.

6.4.1 YIP

The XRD pattern for the temperature dependence on the formation of YIP nanoparticles synthesized using the aminolytic and tube furnace heating method can be seen in Figure 6.4.1.

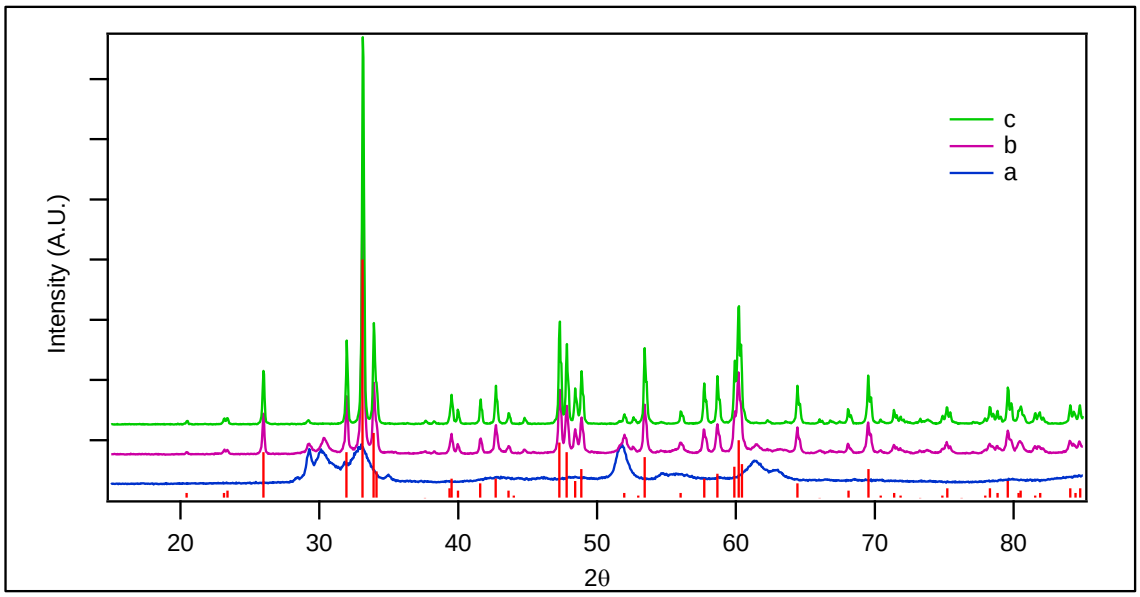

Figure 6.4.1: XRD pattern of YIP samples after annealing in air for 20 hours at different temperatures; (a) 500°C (b) 600°C (c) 700°C. Red lines indicate standard peaks.

The powder produced from the aminolytic method, amorphous YIP precursor, was then crystallized using a tube furnace. The samples were heated from 500-700°C for 20 hours. At 500°C, the sample was still somewhat amorphous and remained so until the annealing temperature was raised to 600°C, where a conversion from an amorphous phase to a crystalline phase occurred. There were, however, still some impurity peaks that remained at 700°C. The impurity was quite low, as seen by the intensity of the impurity

peaks, compared to the standard peaks of YIP. The impurity matches the pattern of Fe_2O_3. The pattern of the sample heated to 700^oC matches the standard powder diffraction pattern (ICDD File Number 39-1489). The standard peaks are also included in Figure 6.5.1. Table 6.4.1 shows the ICP-MS data for YIP samples heated at 500-700^oC. The iron-to-yttrium ratio is not fully 1:1 and shows a higher than expected iron concentration. This is due to the Fe_2O_3 impurity. The ratio of the iron to yttrium is only slightly higher than expected, indicating that the impurity is quite low.

Table 6.4.1: ICP-MS of YIP particles prepared at different temperatures.

	500^oC	600^oC	700^oC
Theoretical	1.00	1.00	1.00
Actual	1.29	1.25	1.39

Figure 6.4.2 shows the XRD patterns of the time dependence on the crystallization of the amorphous YIP. The time ranges between 2-20 hours while the temperature is held at a constant 700^oC.

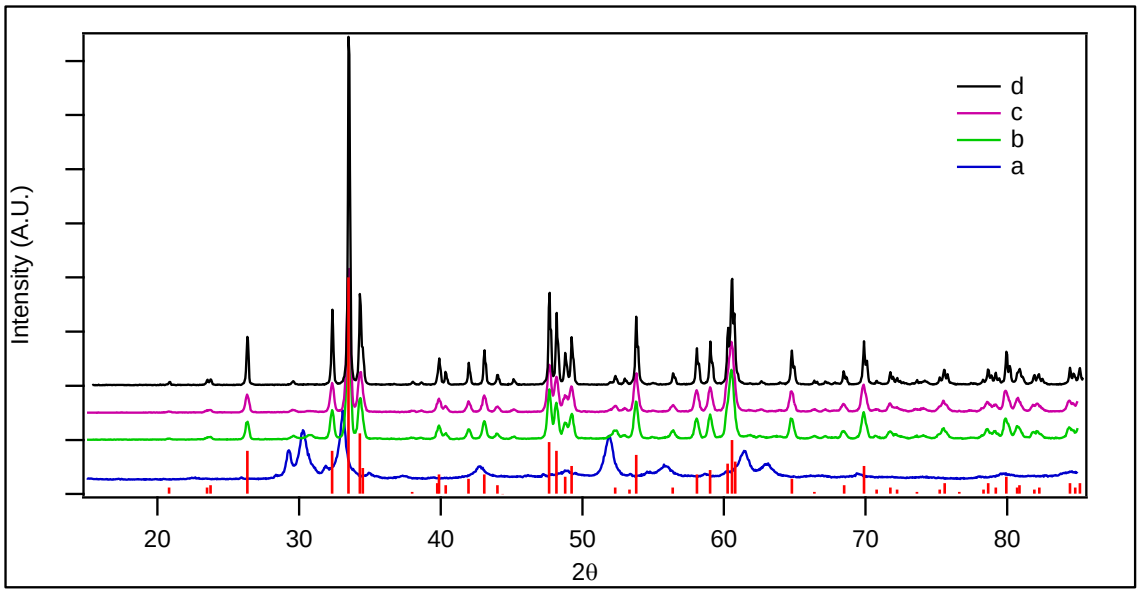

Figure 6.4.2: XRD patterns of YIP samples heated at 700^{o}C for different lengths of time; (a) 2 hours, (b) 5 hours (c) 10 hours (d) 20 hours.

There is a full conversion from amorphous to crystalline product that takes place between 5-10 hours. There is also an absence of impurity peaks in the samples heated for 10 hours and 20 hours. The standard peaks for YIP are also included in Figure 6.4.2. Using the commercial program, IGOR and the Scherrer equation for peak broadening in XRD patterns, the average size of the YIP nanoparticles synthesized using the aminolytic/tube furnace method was ~46 nm.

When the synthesis of YIP nanoparticles was optimized, magnetic studies were performed to obtain some magnetic data and was collected from a representative sample of the nanoparticles. The first measurement completed was a temperature-dependent measurement, which can be seen in Figure 6.4.3.

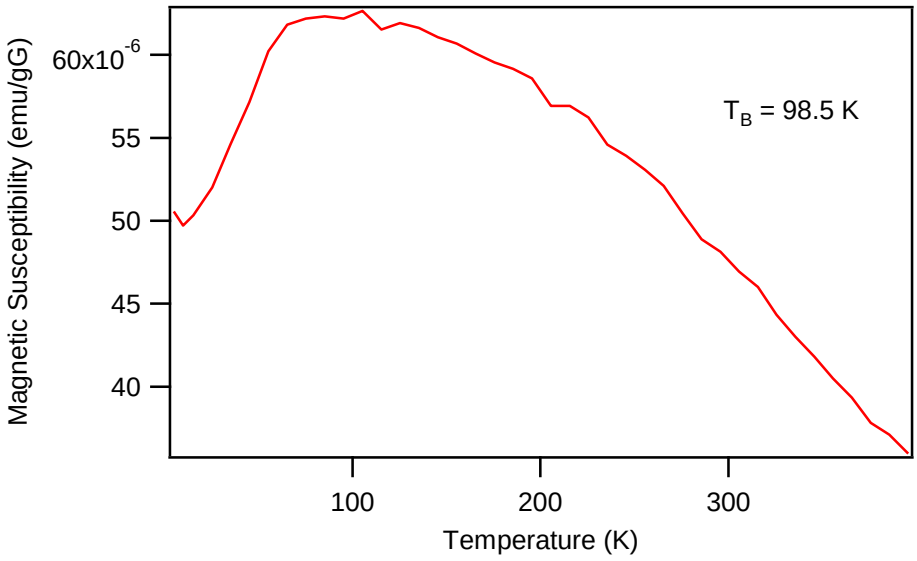

Figure 6.4.3: Temperature-dependent magnetization of YIP sample at 500 G.

As the temperature of the nanoparticles is increased, the susceptibility also increases. At 98.5 K, the system's blocking temperature, the magnetic ordering changes from ferrimagnetic to paramagnetic ordering, and there is a decrease in susceptibility as the temperature is increased. This result is expected with a ferromagnetic to paramagnetic transition that occurs at a sample's blocking temperature. The overall magnetic susceptibility is quite low when compared to a similarly sized $CoFe_2O_4$ or $MnFe_2O_4$.[18,22] This has to do with the magnetic structure of YIP. In the magnetic unit cell of YIP, the Fe^{3+} aligns in an antiferromagnetic fashion. The weak ferromagnetism measured arises from the slight canting (~8.9^o) of the iron ions[23]. Figure 6.4.4 shows a pictorial representation of the magnetic unit cell of YIP. The Fe^{3+} ions are aligned antiparallel to the c-axis, and the canting that occurs results in a net magnetic moment perpendicular to this axis. It has been reported that spontaneous magnetization (going past T_B) is quite low and is parallel to the elongated c-axis[23]. This results in a lower blocking temperature due

to the lower thermal energy requirements to switch from ferrimagnetic to superparamagnetic ordering.

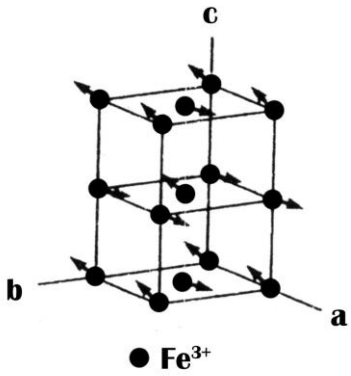

Figure 6.4.4.: Magnetic unit cell of YIP

The second type of magnetic study performed on the nanoparticles was a field-dependent study. A hysteresis loop for the same sample used in the temperature-dependent measurement was collected at 5 K and can be seen in Figure 6.4.5.

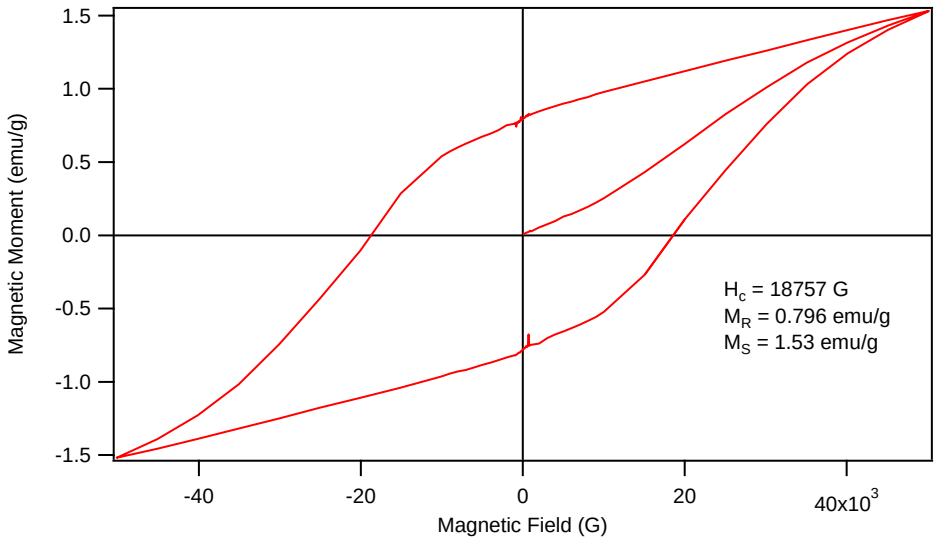

Figure 6.4.5: Hysteresis loop of YIP nanoparticles at 5 K.

The hysteresis measurement shows very interesting results. The first is the very wide coercivity, which indicates that the material is quite magnetically hard. This hardness is due mainly to the magnetocrystalline anisotropy that is inherent in orthoferrites, such as $YFeO_3$. Magnetocrystalline anisotropy energy is the energy required to rotate the magnetization vector from that of the easy axis to that of the hard axis. In YIP, the easy axis is the c-axis. Since YIP is elongated structurally along the c-axis, it will require more energy to rotate away from that axis to that of the hard axis, as compared to a cubic structure, where all axes are the same length. This increase in magnetocrystalline anisotropy results in a higher coercivity and thus a wider hysteresis loop. The next value calculated was that of the saturation magnetization. The sample measure showed a maximum value of only 1.53 emu/g. This value is quite low when compared to $CoFe_2O_4$ of similar size and even when compared to YIG of the same size. This is a result of the magnetic structure of YIP. Since Y^{3+} contributes no magnetic moment, the resulting magnetization measured is due to that of the Fe^{3+} ions. The perovskite structure of YIP results in the iron ions aligning antiparallel with respect to each other, resulting in an almost complete cancellation of their magnetic moments.[24] The fact that there is a magnetic moment measured indicates that the iron is not perfectly antiparallel. Wadas discusses in "Magnetism in Spinels Garnets and Perovskites" that the exchange interaction of the sites in orthoferrites are not as strong as in spinels, resulting in an incomplete antiparallel alignment of iron, resulting in a weak magnetism[24]. The final value measured was remnant magnetization. This value was calculated to be 0.796 emu/g. This value fits along with the scale of the saturation magnetization. To date, there

has not been any other group that has performed a detailed magnetic study on YIP nanoparticles, and therefore, there are no values with which to compare my measurements; however, we believe that our measurements are sensible, given the magnetic and crystal structure of perovskites and its chemical composition.

6.4.2 YIG

Figure 6.4.6 shows the XRD pattern for the temperature-dependence on the formation of YIG nanoparticles synthesized using the combined aminolytic method/tube furnace method.

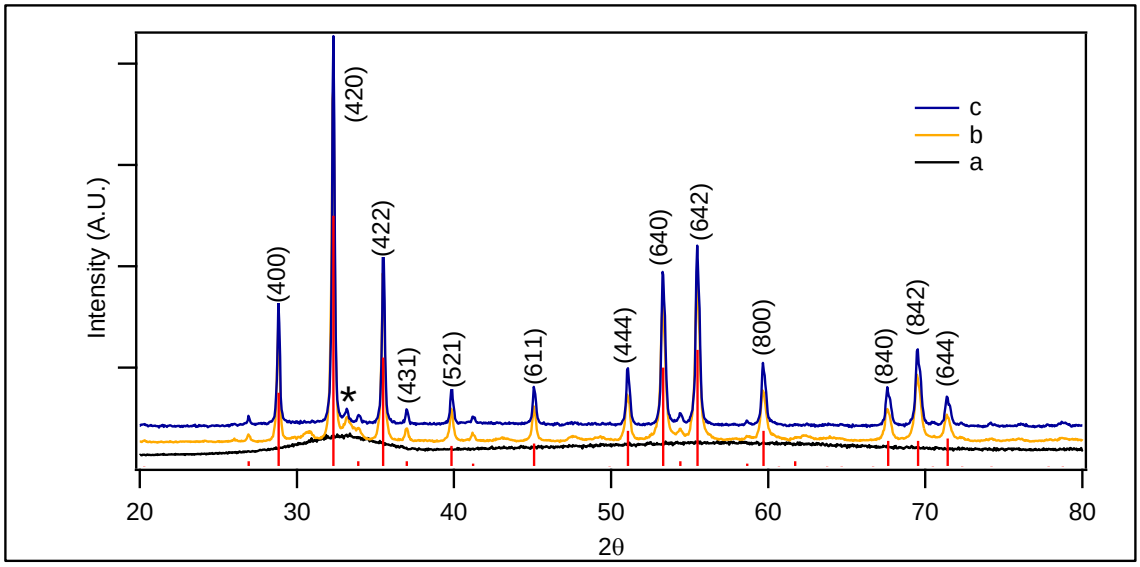

Figure 6.4.6: XRD pattern of YIG samples after annealing in air for 20 hours at different temperatures, (a) 600^{o}C (b) 700^{o}C (c) 800^{o}C. Red lines indicate standard peaks.

The aminolytic method produced the amorphous YIG precursor that was then converted to crystalline product via heating in a tube furnace. The samples were heated

from 500-800^{o}C for 20 hours. At 500^{o}C and below, the sample was amorphous and remained so until the annealing temperature was raised to 700^{o}C, where a conversion from an amorphous phase to a crystalline phase occurred. The Fe_2O_3 impurity peaks present in the sample prepared at 700^{o}C were still present in the sample heated to 800^{o}C, though to a far lesser amount, as seen by the extremely low relative intensity in the XRD pattern. These peaks are indicated with * in Figure 6.4.6. The pattern of the sample heated to 800^{o}C matches the standard powder diffraction pattern (ICDD File Number 43-507). The standard peaks are also included in Figure 6.4.6.

The XRD patterns of the time-dependence on the crystallization of the amorphous YIG can be seen in Figure 6.4.7. The time ranges between 1-20 hours while the temperature is held at 800^{o}C.

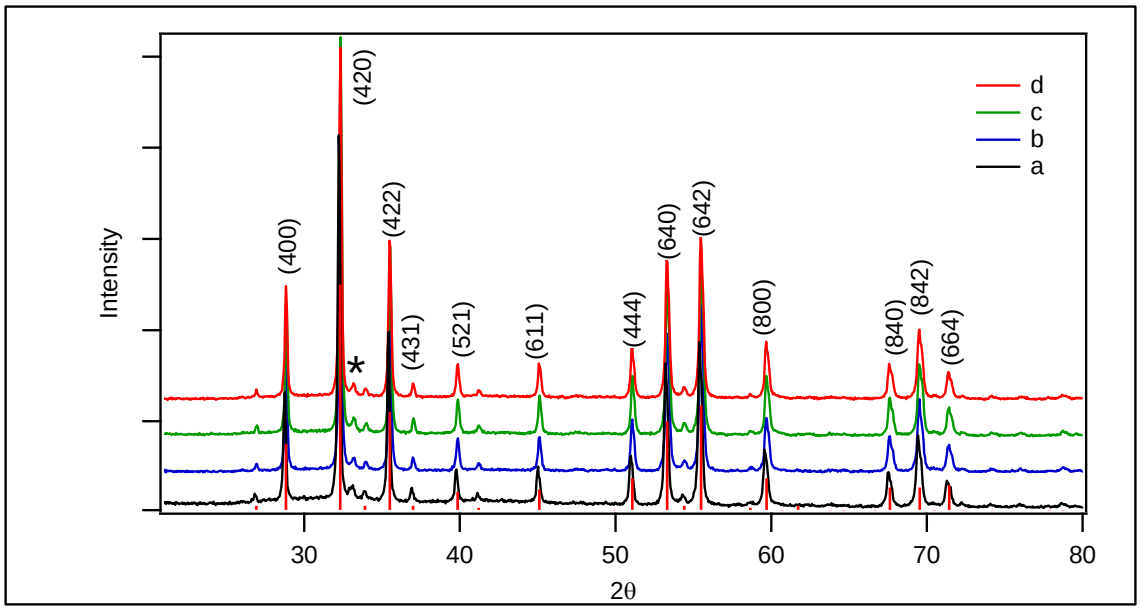

Figure 6.4.7: XRD patterns of YIG samples heated at 800^{o}C for different lengths of time; (a) 5 hours, (b) 10 hours (c) 15 hours (d) 20 hours. Red lines indicate standard peaks.

As seen in Figure 6.4.7, a heating time as low as 5 hours was needed for full conversion. There is still the presence of the Fe_2O_3 impurity peaks in all samples of the time-dependence study; again, they are a small amount, as seen by the low relative intensity of impurity peaks compared to the YIG peaks. Also included in the figure are the standard peaks for YIG. Based on peak broadening in XRD patterns, the Scherrer equation found the average size of the nanoparticles was ~45 nm.

Table 6.4.2 shows the ICP-MS data for YIG samples heated at 600-800^{o}C. The Fe:Y ratio is not fully 5:3, as expected, and indicated a higher than expected iron concentration. This is due to the Fe_2O_3 impurity. The ratio of the iron to yttrium is only slightly higher than expected, indicating that the impurity is quite low.

Table 6.4.2: ICP-MS of particles produced at temperatures between 600-800^{o}C.

	600^{o}C	700^{o}C	800^{o}C
Theoretical	1.66	1.66	1.66
Actual	2.23	2.50	2.13

Once the synthesis of YIG nanoparticles was optimized, magnetic data was collected from a representative sample of the nanoparticles. The first measurement was a temperature-dependent measurement. The resulting data can be seen in Figure 6.4.8.

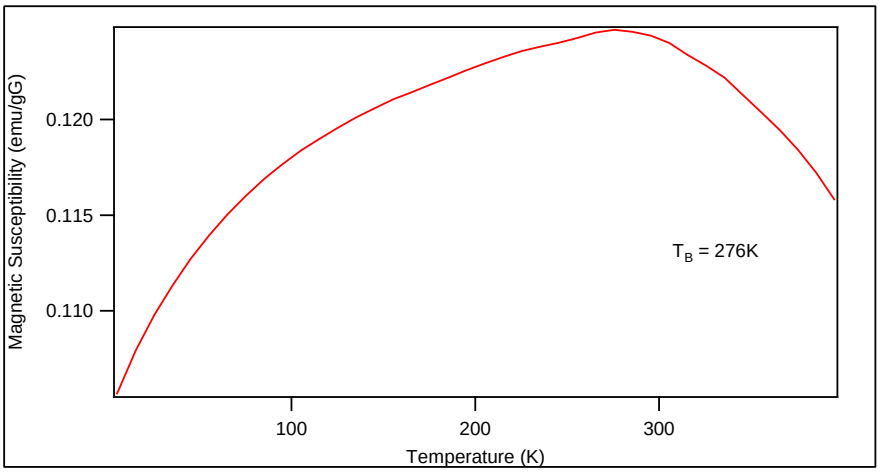

Figure 6.4.8: Temperature-dependent magnetization of YIG sample at 100 G.

As indicated, as the temperature of the nanoparticles is raised, the susceptibility also increases. At 276 K, the system's blocking temperature, the material changes from ferrimagnetic to paramagnetic ordering, and there is a decrease in susceptibility as the temperature is increased.

The second type of magnetic study performed on the nanoparticles was a field-dependent study. A hysteresis loop for the same sample used in the temperature-dependent measurement was collected at 5 K and can be seen in Figure 6.4.9.

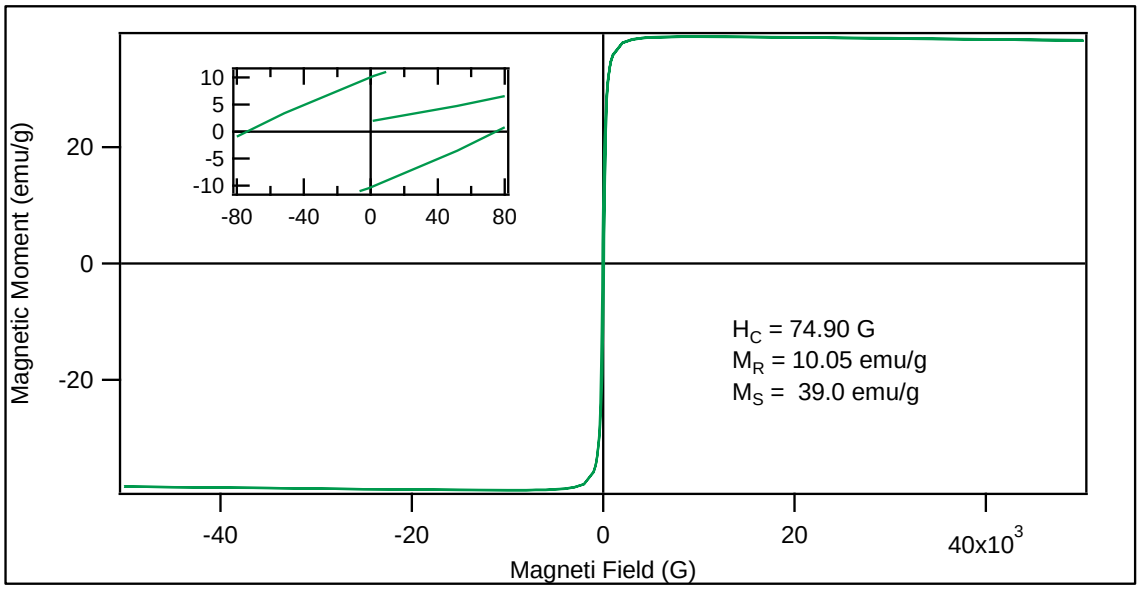

Figure 6.4.9: Hysteresis loop of YIG nanoparticles at 5 K.

The low coercivity of 74 G indicated that the material is quite magnetically soft. This makes sense as the magnetic properties of the YIG system are due to an imbalance of Fe^{3+} in A and B sites within its unit cell. Fe^{3+} in this structure consists of 5 unpaired electrons; however, it contains zero orbital angular momentum. Another reason why this material is soft is due to fact that material has low magnetocrystalline anisotropy. Garnets are cubic and with all crystallographic axes being of equal length, there is a lower amount of energy required to rotate from the easy axis to the hard axis. This results in a lower coercivity and a thinner loop, as seen above. The measured remnant magnetization value is 10 emu/g while the saturation magnetization was found to be 39 emu/g. These measured values are consistent with those found in similar YIG nanoparticles synthesized by Rajendran et al[25].

6.5 Conclusion:

Nanoparticles of YIG and YIP were successfully synthesized via the in-situ aminolytic method, coupled with tube furnace heating. The heating requirements for the synthesis of these garnets and perovskites are lower than previously reported and require uncomplicated starting materials. More work, however, needs to be performed to further purify the YIG and YIP systems of impurities before a more in-depth magnetic study can be performed. One possible way to purify this system is in the use of magnetic separation using a peristaltic pump, the idea being the YIG and YIP have a higher magnetic moment compared to that of the Fe_2O_3 and, thus, will be filtered out upon the application of a magnet. Another direction this project can take is in doping other cations into the system to observe the changes in magnetism to tailor the nanoparticles for specific applications.

6.6 References:

(1) Martha, P.-H. *Journal of Magnetism and Magnetic Materials* **2000**, *215–216*, 171.

(2) Yang, Q.; Zhang, H.; Liu, Y.; Wen, Q.; Jia, L. *Materials Letters* **2008**, *62*, 2647.

(3) Oka, K. *J. Appl. Phys* **1984**, *56*.

(4) Aichele, T.; Lorenz, A.; Hergt, R.; Görnert, P. *Crystal Research and Technology* **2003**, *38*, 575.

(5) Tatarenko, A. S.; Srinivasan, G.; Bichurin, M. I. *Applied Physics Letters* **2006**, *88*, 183507.

(6) Boudiar, T.; Capraro, S.; Rouiller, T.; Blanc-Mignon, M. F.; Payet-Gervy, B.; Le Berre, M.; Rousseau, J. J. *Physica Status Solidi (c)* **2004**, *1*, 3347.

(7) Rastogi, A. C.; Moorthy, V. N.; Dhara, S. *Applied Physics Letters* **2001**, *78*, 1709.

(8) Anderson, R. M.; Vestal, C. R.; Samia, A. C. S.; Zhang, Z. J. *Applied Physics Letters* **2004**, *84*, 3115.

(9) Grasset, F.; Mornet, S.; Demourgues, A.; Portier, J.; Bonnet, J.; Vekris, A.; Duguet, E. *Journal of Magnetism and Magnetic Materials* **2001**, *234*, 409.

(10) Scarberry, K. E.; Dickerson, E. B.; Zhang, Z. J.; Benigno, B. B.; McDonald, J. F. *Nanomedicine: Nanotechnology, Biology and Medicine* **2010**, *6*, 399.

(11) Ustinov, A. B.; Srinivasan, G.; Fetisov, Y. K. *Journal of Applied Physics* **2008**, *103*, 063901.

(12) Mergen, A.; Qureshi, A. *Journal of Alloys and Compounds* **2009**, *478*, 741.

(13) Gatelyte, A. *Advanced Materials Research* **2011**, *222*.

(14) Shaiboub, R.; Ibrahim, N. B. y.; Abdullah, M.; Abdulhade, F. *Journal of Nanotechnology* **2011**, *2011*.

(15) Zheng, L. *Advanced Materials Research* **2011**, *311-313*, 1294.

(16) Cho, Y. S.; Burdick, V. L.; Amarakoon, V. R. W. *Journal of the American Ceramic Society* **1997**, *80*, 1605.

(17) Sadhana, K.; Shinde, R. S.; Murthy, S. R. *International Journal of Modern Physics B: Condensed Matter Physics; Statistical Physics; Applied Physics* **2009**, *23*, 3637.

(18) Song, Q.; Ding, Y.; Wang, Z. L.; Zhang, Z. J. *Chemistry of Materials* **2007**, *19*, 4633.

(19) Xiwen, Z.; Raorong, H. *Journal of Crystal Growth* **2008**, *310*, 3804.

(20) Nanni, F.; Lamastra, F. R.; Bianco, A.; Leonardi, F.; Gusmano, G. *International Journal of Applied Ceramic Technology* **2008**, *5*, 624.

(21) Pinkas, J.; Reichlova, V.; Serafimidisova, A.; Moravec, Z.; Zboril, R.; Jancik, D.; Bezdicka, P. *The Journal of Physical Chemistry C* **2010**, *114*, 13557.

(22) Liu, C.; Zou, B.; Rondinone, A. J.; Zhang, Z. J. *The Journal of Physical Chemistry B* **2000**, *104*, 1141.

(23) McCurrie, R. A. *Ferromagnetic Materials Structure and Properties*; Academic Press: New York, 1999.

(24) Wadas, R. S. *Magnetism in Spinels Garnets and Perovskites*; Dom Slowa Polskiego: Poland, 1974.

(25) Rajendran, M.; Deka, S.; Joy, P. A.; Bhattcharya, A. K. *Journal of Magnetism and Magnetic Materials* **2006**, *301*.

VITA

Daniel E. Sabo

Daniel Sabo was born in Long Branch, New Jersey, to Samuel and Lisa Sabo. He attended Pennsylvania State University and Rowan University and graduated magna cum laude with a B.S. in Chemistry in 2006. Daniel conducted his graduate work at Georgia Institute of Technology in Atlanta, Georgia, under the direction of Dr. Z. John Zhang, working on nanoparticle synthesis characterization and application. In 2012, he graduated with a Ph.D. in Inorganic Chemistry.